UNIVERSITÀ
DEGLI STUDI
DI TRIESTE

UNIVERSITÀ DEGLI STUDI DI TRIESTE

XXXVI CICLO DEL DOTTORATO DI RICERCA IN
SCIENZE DELLA TERRA, FLUIDODINAMICA E MATEMATICA. INTERAZIONI E METODICHE

Kinematic Inversion of Earthquake Cycle Deformation Using SAR Interferometry

Settore scientifico-disciplinare:
GEO/10 GEOFISICA DELLA TERRA SOLIDA

DOTTORANDO
MUHAMMAD TAHIR JAVED

COORDINATORE
PROF. STEFANO MASET

SUPERVISORE DI TESI
PROF. CARLA BRAITENBERG

CO-SUPERVISORE DI TESI
PROF. SYLVAIN BARBOT

Contents

Extended abstract vii

Acknowledgements xiii

Dedication xv

1 Introduction 1

1.1 Introduction . . . 1
1.2 Research Objectives . . . 3

2 Crustal Deformation and Principle of InSAR 5

2.1 Introduction . . . 5
2.2 Synthetic Aperture Radar Satellites . . . 6
2.2.1 European Space Agency Sentinel-1 Satellites . . . 6
2.2.2 Advanced Land Observing Satellites (ALOS) . . . 9
2.3 SAR Complex Image and Resolution . . . 9
2.3.1 Ground Resolution Cell . . . 9
2.3.2 Azimuth and Range Resolution . . . 11
2.4 SAR Interferometry and Processing Techniques . . . 13
2.4.1 Interferometric Phase . . . 13
2.4.1.1 Topographic Phase . . . 15
2.4.1.2 Atmospheric Phase Errors . . . 15
2.4.1.3 Unwrap Phase Errors . . . 17
2.4.1.4 Other sources of Noise . . . 18
2.5 Earthquake Deformation Cycle . . . 19
2.5.1 Coseismic Deformation . . . 19
2.5.2 Postseismic Deformation . . . 20
2.5.3 Interseismic Deformation . . . 21

3 Coseismic Folding at the front of the Sulaiman Fold and Thrust belt 23

3.1 Introduction . . . 23
3.2 Methods of InSAR Processing and Modeling . . . 26
3.2.1 InSAR Analysis . . . 26
3.2.2 Error Estimation . . . 28

3.2.3 InSAR Modeling . . . 29
3.3 Kinematic Inversions and Folding . . . 34
3.4 Kinematic Inversion of Coseismic Slip and Folding . . . 35
3.5 Discussion . . . 42
3.6 Conclusions . . . 46
4 Insights into the Western Sulaiman Fold and Thrust belt 47
4.1 Introduction . . . 48
4.2 Methodology . . . 51
4.2.1 InSAR Data Processing . . . 51
4.2.2 Error Estimation . . . 54
4.3 Kinematic Inversions . . . 55
4.3.1 InSAR Modeling . . . 55
4.4 Results and Discussion . . . 56
4.4.1 Results . . . 56
4.4.1.1 The NW-SE Rupture Model . . . 57
4.4.1.2 The NE-SW Rupture Model . . . 57
4.4.1.3 Finite Fault Slip Distribution . . . 59
4.4.2 Discussion . . . 62
4.5 Conclusions . . . 72
5 Insights into the 2023 Earthquake Sequence on the East Anatolian Fault System 73
5.1 Introduction . . . 74
5.2 Recent Seismicity on the EAF System . . . 77
5.2.1 The 2023 Kahramanmaraş, and Elbistan Earthquake Sequences . . . 77
5.2.2 The 2023 Antakya Aftershock . . . 79
5.2.3 The 2020 Elazığ Earthquake . . . 79
5.3 Methodology used for studying the Antakya Aftershock . . . 80
5.3.1 Analysis of Antakya Aftershock . . . 80
5.3.1.1 InSAR Data Processing . . . 80
5.3.1.2 Geodetic Bayesian Inversion of Antakya Aftershock . . . 81
5.3.1.3 Slip Distribution of the 2023 Earthquake Sequences . . . 86
5.4 Fault Creep at Pütürge Segment Prior to the 2023 Earthquake Sequences . 90
5.4.1 Coseismic Rupture of the 2020 Mw 6.8 Elazığ Earthquake . . . 90
5.4.2 Slip Distribution of the Mw 6.8 Elazığ Earthquake . . . 92
5.4.3 Data and Methodology for SBAS Time Series . . . 93
5.4.4 Analysis of Fault Creep at Pütürge Segment . . . 96
5.5 Discussion . . . 103
5.6 Conclusions . . . 105

6 Conclusions **107**

Bibliography **111**

List of Figures **131**

List of Tables **143**

Extended abstract

The doctoral dissertation titled "Kinematic Inversion of Earthquake Cycle Deformation Using SAR Interferometry" provides insights into the crustal deformation mechanisms triggered by intraplate and interplate earthquakes along the western boundary of the Indian-Eurasian plates, along the Sulaiman Fold-Thrust (SFT) belt utilizing space geodesy techniques. The processing is also applied to investigate the fault movement along the East Anatolian Fault (EAF), at the boundary of the Arabian-Anatolian plates.

Geodetic observations provide valuable insights into the kinematics of continental tectonic plates at both global and regional scales. The revolution of space geodesy in recent decades enables us to monitor the deformation style and characterize its temporal and spatial variations (Barbot and Weiss, 2021; Barbot et al., 2023; Gordon and S. Stein, 1992; S. Stein, 1993). Complex trans-compressional fault systems are predominantly characterized by fault bends and step-over structures along major faults (Barka and Kadinsky, 1988; Cakir et al., 2023; Konca et al., 2021; Tatar et al., 2012; Yule and Sieh, 2003). Several notable examples of such active complex fault systems include the Gargano fault system in the central Adriatic region in Italy, the East Anatolian fault (EAF) and North Anatolian fault (NAF) systems in Turkey, the Marlborough fault system in New Zealand, the San Andreas fault system in the United States, and the Sulaiman Fold thrust belt in Pakistan, all of which are known for high seismicity (Barbot et al., 2013; Barbot et al., 2023; Barka, 1996; Billi et al., 2007; Cakir et al., 2023; Chiarabba et al., 2005; Javed et al., 2022; Konca et al., 2021; Tatar et al., 2012). Complicated fault geometries in trans-compressional regions affect the nucleation and propagation of ruptures, ultimately controlling the size of earthquakes (Javed et al., 2022; Lapusta and Rice, 2003; Sathiakumar and Barbot, 2021; Sathiakumar et al., 2020; Wesnousky, 2006).

Recently, on February 6, 2023, the Mw 7.8 Kahramanmaraş earthquake ruptured the 310 km long EAF system. Just nine hours later after the first devastating earthquake, a Mw 7.6 earthquake ruptured a 150 km long, E-W trending, left-lateral splay of the EAF system (Barbot et al., 2023; Lomax, 2023; Zilio and Ampuero, 2023). These two earthquakes collectively ruptured 13 fault segments with varying strikes along the EAF system, resulting in a maximum slip of 12

m (Barbot et al., 2023; Melgar et al., 2023). Similarly, the 2016 Mw 7.8 Kaikoura earthquake produced a rupture along the Marlborough branching fault system, involving 21 faults and generating approximately 10 m of coseismic surface displacement (W. Xu et al., 2018). Synthetic Aperture Radar (InSAR) Interferometry provides valuable tools for accurately investigating the sources of complex tectonic processes and the structure of the deforming elastic and viscoelastic crust, from global to regional scales (Barbot et al., 2023; Barkat et al., 2022; Cakir et al., 2023; Feng et al., 2015; Javed et al., 2022; R. Jolivet et al., 2012; Nissen et al., 2016; Rollins et al., 2018).

First, we use SAR interferometry observations to understand the slow and complex deformation processes at the frontal zone of the SFT belt, central Pakistan (discussed in Chapter 3) and then we investigate crustal deformation at the western zone of the SFT belt (discussed in Chapter 4). The relative motion between the Indian and Eurasian tectonic plates is accommodated across wide fault zones along the SFT belt. The SFT belt formed during the India-Eurasia collision in the late Cenozoic. However, the mechanics of shortening of the brittle crust at time scales of seismic cycles is still poorly understood (Banks and Warburton, 1986; Bernard et al., 2000; Saif-Ur-Rehman et al., 2019; 2020). In order to better assess the seismic potential, a key question that needs to be addressed is why moderate-size seismicity is observed along the eastern zone, as opposed to the higher magnitude seismicity in the western zone of the SFT belt. Do geometric complexities or fault dimensions exist in the frontal SFT belt zone that control the coseismic slip propagation and the earthquake magnitude as suggested in several publications (Namson and T. L. Davis, 1988; Sathiakumar and Barbot, 2021; Sathiakumar et al., 2020; Weng and Yang, 2017)?

We use the spaceborne radar interferometry to analyze the deformation associated with the 2015 moment magnitude (Mw) 5.7 Dajal blind earthquake at the eastern boundary of the SFT. We use kinematic inversions to determine the distribution of slip on the frontal ramp and of flexural slip along active axial surfaces for the forward- and backward-verging two end-member models: a double fault-bend fold system and a fault-propagation fold. In both models, a décollement branches into a shallow ramp at approximately 7.5 km depth with coseismic folding in the hanging wall. The Dajal earthquake ruptured the base of the Boundary Thrust buried under the sediment from the Indus River floodplain, representing fault-bend or fault-propagation folding some 30 km off its nearest surface exposure.

The rupture of the 2015 Mw 5.7 Dajal did not reach the surface, buried under the younger sediments of the Indus River floodplain. The rupture and associated folding in the hanging wall document the eastward growth of the SFT.

The earthquake represents the seismic rupture of a frontal blind ramp of the SFT, presumably as the seismic expression of a Fault-Bend Fold (FBF) or Fault-Propagation Fold (FPF). The earthquake illuminates the possible extension of the Boundary Thrust 30 km south of the Zindapir anticlinorium where it breaks the surface, corresponding to the propagation of the SFT some 30 km east into the Miocene and younger sediments of the Indus River floodplain. The earthquake was accompanied by coseismic folding accommodated by flexural slip along an active axial surface. The deformation is captured at the temporal resolution afforded by the radar acquisitions, which includes between 10 and 18 days of potential postseismic deformation. Despite this short period of observation, flexural slip is tantamount to 70% of the expected value for coseismic folding, indicating strong mechanical coupling and synchronicity between faulting and folding at the time scales of the seismic cycle. While the Dajal earthquake demonstrates the seismic potential of the deformation front of fold-and-thrust belts, the folded sediments above the blind ramp exert a strong control on the rupture propagation. Further seismic exploration of fold-and-thrust belts will be crucial to anticipate the location and size of future seismicity in this widespread tectonic setting.

The western zone of the SFT belt exhibits high seismic hazard. The full understanding of the high magnitude seismicity is lacking due to complex tectonic settings, and the lack of a GNSS and seismic stations network. Here, we take advantage of the Sentinel-1, and ALOS-2 ScanSAR satellite observations to estimate the coseismic deformation caused by the 2021 Mw 6.0 Harnai earthquake. The coseismic surface deformation along the line-of-sight (LOS) is estimated as 70 mm and 80 mm for ascending and descending interferograms, respectively. Modeling of InSAR data reveals primarily thrust-dominated slip in up dip direction with a strike-slip component that is in good agreement with the tectonic context of the transpressional Karahi and Harnai faults. Source fault geometry along with the corresponding uncertainty of the 2021 Mw 6.0 Harnai earthquake and preseismic InSAR derived movement (Karaca et al., 2021) shows the fault was locked until 2021, prior to the rupture. The finite slip models show that 95% of slip is concentrated between 3 and 10 km depth. The NW-SE oriented rupture rather than the NE-SW oriented model is justified by the tectonic setting and fault structure of the Harnai fault. Major deformation is observed in the hanging wall at the southern block of the Harnai fault. This study helps to understand the crustal deformation mechanism at the western margin of the SFT belt.

Furthermore, we worked at the EAF system which accommodates the northward movement of the Arabian plate into the Anatolian plate. The convergence

forms a triple junction slip partitioning among the NAF, the EAF, and the faults of the Turkish-Iranian Plateau. The NAF is a 1,200 km long right-lateral strike-slip fault extending from the Karliova triple junction to the Sea of Marmara. The EAF is a 310 km long left-lateral fault, that extends southwards and branches out diffusely to Antakya, the Dead Sea Fault (DSF), and the Cyprus Arc to the southwest. The NAF is considered structurally mature while the EAF is structurally immature because it consists of multiple fault segments. These fault segments rupture over time, and long-term accumulated strain energy is released by bends and step over structures that connect the EAF system. A significant portion of the EAF system has ruptured in the last few years, as demonstrated by the recent activity starting with the January 24, 2020, Mw 6.8 Elazığ earthquake, near Hazir Lake, continuing with the February 06, 2023, Mw 7.8 Kahramanmaraş earthquake that ruptured the 310 km long Erkenek, Pazarcik, and Amanos contiguous fault segments. On the same day 9 hours later, the Mw 7.6 earthquake ruptured the 150 km long left lateral splay of the EAF. Two weeks later on February 20, another aftershock with Mw 6.4 occurred in Antakya at the southern termination of the EAF. In this study, coseismic slip distribution of the 2023 Mw 7.8 Kahramanmaraş, the Mw 7.6 Elbistan, and Mw 6.4 Antakya aftershocks is constrained using remote sensing observations. The finite fault rupture inversion which I accomplished in this PhD study is part of an international effort to collect multi-parametric spaceborne geodetic data to determine the coseismic slip distribution of the 2023 earthquake sequence.

Based on the estimated coseismic slip distribution, the 2023 mainshock rupture propagated bilaterally from the central Pazarcik segment. To the north, the rupture terminated near the bifurcation with the Bitlis-Zagros fold-and-thrust-belt. As a result, a 40 km long segment separating the 2020 Elazığ and the 2023 Kahramanmaraş ruptures did not slip during the earthquakes. The EAF features creeping segments to north, near the Karliova triple junction and around Hazir Lake in the Palu and Pütürge segments, but is locked during the interseismic cycle in the remaining segments. We speculate that this section of the EAF represents a seismic gap. Alarmingly, the Pütürge segment remains unbroken, bearing the potential for another significant earthquake. To test this hypothesis, we further investigate the fault behavior before the 2023 Kahramanmaraş earthquake sequence. We perform time series analysis using Sentinel-1 SAR interferometry to identify the extent of creep along the EAF, particularly along the 40 km long Pütürge segment. We process the ascending tracks AT116, and AT43, along with the descending tracks DT123 and DT21 using the small baseline (SBAS) inversion algorithm. We use 147 interferograms for track AT116, 85 for track AT43, 120 for track DT123, and 145 for track DT21. As a preliminary step, we stack the geocoded unwrapped interferograms, and remove the unwrap

errors for each interferogram. We then utilize the ECMWF ERA5 products to reduce the tropospheric phase delays. Finally, we correct the phase ramps, DEM errors, and estimate the average velocity. The results indicate the presence of up to 20 mm/yr shallow creep along the EAF after the coseismic deformation of the 2020 Mw 6.8 Elazığ earthquake, which propagates towards the southwestern end of the Pütürge segment. We also find creep at many small segments of the EAF zone from Pütürge segment to the Karliova triple junction. This study clarifies the seismic potential of the Pütürge segment. The first part of the work, concerning the finite fault inversion, has been published in (Barbot et al., 2023), whereas the work on the creep analysis on Pütürge segment is being prepared for publication.

Acknowledgements

Starting with the name of ALLAH who is the most kind and merciful. Almighty ALLAH is The One, Grestest, The Everlasting, Who begets none, is be gotten, by no one, and there is none His equal. ALHAMDULILLAH. I bear witness that the Holy Prophet Muhammad (PBUH) is the last messenger, who always promoted peace, his life is the perfect example for humanity till the Day of Judgment. I am grateful to Allah for giving me strength and blessings in completing this thesis. I am nothing without His help. Please keep me always in prostration before you and let me not leave before anyone except you.

The completion of this doctoral project would have been impossible without the exceptional support, both scientific and personal, of numerous individuals. This doctoral journey, like many others, has been significantly enhanced by the contributions of individuals who have provided guidance, encouragement, and unwavering support throughout the process.

First of all, I am deeply grateful to my both supervisors, Prof. Carla Braitenberg, and Prof. Sylvain Barbot for their invaluable guidance throughout my research journey. Their mentorship has been instrumental in shaping my understanding of earthquake science and has inspired me to pursue further research in this field. Prof. Carla has consistently demonstrated unwavering support and assistance throughout my research journey, particularly during challenging times. I am deeply grateful for her unwavering belief in my capabilities and her guidance in steering the research in the right direction. I am immensely thankful to her for providing me with this exceptional opportunity to work with her.

I am immensely grateful to Professor Sylvain Barbot for his unwavering dedication, time, and expertise in understanding, reviewing my results, and providing prompt assistance whenever needed. Professor Sylvain's work has significantly enhanced my understanding of earthquake phenomena and their modeling. His profound knowledge of earthquake modeling and unwavering support throughout my PhD studies have been instrumental in achieving significant outcomes. His contributions have had an unparalleled impact on my

Ph.D. project. My utmost sincere gratitude to him for providing his unwavering support and guidance, which have kept my research on the right track.

I would then like to thank Dr. Farhan who always stands by me to understand the earthquake phenomena, and modeling through inversions. I ought to extend my gratitude to the Tectonophysics and Geodynamics section. Dr. Alberto, who manages the Server, and HPC, and is always eager to resolve and help with the installation of new modules and software on a virtual machine.

Yet as importantly, I thank all the lab mates in this building of *Palazzina C*, for all the opportunities for discussion, prolific arguing, and mutual advice through the last years, both in the office and remotely: Alberto, Tommaso, Marco, Anna, and anyone I may have forgotten.

I am especially grateful for the prayers and efforts of my whole family back in Pakistan, especially my parents ("Abu, Ami": what I call them in my local language) and brothers (Aamir, Ansar, and Amjid families) for their support, encouragement, sacrifices, endless love, and prayers throughout my life.

I am highly indebted to my gorgeous and marvelous wife Sobia for her myriad support, affection, calmness, and prayers. Her continuous support and sacrifices during difficult times enabled me to work hard with a focus and achieve my goals. Her presence in my life and this journey have had a great impact on completing my research. She is always there for me, no matter what. I am so grateful for her in my life. It is also important to mention the love of my beautiful son Rayyan, who fills my life with joy and adventure. His sparkling eyes, beautiful smile, and warm hugs chase away any stress or tiredness.

I acknowledge the Ph.D. project is financed through the Maria Zadro legacy to the University of Trieste, Italy. I am grateful to the university administration, and Ph.D. coordinator, Prof. Maset Stefano, for his prompt responses to queries and support for managing our missions for international conferences, and workshops. I am very thankful to the external reviewers, Dr. Tommaso Pivetta and Dr. Mimmo Palano, for their invaluable time in reviewing my Ph.D. dissertation. Their insightful suggestions have significantly enhanced the quality and depth of my final Ph.D. dissertation.

I used GMTSAR (Sandwell et al., 2011), MintPy (Yunjun et al., 2019), LiCSBAS (Morishita et al., 2020) to process the Sentinel-1 data and obtained most of the maps presented in the thesis Generic Mapping Tools (GMT, Wessel et al., 2013), and the Matlab toolbox (Wessel and Luis, 2017). In addition, I mostly used the DMG server resources to process the SAR data, I express my gratitude, acknowledge, and thank all the producers cited in this work.

Dedication

I wholeheartedly dedicate my doctoral achievement to my beloved father, Ghulam Rasool, and mother, Nazia Ghulam Rasool, as well as to my entire family. Throughout my academic journey, your unwavering love, support, and encouragement have been my guiding light. Your sacrifices, both seen and unseen, have made this accomplishment possible. Thank you for believing in me, for inspiring me to attain my Ph.D. qualification, and for instilling in me the values of perseverance and determination. This work stands as a tribute to your endless dedication and the immeasurable impact you've had on my life. With deepest gratitude.

1 Introduction

1.1 Introduction

Geodetic observations provide insights into the kinematics of continental and oceanic tectonic plates at global and regional scales. Space geodesy enables us to monitor the deformation style, and characterize the temporal and spatial variation (Gordon and S. Stein, 1992; S. Stein, 1993). The fault systems in complicated trans-compressional regimes are mostly characterized by fault bends, and step-over structures along main faults (Barka and Kadinsky, 1988; Yule and Sieh, 2003). Several notable examples of such active complex fault systems include the Gargano fault system in the central Adriatic region in Italy, the East Anatolian fault (EAF) and North Anatolian fault (NAF) systems in Turkey, the Marlborough fault system in New Zealand, the San Andreas fault system in the United States, and the Sulaiman Fold thrust (SFT) belt in Pakistan, all of which are known for high seismicity (Barbot et al., 2013; Barbot et al., 2023; Barka, 1996; Billi et al., 2007; Cakir et al., 2023; Chiarabba et al., 2005; Javed et al., 2022; Konca et al., 2021; Tatar et al., 2012). The complicated fault geometries in trans-compressional regions are considered to affect the nucleation and rupture propagation that ultimately controls the triggering of an earthquake (Javed et al., 2022; Lapusta and Rice, 2003; Wesnousky, 2006). Recently, the 2016 Mw 7.8 Kaikoura earthquake occurred on the Marlborough branching fault system that ruptured 21 faults and produced approximately 10 m coseismic surface displacement (W. Xu et al., 2018). Global Navigation Satellite System (GNSS) and Synthetic Aperture Radar (InSAR) Interferometry help us to investigate sources of complicated tectonic processes and the structure of the deforming elastic, and viscoelastic crust accurately from global to regional scale (Agata et al., 2019; Feng et al., 2015; Nissen et al., 2016; Rollins et al., 2018).

We use remote sensing SAR observations to understand the slow and complex deformation processes involved at the western boundary of the Indian-Eurasian plates. The relative motion between tectonic plates is accommodated across wide fault zones. Yet, how these deformation zones grow over time is poorly known. We investigate the SFT belt, Pakistan at the plate boundary between the Indian and Eurasian continents in order to better assess the seismic potential. A key question that needs to be addressed is why moderate-size seismicity was

observed along the eastern zone, as opposed to the western zone of the SFT belt. Do geometric complexities or fault dimensions exist in the eastern SFT belt zone that control the coseismic slip propagation, size of magnitude as suggested in several articles (Namson and T. L. Davis, 1988; Sathiakumar and Barbot, 2021; Sathiakumar et al., 2020; H. Wang et al., 2017; Weng and Yang, 2017)? InSAR helps us to estimate the crustal deformation induced by the 2015 Mw 5.7 Dajal earthquake at the eastern margin of the SFT. The rupture did not reach the surface at the eastern extension of the SFT, buried under the younger sediments of the Indus River floodplain. The rupture and associated folding in the hanging wall documents the eastward growth of the SFT. These observations document the seismic potential of hidden ramps in fold-and-thrust belts and the control of final rupture size by fault bends and surrounding folds.

Furthermore, We use C-band Sentinel-1, and L-band Advanced Land Observing Satellite (ALOS-2) ScanSAR data to investigate the complicated processes involved during coseismic deformation caused by 2021 Mw 6.0 in the western SFT belt. We use ALOS-2 and Sentinel-1 data to perform the fault movement inversion using a Bayesian approach to investigate the coseismic deformation and slip distribution on the inverted fault dimensions. The earthquake occurred on 06 October 2021 with Mw 6.0 earthquake near Harnai on a trans-pressional margin of the western zone of the SFT belt, providing an opportunity to study the interaction of coseismic slip and folding within the most active seismic of the SFT belt. We explore InSAR data to derive the coseismic deformation and source parameters such as dip, strike, depth, width, length, average slip, strike and dip, and related surface deformation of the earthquake.

The accurate earthquake source parameters play a key role to insight lithospheric of SFT belts at the convergence of Indian-Eurasian plates. The computation of source parameters using the InSAR dataset has been proven as an accurate and additional method to learn more about the mechanism of earthquakes (Barbot et al., 2008; Barbot et al., 2023; Javed et al., 2022; Mellors et al., 2004; Nissen et al., 2016) and compare their corresponding source parameters and enhance the accuracy of the results (Barkat et al., 2022; Tatar et al., 2020; Weston et al., 2012). Ultimately, the comparison provides a higher certainty level of source parameters computed from different datasets that significantly improve the accuracy of seismic hazards assessment. The mechanism and style of deformation at the western boundary of the Indian-Eurasian plates are not very well known due to the lack of seismic stations and GNSS networks. Therefore, the identification of seismic source parameters of the 2015 Mw 5.6 and the 2021 Mw 6.0 earthquakes would provide a significant contribution to understanding the regional style of deformation of the tectonically active SFT belt.

In addition, we also work on the complex deformation processes involved around the immature EAF system at the convergence of the Anatolian and

Arabian plates using remote sensing data. The EAF remained locked until the recent seismic activity starting with the January 24, 2020, Mw 6.8 Elazığ earthquake, near Hazir Lake, continuing with the February 06, 2023, Mw 7.8 Kahramanmaraş earthquake that ruptured the 310 km long Erkenek, Pazarcik, and Amanos contiguous fault segments. On the same, day 9 hours later, the Mw 7.6 earthquake ruptured the 150 km long left-lateral splay of the EAF. Two weeks later on February 20, another aftershock with Mw 6.4 occurred in Antakya at the southern termination of the EAF system. The finite fault rupture inversion that we accomplished in this Ph.D. study is part of an international effort to collect multi-parametric spaceborne satellite observations to constrain the spatial distribution of the coseismic slip for the 2023 earthquake sequence.

Further, we analyze the time evolution of the deformation of the EAF, with the aim to detect creep over segments of the EAF from the Pütürge segment to the Karliova triple junction. In order to estimate the earthquake potential at Pütürge segment, we estimate the creep rates using Sentinel-1 data to perform analysis through Small Baseline Subset (SBAS) (Hooper, 2008; Morishita et al., 2020; Yunjun et al., 2019) inversion techniques to compute the rates of deformation using the selected interferograms that have high coherence and small perpendicular and temporal baselines. Space geodesy is a dominating tool for investigating the deformation mechanism, however, there are also some limitations (ionospheric and tropospheric delays). The effect of atmospheric heterogeneities (Zebker and Villasenor, 1992) are reduced with the aid of independent sources such as Generic Atmospheric Correction Online Service (GACOS), European Centre for Medium-Range Weather Forecasts (ECMWF) ERA5, Global Position System (GPS) based corrections and numerical weather models (Hanssen et al., 1999; Z. Li et al., 2011). Ultimately, the use of these models improves the resolution and correlation of InSAR by reducing the atmospheric effects.

1.2 Research Objectives

These are the following primary objectives of the thesis.

- To understand the slow and complex deformation processes and structures involved at the western boundary of the Indian and Eurasian plates at the front of the SFT belt.

- To estimate the coseismic deformation induced by the 2015 Mw 5.7 Dajal, and 2021 Mw 6.0 Harnai earthquakes at the front and western zone of the SFT belt, and model the ruptured fault parameters using the geodetic Bayesian inversion approach.

- To determine the slip distributions of the 2015 Mw 5.7 Dajal and 2021 Mw 6.0 Harnai earthquakes on the frontal ramp and of flexural slip along active axial surfaces for the forward- and backward-verging two end-member models: a double fault-bend fold system and a fault-propagation fold. The fault-bend fold involves décollement-ramp-décollement along with associated active axial surfaces, fault-propagation fold involves a décollement branches into a shallow ramp.

- To estimate the coseismic deformation generated by the February 6 2023 Mw 7.8 Kahramanmaraş mainshock and the Mw 7.6 Elbistan, and February 20 2023 Mw 6.4 Antakya aftershock. Find the slip distribution on the multiple segments of the left-lateral EAF system ruptured during the 2023 Turkey earthquake sequence.

- To analyze the distribution of shallow creep prior to the 2023 Turkey earthquake sequence on the EAF from the Pütürge segment to the Karliova triple junction. The Mw 7.8 Kahramanmaraş mainshock, rupture propagation stopped southward at the diffuse termination of the EAF and tapered off northward into the Pütürge segment, some 20 km south of the 2020 Mw 6.8 Elazığ earthquake. As a result, a 40 km long segment separating the 2020 Elazığ and the 2023 Kahramanmaraş ruptures did not slip during an earthquake. We speculate that this section of the EAF represents a seismic gap. To test this hypothesis, we investigate the fault behavior before the 2023 Kahramanmaraş sequence. Analyzing the post-seismic deformation of the 2020 Mw 6.8 Elazığ earthquake on the EAF zone would clarify the seismic potential at the Pütürge segment.

2 Crustal Deformation and Principle of InSAR

2.1 Introduction

Spaceborne geodesy has played a major role in improving our ability to insight into the earthquake cycle by continuously monitoring the deformation at the tectonic plate boundaries and major faults. The space geodetic data from GNSS and InSAR continually monitor the complex network of faults and diffuse plate boundaries, providing valuable insights into the mechanisms underlying crustal deformation at the seismic scale (Barbot et al., 2023; Segall and J. L. Davis, 1997). The InSAR and GNSS tools are currently the most dominating tools that provide continuous monitoring of complicated faults to update the hazard assessment of a particular area. However, the GNSS instruments need to be installed across the faults and continuous monitoring of the instrument at the site is also required to avoid any damage. On the other hand, InSAR has a special ability to study the whole globe with high precision, especially in remote areas that are not accessible to install instruments. The InSAR provides cumulative displacement between the acquisition dates at a much higher spatial coverage than GPS (Samsonov and Tiampo, 2006).

The GNSS satellites include the EU Galileo, the US GPS, and the Russia Federation Global Navigation Satellite System (GLONASS) among others. The satellites continuously broadcast a code having the information of the precise position, navigation, and time of the satellite. If we have a constellation of four GPS satellites, we can correct the timing error, and accurately measure the position of our GPS antenna anywhere on Earth up to the precision of several meters, however, not enough to account for the slow deforming tectonic plates accurately which may require the precision up to order of mm/year. However, instead of using a code, we can track the carrier waves. The phase data from a constellation of multiple satellites over time aids us in calculating accurate positions with the precision of up to the order of millimeters (Blewitt, 2007; Elliott et al., 2016).

We now have a great network of the GNSS instruments containing many thousands of regular continuous GPS stations all over the globe. The network

coverage has been growing further improving accuracy, and measuring the velocities, and strain rates on individual points. Still, there are large gaps in the continental coverage of the GNSS network to compute tectonic velocities, especially in underdeveloped and developing countries, such as Pakistan which cannot afford the costs of installation and maintenance of the GNSS network. Non-availability of the dense network may not provide accuracy in distinguishing the steady creep from a locked fault. Along with the GNSS network, the SAR satellites dramatically improve our ability to measure the deforming fault zones up to millimeter precision and construct the complete picture of the earthquake cycle. The SAR satellite technology enables us to measure surface deformation with a spatial coverage of a few kilometers up to a precision of 1 mm without any specific instrument on the ground (Barbot et al., 2023; Javed et al., 2022; Segall and J. L. Davis, 1997).

2.2 Synthetic Aperture Radar Satellites

SAR satellites transmit the microwaves on the earth's surface and record the backscattered energy from the target at any time of the night or day in all weather conditions. These satellites use microwaves that have the capability to penetrate through clouds and record images containing phase and amplitude information. The SAR satellites calculate the distance between the SAR sensor and the target by analyzing the phase of radar signals, taking into account the acquisition time and satellite position. There are now multiple SAR satellites revolving around the earth in specific orbits and monitoring the land surface (Figure 2.1).

We often use two observations from SAR satellites before, and after an event to estimate the deformation caused by earthquakes, volcanoes, and landslides, or time series to monitor the tectonic plate movement in time. Based on the satellite positions, amplitude, and phase differences of the two observations of the same target, we can compute the land surface deformation along the LOS direction. In this thesis, for studies discussed in Chapter 3, Chapter 4, and Chapter 5, we use the European Space Agency (ESA) Sentinel-1 and the Japan Aerospace Exploration Agency (JAXA) ALOS-2 satellite observations (Figure 2.1).

2.2.1 European Space Agency Sentinel-1 Satellites

Copernicus Sentinel-1 was initially designed based on Sentinel-1A, and -1B. The Sentinel -1A and -1B with an open data policy were launched on 3rd April 2014 and 25th April 2016, respectively. Both satellites are sun-synchronous with

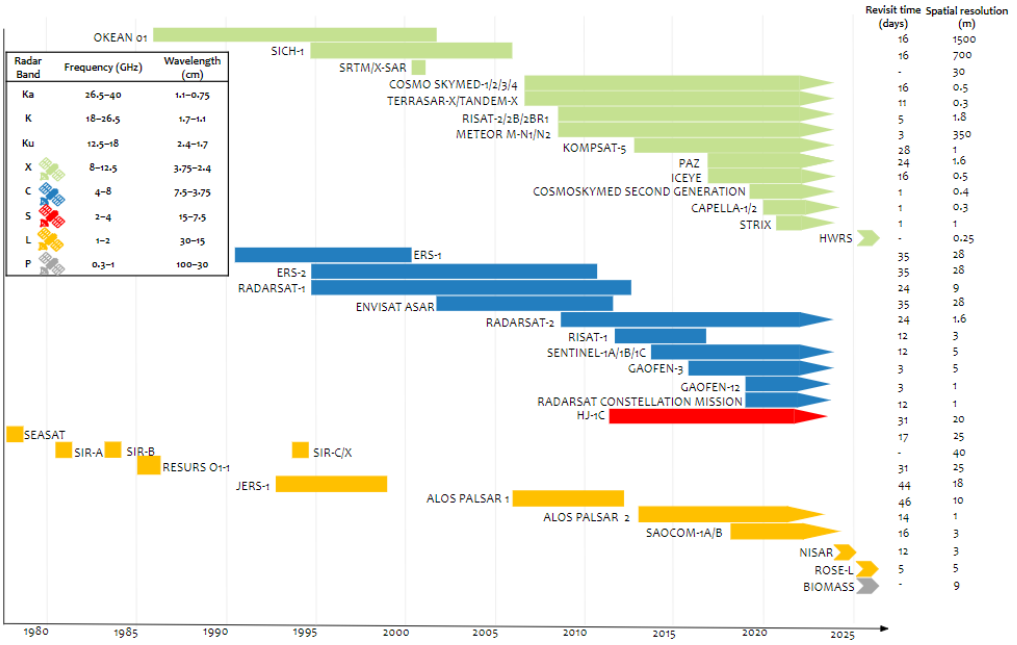

Figure 2.1: The launched and proposed SAR satellite missions operating using different frequencies of microwaves. We specifically used the C-band (5.3 GHz) Sentinel-1A/1B and the L-band (1.2 GHz) ALOS-2 satellites (https://detektia.com/en/sar-synthetic-aperture-radar/).

a 12-day revisit period for each satellite. By combining Sentinel-1A and 1B, the revisit period was reduced to 6 days. Unfortunately, Sentinel-1B stopped delivering data from December 23 2021 due to an electronic power supply problem at the satellite platform. The SAR satellite mounted a C-band (f = 4-8 GHz) instrument that operates with single and dual polarization (HH, VV, HV, VH). The satellite acquires images in Interferometric Wide (IW), Strip map (SM), Wave (WV), and Extra Wide (EW) modes as shown in Figure 2.2. Each acquisition mode was designed to monitor the specific features on the ground surface. The IW mode is widely used to monitor the surface deformation caused by earthquakes, landslides, fault movement, glacier velocities, and volcanic eruptions. The coverage of the IW is about 250 km wide with a geometric resolution of 5×20 m^2. The IW swath mode records images in three subswaths in TOPS mode (Figure 2.3). The microwave beam is steered in the range direction, and forward and backward in the flight direction, referred to as the azimuth direction. The technique ensures a sufficient overlap region for each burst that is mandatory to remove scalloping and obtain an admirable image with feasible coherence.

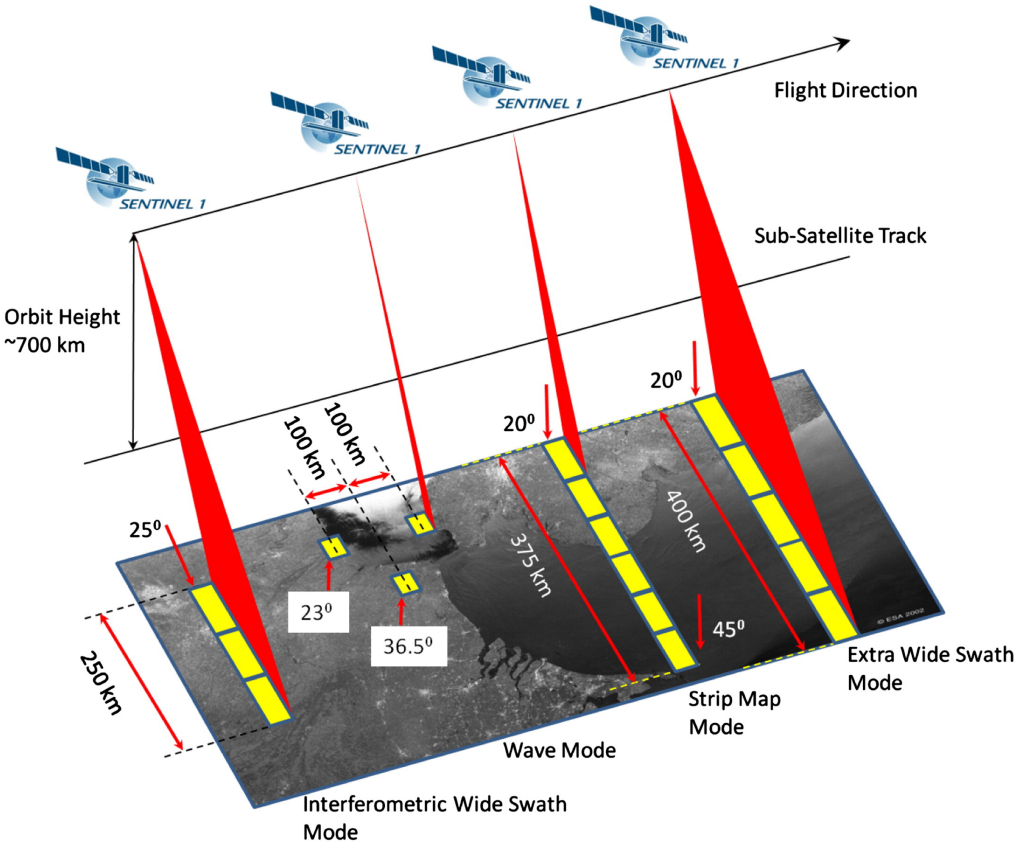

Figure 2.2: Sentinel-1 satellite acquisition modes. The acquisition difference of Extra Wide swath (EW), Strip map (SM), Interferometric Wide (IW) and, Wave (WV) of the Seintinel-1 satellite. The image modified from (https://sentinels.copernicus.eu/web/sentinel/missions/sentinel-1/instrument-payload).

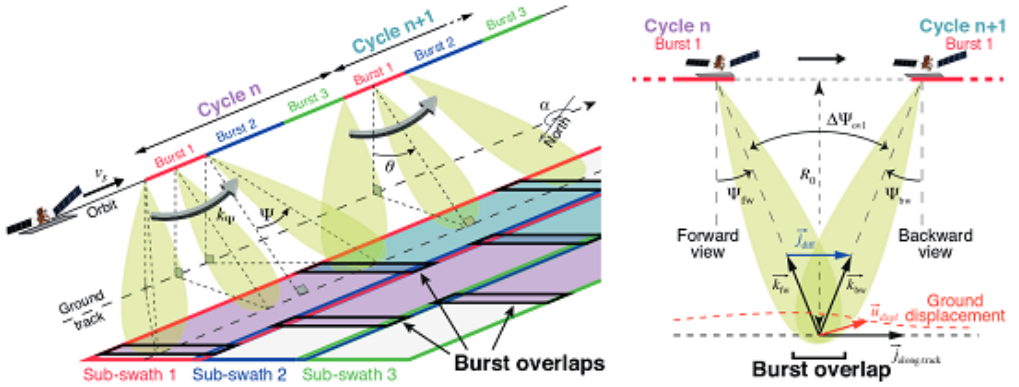

Figure 2.3: Sentinel-1 TOPS mode acquisition in subwath 1, 2 and 3 with burst 1, 2, and 3 along with burst overlap (Grandin et al., 2016).

2.2.2 Advanced Land Observing Satellites (ALOS)

The L-band ALOS-1/Daichi-1, was launched by JAXA in 2006. However, after 5 years, the satellite lost power due to technical problems, thus aborting the mission. Following ALOS-1, JAXA launched the ALOS-2 in 2014. The satellite was equipped with a Phased Array L-Band (PALSAR-2) with $\lambda = 24\,cm$ and $f = 1.2$ GHz. It has a great capability to penetrate through leaves and therefore has a better coherence as compared to X, and C bands satellites in forests, or agricultural regions. PALSAR-2 has a revisit time of 14 days, and acquires images in three acquisition modes, Spotlight (SPT): acquires 25 km wide observations with a resolution of 1 - 3 m, Stripmap (SM): acquires 50 - 70 km wide observations with 3 - 10 m resolution, and ScanSAR (WD) mode: acquires 350 - 490 km wide observations with 60 - 100 m resolution.

2.3 SAR Complex Image and Resolution

The SAR image composed of many small elements that are known as pixels, carries information of the phase and amplitude of the backscattered microwaves from the earth's surface. The backscattered signal is stored in the two-dimensional array of rows and columns. The rows are associated with azimuth observations (along radar flight direction), while the columns are associated with the slant range observations. The amplitude is calculated based on the backscattered microwaves from Earth's surface. The strong amplitude or bright pixels indicate the exposed rocks, lack of vegetation, and buildings in the urban areas, while the low amplitude or dark pixels could be an indication of the vegetation, water basin, or flat surfaces (Figure 2.4).

The Radar transmits signals from antenna to the ground surface and records backscattered signals from each pixel on the ground. Since each pixel is at a different distance from the radar, that produces different delays. However, the delay time (τ) becomes equal to the phase changes (ϕ) due to the sinusoidal signal. Thus, the phase changes (ϕ) can be defined using the following equation based on the wavelength of the radiations ($\lambda = 5.66$ cm for C-band) and two-way travel distance ($2R$) between radar antenna and ground surface:

$$\phi = \frac{2\pi}{\lambda} 2R = \frac{4\pi}{\lambda} R. \tag{2.1}$$

2.3.1 Ground Resolution Cell

The smallest area on the ground that can be distinguished in a SAR image is called the ground resolution cell. The size of the ground resolution cell

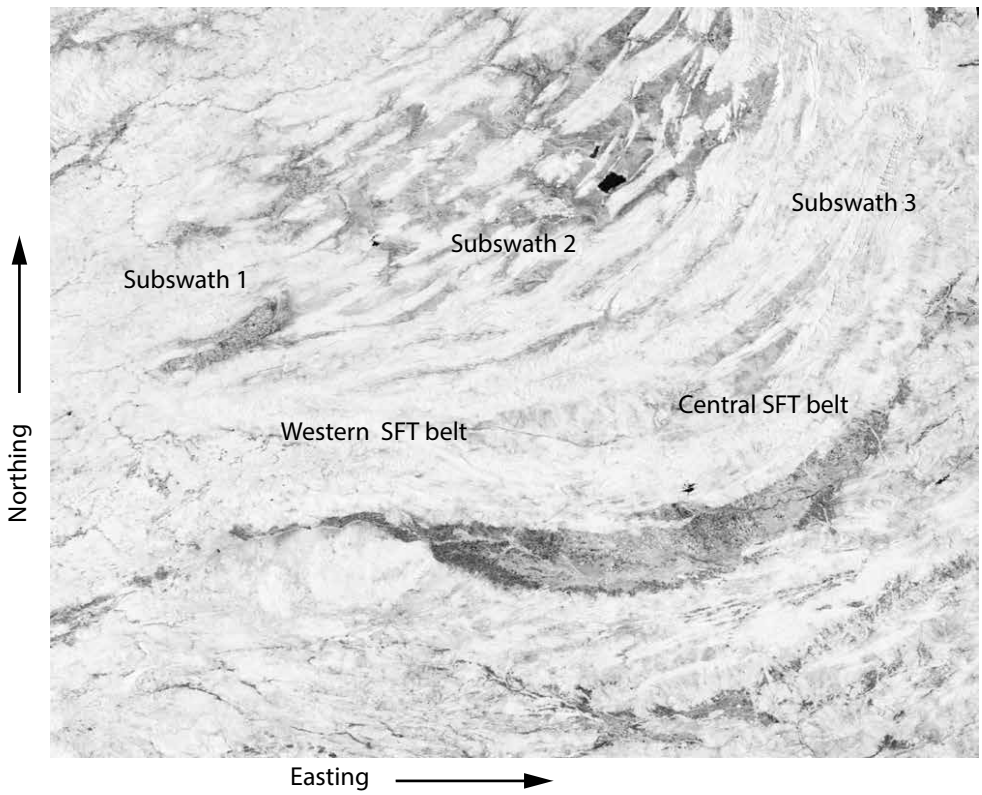

Figure 2.4: SAR image of Sentinel-1 satellite showing the backscattered signal on the Sulaiman Fold and thrust (SFT) belt at the Indian-Eurasian plates boundary zone. The bright pixels indicate the exposed rocks while the dark pixels indicate the vegetation, trees, and flat surfaces as lakes.

is determined by the slope of the topography in the azimuth direction and perpendicular plane to the ground range direction. Since the ground resolution cell depends on the terrain slopes, scatterers on the ground can be affected by foreshortening and layover. When the terrain gradient is increased compared to a flat surface, the ground resolution cell dimensions also increase and cause shortening. Further, when topographic gradient exceeds or lags behind the satellite off-nadir angle, eventually signals from multiple cells are superimposed to a single ground resolution cell that produces layover (Ferretti et al., 2007) (Figure 2.5a, b). In contrast, when the terrain gradient decreases, the resolution cell dimension also decreases. The minimum resolution cell dimension (i.e., equal to the slant range resolution) is reached when the terrain gradient is parallel to the LOS. This is also the lower gradient limit that can be imaged by a SAR, as beyond this angle, the terrain is in shadow (Figure 2.5a, b).

When terrain slope decreases, the resolution cell dimension decreases.

2.3.2 Azimuth and Range Resolution

The resolution of SAR images is determined by the azimuth and range resolution. The range resolution is defined by slant range and ground range resolution. We represent the slant range resolution by ΔR_s which is defined by the speed of light (c), and radar pulse-length (τ). We represent the the ground range with R_g, which is determined by the slant range resolution (ΔR_s) and radar look angle (θ) (Brown and Porcello, 1969) as

$$\Delta R_s = \frac{c\tau}{2}, \tag{2.2}$$

$$R_g = \frac{\Delta R_s}{sin\theta}. \tag{2.3}$$

The azimuth resolution (Δ L) can be defined by the radar wavelength (λ), antenna length (L), and slant range(ρ) (Brown and Porcello, 1969)

$$\Delta L = \frac{\lambda\rho}{L}. \tag{2.4}$$

In order to improve the azimuth resolution, the antenna length should be very large. However, the antenna length of the radar is limited to tens of meters. The limitation of antenna length is handled by the Synthetic Aperture Radar (SAR) approach in which multiple small antennas are mounted on the Radar which record backscattered signals on multiple positions along the flight direction of the satellite. So, the azimuth resolution of SAR becomes half of the antenna length $\Delta L = \frac{L}{2}$ (Zink, 2002) (Figure 2.6).

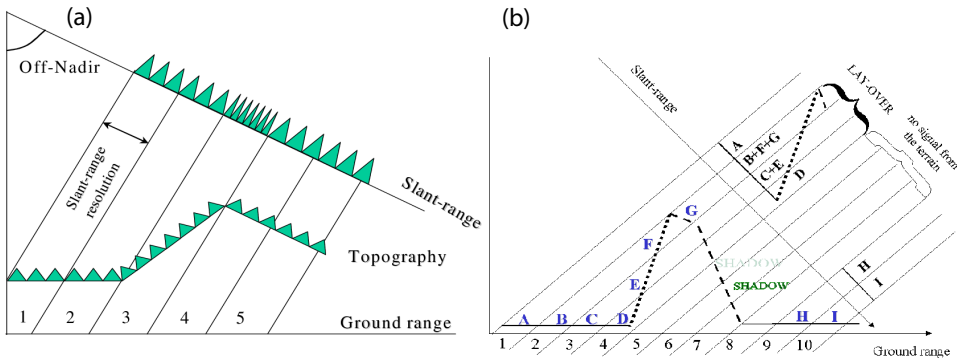

Figure 2.5: Effect of topography on SAR image acquisition. (a) Slant range resolution is affected by topographic gradient. (b) The positive topographic gradient incorporates the layover effect and the negative gradient produces a shadow zone (Ferretti et al., 2007).

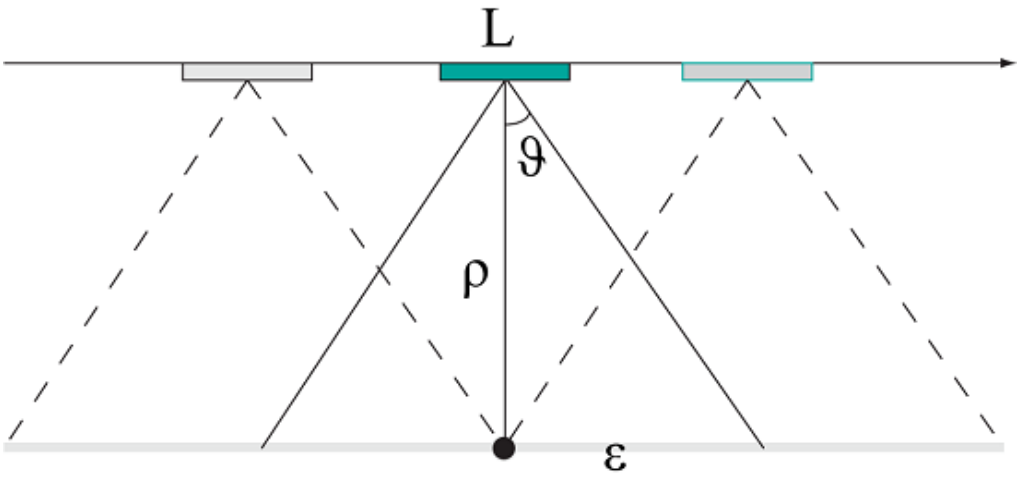

Figure 2.6: Scketch of Synthetic Aperture Radar (SAR) antennas mounted on the Radar which record backscattered signals on multiple positions along the flight direction of the satellite. Here ρ is the distance between the illuminted targeted ground surface and the antenna, ε is half illuminated ground length, and ϑ is the pulse angle (Ferretti et al., 2007).

2.4 SAR Interferometry and Processing Techniques

The Sentinel-1 satellite revisits the same area after 12 days and records the ground surface information from a slightly different position (Figure 2.7). The position of the satellites is obtained by the satellite orbits. The shortest distance between both satellite positions is known as the interferometric baseline (B) (Besoya et al., 2021; Ferretti et al., 2007) (Figure 2.7). The time difference between both observations is called the temporal baseline, while a perpendicular (Bn) baseline is determined by the normal projection of the interferometric baseline on the slant range (Figure 2.7). SAR images record the ground surface information based on the backscattered signal as amplitude and phase. An interferogram is produced through an interferometric phase of two SAR images to estimate the deformation in the LOS direction (Bamler and Hartl, 1998; Javed et al., 2022).

2.4.1 Interferometric Phase

The phase of each SAR image pixel is defined in equation 2.1. The interferometric Phase is defined as the double difference between two single-look complex (SLC) SAR phases (equation 2.5) assuming both satellites cover the same area of interest with almost similar geometry. The interferometric phase is calculated by using the following equation;

$$\begin{aligned} \phi_{int} = \phi_2 - \phi_1 &= \frac{2\pi}{\lambda} 2R_2 - \frac{2\pi}{\lambda} 2R_1, \\ &= 2\frac{2\pi}{\lambda}(R_2 - R_1). \end{aligned} \tag{2.5}$$

The interferometric phase (ϕ_{int}) includes the deformation phase ($\phi_{deformation}$) due to fault movement, topographic phase ($\phi_{topographic}$), orbital phase ($\phi_{orbital}$) noise if precise orbit information is not available, atmospheric phase ($\phi_{atmospheric}$) errors due to upper and lower atmospheric delays, and unwrap phase (ϕ_{unwrap}) noise during the InSAR data processing ;

$$\phi_{int} = \phi_{deformation} + \phi_{topographic} + \phi_{orbital} + \phi_{atmospheric} + \phi_{unwrap}. \tag{2.6}$$

Note that the interferometric-phase (ϕ_{int}) is a cumulative phase change between two SAR acquisitions. To compute the phase changes caused by a tectonic activity such as an earthquake, fault movement, landslides, and volcanoes, we need to remove the contributions of topographic, atmospheric turbulence, and satellite orbit errors to estimate accurate LOS displacement.

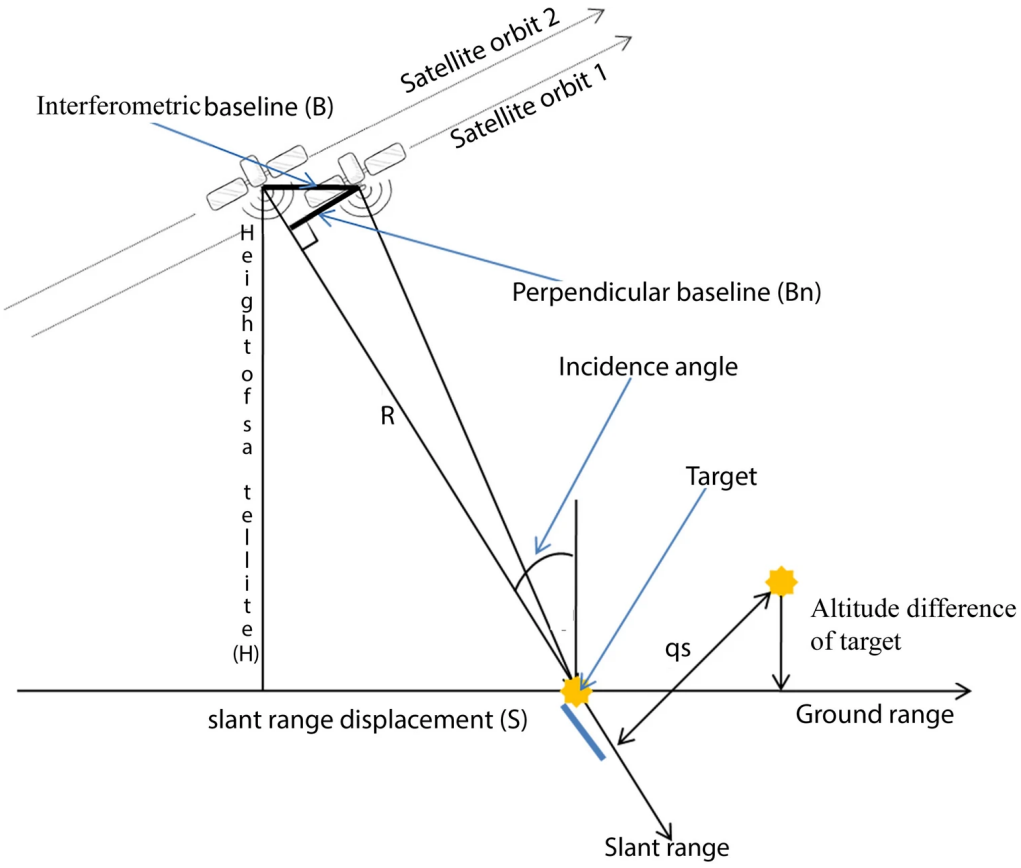

Figure 2.7: The geometry of InSAR satellites used to obtain an interferogram using two SAR satellites to monitor the surface deformation along the line-of-sight direction (Besoya et al., 2021; Ferretti et al., 2007).

2.4.1.1 Topographic Phase

The topographic phase is part of the InSAR signal, that is removed to accurately measure deformation along the LOS direction (Massonnet and Feigl, 1998; Massonnet et al., 1997; Zebker et al., 1994). The topographic phase is removed from the interferometric phase, for instance using the Shuttle Radar Topography Mission (SRTM) DEM models, however, it can also be done by using multiple interferograms. The DEM method is simpler to implement, however, it is less accurate if the DEM is not of high quality over mountainous regions. The multiple interferogram method is more accurate by having different perpendicular baselines that allow us to separate the topographic phase from the deformation phase, but it is also more complex to implement (Zebker and Goldstein, 1986). An example of topographic noise is shown in Figure 2.8.

2.4.1.2 Atmospheric Phase Errors

Atmospheric phase errors are still a major concern in the InSAR deformation measurements because their contribution can produce a significant phase shift in the interferogram. These delays are caused by spatio-temporal turbulence in the water vapor content, and atmospheric pressure in the lower atmosphere, and the stratification of the atmospheric column. The pressure is there in any case- it decreases from the surface to greater heights (Z. Li et al., 2006; Z. Li et al., 2012; Zebker et al., 1997). Since SAR satellite images are acquired at different times, the radiations can be affected by varying atmospheric conditions. Therefore, it is essential to remove atmospheric delays from InSAR data before estimating surface deformation. These delays are generally divided into tropospheric phase delays and ionospheric phase delays. Tropospheric phase delays are caused by water vapor content or humidity, pressure, and temperature in the lower atmosphere. These noise effects can be removed using a variety of methods, such as the ERA5 reanalysis dataset, GACOS (Yu et al., 2018b), or numerical weather models. However, the accuracy of numerical weather models can vary, depending on the region and the time of year.

The ionosphere is mainly composed of ions and free electrons. The density of electrons (TEC) is subjected to the geographic location, the sun's activity, and the orientation of the geomagnetic field (Shim et al., 2008). The turbulence of the TEC can also occur due to magnetic storms. However, the ionosphere interacts with the microwave radiations significantly especially for L- and X-band satellites, and affects the precision of surface deformation measurements (Figure 2.9). The application of ionospheric correction is mostly done by split spectrum filters (Gomba et al., 2015). However, GACOS and ERA5 can also be used to correct the ionospheric delays. The choice of atmospheric correction method will depend on several factors, such as the availability of data, the

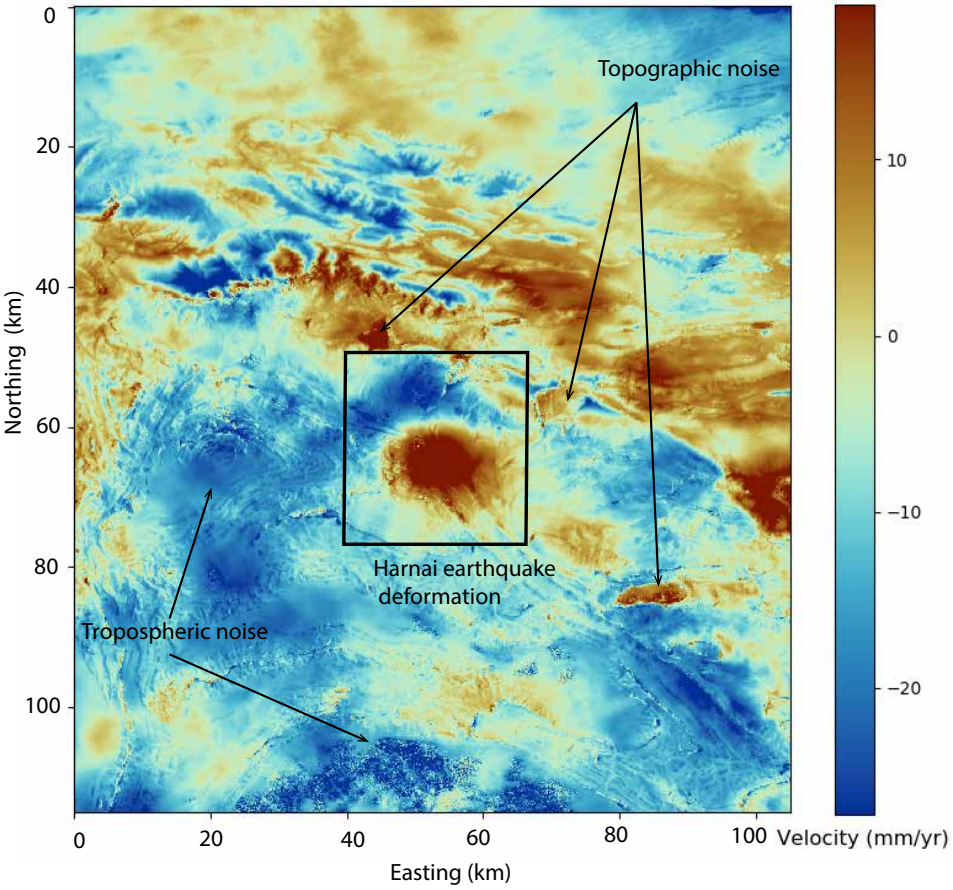

Figure 2.8: The contribution of topographic noise in the velocity inferred from Sentinel-1A time series from 30 October 2020 to 30 November 2021 at the central SFT zone in the descending track T078. The GACOS corrections are already applied to remove the stratified atmospheric noise that correlates with topography. The black rectangle shows the deformation produced by the 2021 Mw 6.0 earthquake at the western SFT zone.

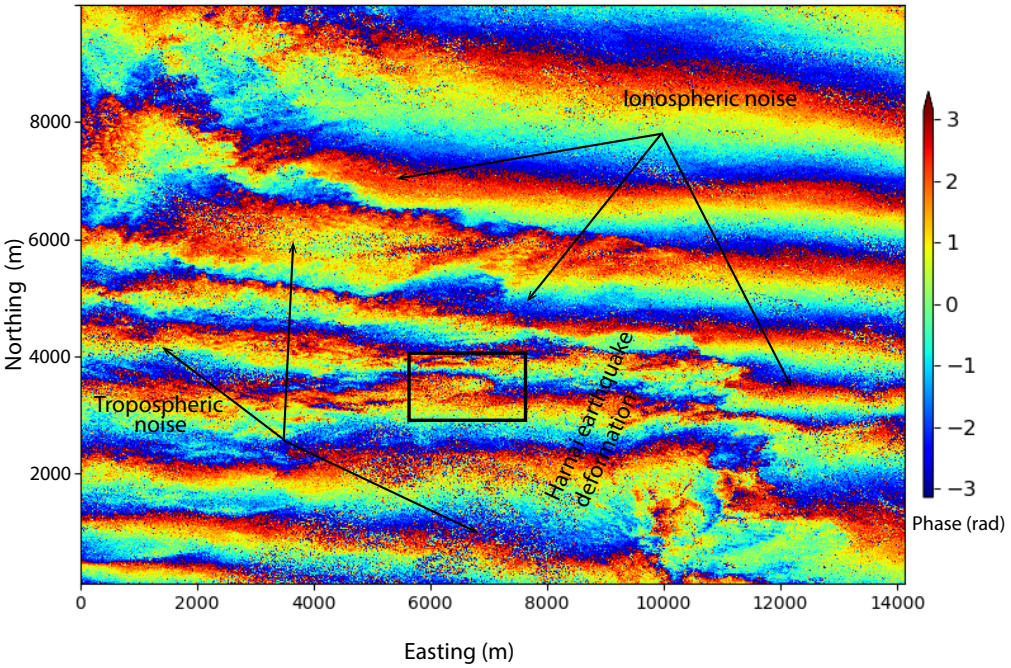

Figure 2.9: The contribution of atmospheric and significant ionospheric noise in an interferogram produced using L-band ALOS-2 ScanSAR data from 29 September 2021 to 10 October 2021 at the western SFT zone. The black rectangle shows the deformation produced by the 2021 Mw 6.0 earthquake at the western SFT zone.

accuracy requirements of the application, and the computational resources available. The example of scattered tropospheric, and ionospheric noise is shown in Figure 2.9.

2.4.1.3 Unwrap Phase Errors

Phase unwrapping is an essential step in InSAR processing to accurately measure surface deformation. Without phase unwrapping, the interferogram would only provide an ambiguous measurement of the terrain altitude, which would make it difficult to identify and measure small elevation changes. Resolving the 2π ambiguity in the interferometric phase during phase unwrapping can introduce an error (Ferretti et al., 2007; Goldstein et al., 1988). This is a challenging step, especially in regions with high topographic gradients, and high noise levels. However, there are several effective phase unwrapping algorithms available to unwrap the phase accurately (Goldstein et al., 1988; B. Wang et al., 2023; Zhou et al., 2020)

2.4.1.4 Other sources of Noise

In an ideal case, one dominating scatterer may be present in each resolution cell, however, we find multiple elementary scatterers in each resolution cell, which could be changed between two SAR observations time intervals. Therefore, the presence of several scatterers varying with time in each resolution cell introduces the phase noise. Temporal variations of scatterers are prominent in areas with crops, vegetation, forests, and water basins, and we can find a significant change in scatterers between the two acquisitions of the two SAR images, whereas buildings in the cities, and exposed rocks remain unchanged for several decades.

The change of scatterers in time produces the phase noise. When we have multiple combinations of elementary backscatterers, the speckle will change even if the scatterers remain unchanged over time due to the critical baseline of the interferometric phase. The critical baseline is determined by the terrain slope, and the interferometric phase above the critical baseline will be considered pure noise. however, it can be removed by designing filters (Ferretti et al., 2007). Once all the significant phase errors have been removed from the interferometric phase, the remaining phase can be used to estimate surface deformation accurately.

2.5 Earthquake Deformation Cycle

In the last several decades, the space geodetic revolution has provided us with the ability to monitor the behavior of fault zones with an accuracy of about 1 mm. The crustal deformation around a major fault zone for a complete earthquake cycle (Figure 2.10) is commonly divided into;

- Coseismic deformation
- Postseismic deformation
- Interseismic deformation

However, interseismic and long postseismic deformation phases are sometimes challenging to separate.

2.5.1 Coseismic Deformation

Coseismic deformation (Figure 2.10, 2.11, and 2.12) that occurs during an earthquake is routinely measured from geodetic observation. The ability of SAR is remarkable to cover all over the globe and record images in the form of phase and amplitude without any instrument being installed on the ground. The phase and amplitude images, before and after an earthquake are further used to compute the interferograms showing the deformation. The InSAR observations can be used to constrain the ruptured fault geometry and then the distribution of slip over the fault of the earthquake (Barbot et al., 2023; Cakir et al., 2023; Javed et al., 2022) (Figure 2.11, and 2.12).

The source fault parameters estimated from space geodesy have several advantages over other traditional models, especially for shallow major earthquakes. The geodetic source fault models provide accurate epicenter locations of earthquakes, surface ruptures, and orientations of the rupture. In addition, the slip distribution of the shallow earthquakes over the ruptured fault plane determined from geodetic observations is more reliable than that determined from seismology (Funning et al., 2014). The fault can be divided into multiple segments based on literature, geological field observation, and SAR interferograms to model the slip distribution (Barbot et al., 2023; Javed et al., 2022). However, there are also some ambiguities in the source fault geometries such as hypocentre location, and dip of the fault determined from SAR interferometry, particularly for moderate to small earthquakes in regions with large atmospheric, and topographic variations. It is challenging to fully remove the atmospheric errors. The example of a coseismic deformation measured from Sentinel-1 ascending and descending interferograms is shown in Figure 3.1b, c.

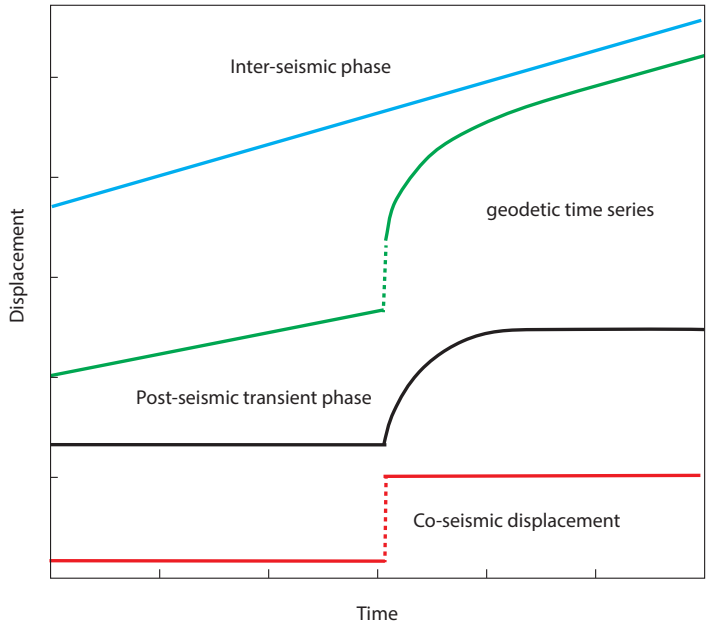

Figure 2.10: . The different stages of a fault behavior during an earthquake cycle. Space geodesy provides great insights to understand the distinct phenomena occurring during interseismic, coseismic, and postseismic phases.

2.5.2 Postseismic Deformation

After a major earthquake, we usually find a phase of transient and postseismic deformation, which arises from the adjustment of the crust and mantle due to stress changes that occur during an earthquake as shown (Figure 2.10, 2.11, and 2.12). The rates of transient deformation for large earthquakes vary with time and space and are determined by the viscoelastic relaxation phenomena. The mechanism of time-dependent postseismic processes is critical to gain insights into the seismic cycle of a fault. We find several mechanical processes involved that could produce the postseismic deformation, such as viscoelastic relaxation of rocks at the deeper zones of the seismogenic layer (Freed and Bürgmann, 2004; Pollitz et al., 2001), aseismic or transient slip within the ruptured zone often at the downdip (Savage and Svarc, 1997), and local poroelastic rebounds caused by fluid flow in the pores during an earthquake (Fialko, 2004a; c; S. Jonsson et al., 2003; Peltzer et al., 1998) (Figure 2.11, and 2.12).

In the early stages, the deformation often occurs near the rupture zone mostly dominated by afterslip both at shallow and deeper depths below the ruptured fault and also multiple forms of poroelastic rebounds. Later, in the far field, we find the deformation induced by viscoelastic relaxation phenomena in the upper mantle and lower crust (Figure 2.11, and 2.12). If the postseismic deformation

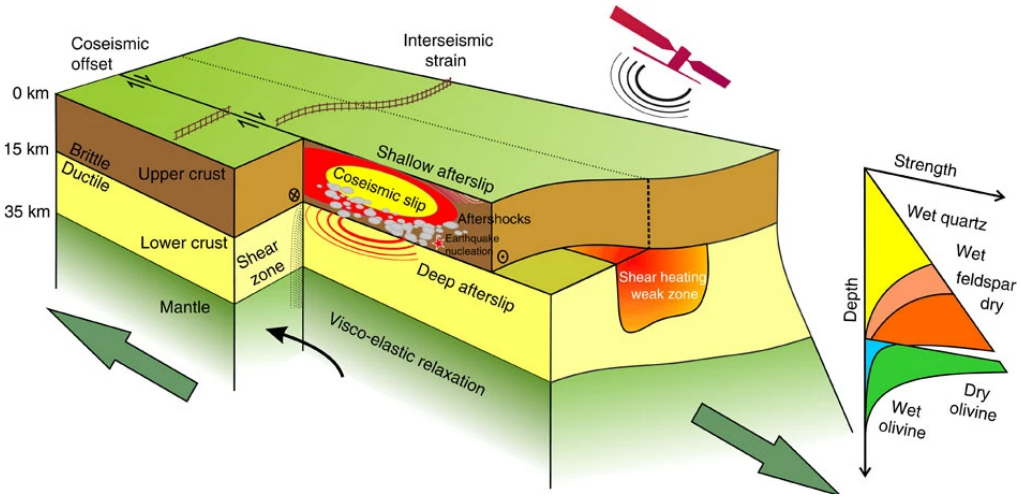

Figure 2.11: Space geodetic revolution helps us to monitor the behavior of faults and measure time-dependent parameters of deformation to insight into the entire earthquake cycle. Coseismic deformation occurs over a fault in the seismogenic crust. Postseismic deformation in the form of shallow and deep after-slip started shortly after an earthquake. The shallow after-slip occurs in the brittle upper crust, and the deep after-slip occurs in the ductile lower crust and upper mantle. Interseismic strain accumulates across the fault zone for the rest of the period of the earthquake cycle. The figure is modified from (Elliott et al., 2016)

phases mentioned above can be distinguished from each other, could provide valuable information about the fault zone hosting earthquakes, and ambient rock features. In addition to the creeping slip rates on a fault during postseismic deformation, frictional properties of the rupture can be inferred during the afterslip, pore fluids and porosity of the rocks during poroelastic phenomena, and rheological properties of the substrate during viscoelastic relaxation phenomena. Furthermore, measuring creep rates prior to an earthquake is equally important, especially for the faults that break in the form of segments and host often major earthquakes.

2.5.3 Interseismic Deformation

Interseismic deformation phase occurs between earthquakes and typically shows a steady motion on either side of the fault as shown in Figure 2.10, 2.11, and 2.12. At this stage, the fault is locked at the upper crust of the seismogenic layer, however, we find the deformation due to movement at the lower crust and upper mantle (Figure 2.11, and 2.12). Such deformation is distinguishable, particularly, in the case of the major strike-slip faults such as the NAF and EAF zones.

The interseismic deformation is mainly focused around the fault zone (Garth-

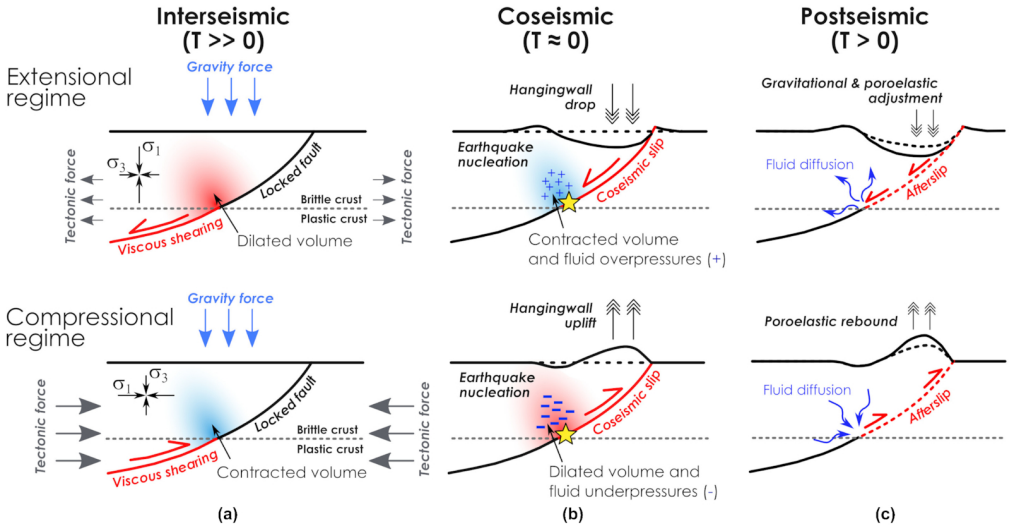

Figure 2.12: A sketch of an entire earthquake cycle including, coseismic ($T = 0$), postseismic ($T > 0$), and interseismic ($T >> 0$) phases in the thrust and extensional regimes. Star indicates the hypocentral location of a presumed earthquake, $T = 0$ represents the time earthquake nucleation. The figure is modified from (Albano et al., 2021)

waite et al., 2013; Walters et al., 2011) (Figure 2.11). Some authors have successfully modeled such deformations assuming the boundaries of tectonic blocks are thin, extending exclusively from the surface to the greater depths. The entire boundary zone, except the locked upper crust of the tectonic blocks, moves at a constant rate (Savage and Burford, 1973; Weertman, 1966) (Figure 2.11, and 2.12). However, we cannot distinguish the distributed shear below the seismogenic depth of around 15 km, typically at the upper mantle on the narrow fault zone using solely InSAR and GPS data (Elliott et al., 2016; Moore et al., 2000). Though, the steady interseismic slip rates estimated from geodetic observations can be compared with the rates derived from geological measurements estimated by geodating techniques of the sites around the fault zones (Meade et al., 2013; Thatcher, 2009). Therefore, short-term geodetic measurements can be very useful to estimate the long-term slip rates of the tectonic blocks.

3 Coseismic Folding at the front of the Sulaiman Fold and Thrust belt

Abstract

The Sulaiman Fold and Thrust (SFT) belt in Central Pakistan formed during the India-Eurasia collision in the late Cenozoic. However, the mechanics of shortening of the brittle crust at time scales of seismic cycles is still poorly understood. Here, we use spaceborne Radar interferometry to analyze the deformation associated with the 2015 moment magnitude (Mw) 5.7 Dajal blind earthquake at the eastern boundary of the SFT. We use kinematic inversions to determine the distribution of slip on the frontal ramp and of flexural slip along active axial surfaces for the forward- and backward-verging two end-member models: a double fault-bend fold system and a fault-propagation fold. In both models, a décollement branches into a shallow ramp at approximately 7.5 km depth with coseismic folding in the hanging wall. The Dajal earthquake ruptured the base of the Boundary Thrust buried under the sediment from the Indus River floodplain, representing fault-bend or fault-propagation folding some 30 km off its nearest surface exposure.

The work has been published in (Javed et al., 2022), here the text and figures are reproduced from the publication.

3.1 Introduction

The kinematics of crustal deformation at fold-and-thrust belts is complicated by the interaction between faulting and folding (Chapple, 1978; Muñoz and Charrier, 1996; Poblet and Lisle, 2011; Price, 1981; Sepehr and Cosgrove, 2004). Complex fault geometry causes shortening in the hanging wall that is accommodated by flexural slip, a type of plastic deformation that results from slip on multiple bedding planes in sedimentary strata (Couples et al., 1998; K. M. Johnson, 2018; K. M. Johnson and A. M. Johnson, 2002; Kaneko et al., 2015; Sathiakumar et al., 2020; Suppe, 1983; Tanner, 1989). Subduction zones exhibit a thrust-and-fold belt in the forearc near the trench (D. Davis et al., 1983; Kopp and Kukowski, 2003; Qiu and Barbot, 2022; Saffer and Bekins, 2002), even in the

poorly developed frontal prism of erosive margins (Eakin et al., 2014; Tsuji et al., 2014; Von Huene et al., 1985). Fold-and-thrust belts can also be found at the margin of collision zones (Hubbard et al., 2016; 2015; Lavé and Avouac, 2000; Yue et al., 2005) and in other transpressive settings (Lai et al., 2006; Namson and T. L. Davis, 1988; Shaw et al., 2004; Shaw and Shearer, 1999; Shaw and Suppe, 1994; 1996; Tapponnier et al., 1990). The role of folding on the long-term build-up of topography is well explained in various tectonic environments (T. L. Davis et al., 1989; Kastelic and Carafa, 2012; Mahanjane and Franke, 2014; Shaw et al., 2005). However, the mechanical coupling between folding and faulting during seismic cycles is still poorly understood. Some observations (Kuo et al., 2014; A. Lin et al., 2001; J. Lin and R. Stein, 1989) and numerical modeling (Sathiakumar et al., 2020) indicate that coseismic folding is possible, but how this deformation occurs in the crust is still poorly resolved.

The relative convergence between the Indian subcontinent and the Afghan block results in underthrusting of the Indian plate (Figure 3.1a). The western margin of the India-Eurasia collision belt, which accommodates around half of 35-46 mm/yr of relative plate motion (Ul-Hadi et al., 2013), provides an ideal setting to study the mechanics of an active fold-and-thrust belt (Figure 3.1a) (Banks and Warburton, 1986). The shear component is accommodated along the transform boundary of the Chaman Fault (CF) system but shortening is taken up by the transpressive Kirthar Fold Thrust (KFT) and the Sulaiman Fold Thrust (SFT) (Bernard et al., 2000; Fattahi and Amelung, 2016; Saif-Ur-Rehman et al., 2020; Szeliga et al., 2012). The deformation front separating Eurasia from the Indian subcontinent in Central Pakistan is the Boundary Thrust (BT), at the eastern limit of the SFT. The SFT belt is seismically active with many devastating earthquakes occurring within a complex network of blind thrusts, fault bends, duplex structures, and strike-slip faults (Banks and Warburton, 1986; Jadoon, 1995; Prevot et al., 1980). The historical earthquakes and fault plane solutions in the SFT belt in the last three decades are shown in Figure 3.1a. The regional seismicity is characterized by thrust and a few strike-slip earthquakes (Pezzo et al., 2014; Reynolds et al., 2015). For example, the doublet thrust of Mw 6.9 events that occurred on February 27, 1997, separated by approximately 19 seconds, caused many fatalities and major economic loss (Nissen et al., 2016). Although the Central and Western SFT are characterized by well-developed fault-bend folding structures, the structures in the eastern SFT zones are under-developed (Banks and Warburton, 1986; Khan and Scarselli, 2021; Saif-Ur-Rehman et al., 2019), experiencing only moderate-size NE-SW and E-W thrust earthquakes, with a deficit of large (Mw>6.0) earthquakes along the BT in the last several decades. Large cities with a population of more than 3 million are located approximately 10 to 50 km from the BT (Figure 3.1a).

On October 23, 2015, a Mw 5.7 earthquake occurred near Dajal, 55 km SSW of

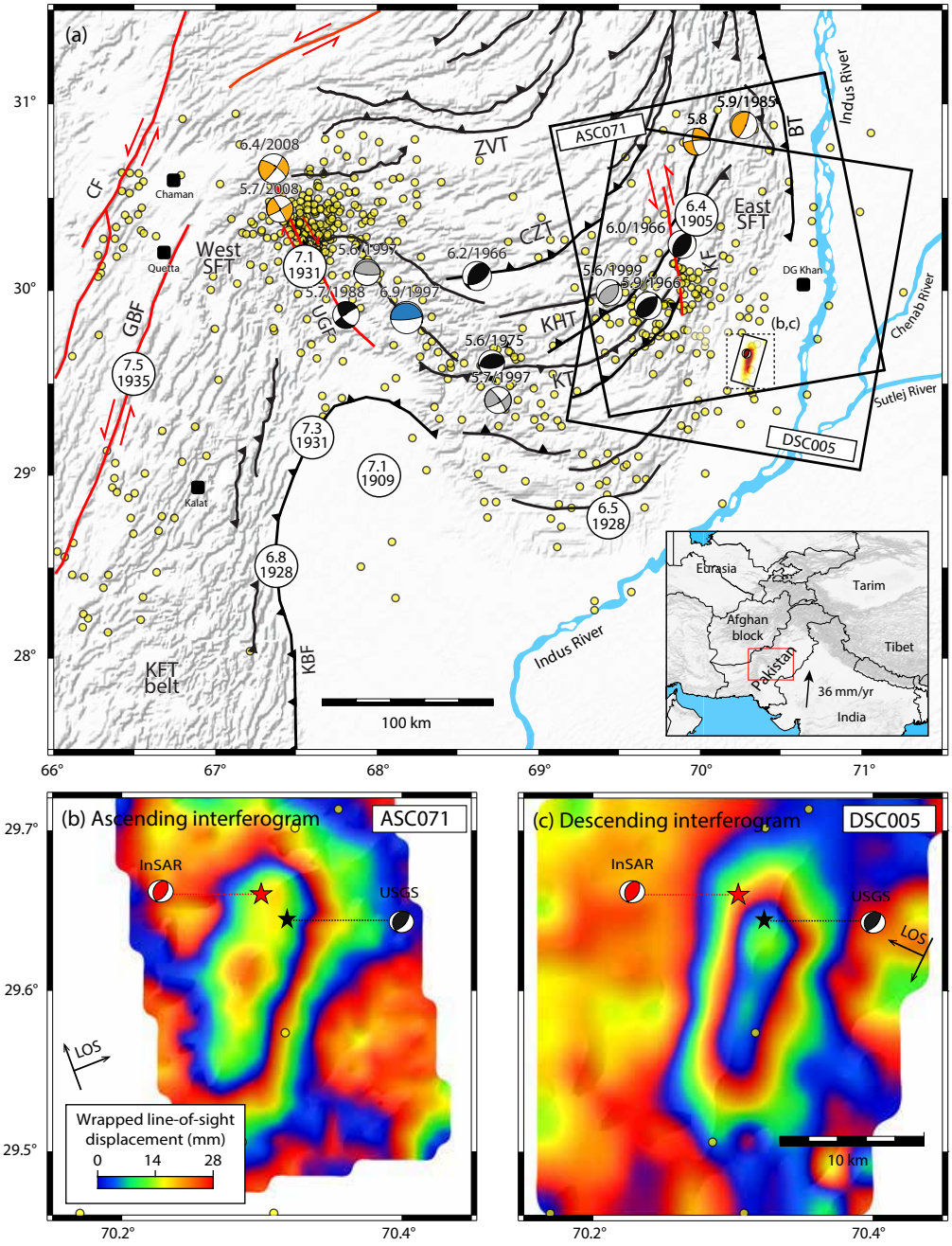

Figure 3.1: Tectonic settings and historical earthquakes (yellow circles) with M>3.5 on SFT belt. a) Faults abbreviated with BT – boundary thrust, CF – Chaman Fault, GBF – Ghazaband Fault, KF – Kingri Fault, KT – Kamari Thrust, KHT – Karahi Thrust (Pezzo et al., 2014). Focal mechanism solutions in blue (Nissen et al., 2016), orange (Pezzo et al., 2014), GCMT catalog, dark gray (Reynolds et al., 2015), black (Bernard et al., 2000), and white circles (Ambraseys and Bilham, 2003). The dark red moment tensor is the 2015 Dajal earthquake epicenter, shown above the slip distribution. The inset shows the geographical location of the SFT belt and the relative motion (36 mm/yr) between the India and the Afghan block (Ul-Hadi et al., 2013). b) and c) Ascending and descending, wrapped LOS displacement of the 2015 Dajal earthquake.

Dera Ghazi Khan, one of the most populated cities of Punjab province, Pakistan (Figure 3.1a). The earthquake occurred at the eastern boundary of the SFT, providing an opportunity to study the interaction of coseismic slip and folding within an active fold-and-thrust belt (Figure 3.1b, c). Here, we investigate the deformation induced by the 2015 Mw 5.7 Dajal earthquake to gain new insights into the mechanics of folding through flexural slip during the seismic cycle. The orientation and maturity of the frontal fold-and-thrust belt is still poorly understood. A preliminary geological interpretation of a controlled-source seismic profile across the BT some 20-30 km north of the epicenter infers the presence of a shallow thrust, dipping eastwards at an angle of 30° to 40°, possibly rooted in a décollement at 5 – 10 km depth forming a double fault-bend fold (FBF) or a fault-propagation fold system (FPF) (Humayon et al., 1991; Saif-Ur-Rehman et al., 2019). The double FBF system is defined by two horizontal décollements separated by a frontal ramp and associated active axial surfaces originating at the fault bends (Suppe, 1983), whereas the FPF system involves a deeper horizontal décollement and the frontal ramp that terminates below a thick sediment layer along with their associated axial surfaces initiated at the fault bends and top of the fold (Sathiakumar et al., 2020; Suppe, 1983; Suppe and Medwedeff, 1990). A more recent interpretation of the controlled-source seismic profiles at the Eastern SFT zone in addition to the other geological and field observations invokes a FBF system with a pair of forward- and backward-verging faults (Humayon et al., 1991; Saif-Ur-Rehman et al., 2019).

3.2 Methods of InSAR Processing and Modeling

3.2.1 InSAR Analysis

We select two pairs of Sentinel-1A observations of ascending track $T-071$ and descending track $T-005$ in TOPS mode that have the shortest perpendicular and temporal baselines with the least seasonal atmospheric variation to retain high correlation. Features of these datasets including orbit number, track, incidence angle, and heading angle of ascending and descending tracks are given in Table 3.1. We generate the ascending and descending interferograms using single look complex (SLC) products through the GMT5SAR code (Sandwell et al., 2011).

We mostly follow the default procedure for processing and filtering. We use the amplitude image and a 1-arc-second SRTM digital elevation model (Farr et al., 2007) for co-registration and to produce the topographic phase correction. We generate the unwrapped interferometric phase for the ascending and descending acquisitions. We improve the co-registration through 1) geometric alignment on the basis of precise orbit (Sansosti et al., 2006), 2) de-ramping of SLC before

Table 3.1: Features of Sentinel-1A interferometric pairs

Image pair (yy/mm/dd)	Track	Perp. baseline (m)	Temp. baseline (days)	Inc. angle (°)	Head. platform (°)
2015/10/17–2015/11/10	*ASC* – *T*071	174	24	36 – 39	−12.59
2015/10/01–2015/11/18	*DSC* – *T*005	40	48	36 – 39	167.35

interpolation of data (Miranda et al., 2015) and 3) mitigation of mis-registration on the basis of the spectral technique (Prats-Iraola et al., 2012). Azimuth co-registration is more difficult in TOPS mode acquisition than conventional strip map (De Zan and Monti Guarnieri, 2006). After high-quality co-registration, we remove the effect of topography from the SAR interferogram. In the first stage, we use a Gaussian filter with a wavelength of 200 m, and in the second a Goldstein filter is applied to the interferograms (Baran et al., 2003; Goldstein and Werner, 1998). We use SNAPHU (C. Chen and Zebker, 2002) software to unwrap the interferogram with a threshold coherence of 0.15. Each subswath of interferometric SAR acquisition is processed individually and independently within its corresponding coordinates. In the end, geocoding is applied to transfer the radar coordinate system to the geographic coordinate system.

With aim to define the data region to consider in the inversion, we have made a simulation of the expected surface deformation signal for a single fault, assuming an average dislocation. We find the signal to be confined to a region of 0.2° × 0.2° and to decay quickly from its central part, with a noise level of about 2 mm. This region limits the square of useful data since at greater distances we cannot expect to have any signal in the data, but just add data with noise or with a signal which has nothing to do with the earthquake. The topography of the deformed region is flat, which is a favorable situation in relation to atmospheric effects since they are correlated with topography. Nonetheless, we have tested also the interferograms on a wider region (0.6° × 0.6°) taking acquisitions before and after the 2015 Dajal earthquake, as shown in Figure 3.2. The figure clearly shows the presence of atmospheric noise to the west of the Dajal earthquake deformation zone (Figure 3.2a - e), although we had applied the GACOS for InSAR (Yu et al., 2018b) and removed atmospheric noise. We find significant noise on the western side of the coseismic deformation zone in the interferograms of 10 November to 17 October 2015 (Figure 3.2a). This noise signal is absent in the descending interferogram from 01 October to 18 November 2015 (Figure 3.2f), which demonstrates that the western signal on

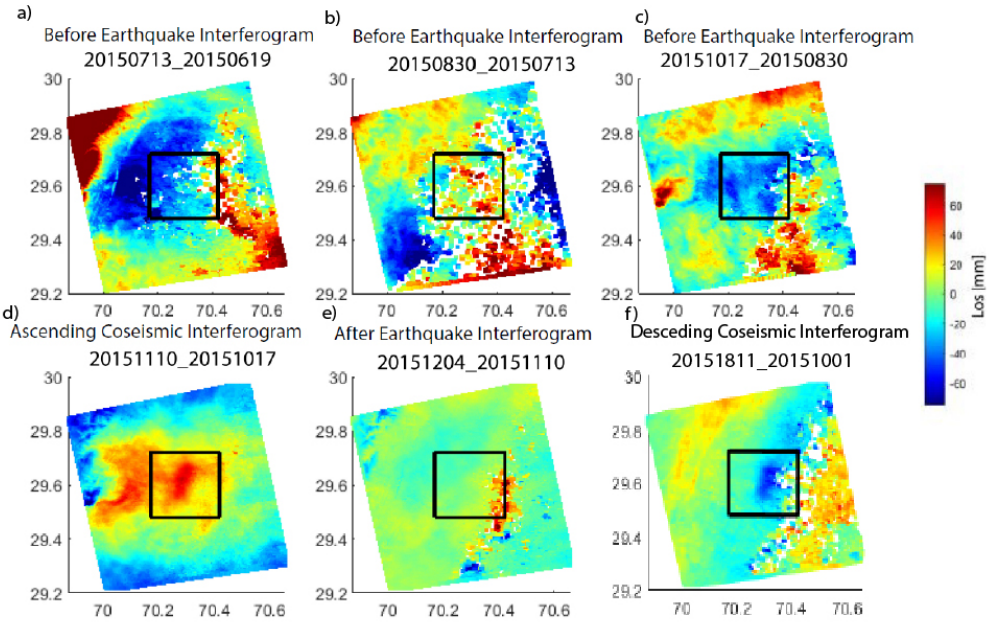

Figure 3.2: LOS displacement for ascending (a-e), and descending (f) tracks, calculated using Sentinel-1A interferograms for time couples before, after, and across the 2015 Dajal earthquake of 23 October 2015.

LOS on the ascending interferogram is due to noise. Moreover, the noise is lower in the ascending track for the 10 November to 04 December 2015 interferogram (Figure 3.2e). This shows that the noise is probably due to local strong rains that affect the area in fall and is stronger where the topography rises steeply, which is to the western side of the deformation zone. We can clearly observe the region outside 0.2° x 0.2° area is noisy and can reach up to 15 - 20 cm. The inclusion of this wider area has a significant impact on the results, as the noise level is higher than the signal at those distances.

3.2.2 Error Estimation

Variance and covariance of the datasets are generally estimated experimentally to characterize the InSAR data errors that have occurred due to phase decorrelation. The InSAR errors arise mainly due to varying ionosphere and water vapor content in the upper atmosphere and lower atmosphere respectively (Hanssen et al., 1999). The error can also be encountered due to steep topographic variations at the site and anisotropic spatial variability. We estimate the spatial variability of both ascending and descending interferograms using a semi-variogram (Wackernagel, 2003) by measuring the dissimilarity. We use the unbounded exponential function to compute dissimilarities with nugget, sill, and range variances for the ascending and descending interferograms sep-

arately in Table 3.2. Subsampled points used for Bayesian inversion for both interferograms are shown in Figure 3.3b, d respectively.

Table 3.2: Detail of interferogram errors calculated using semi-variogram

Track	Sill $(mm)^2$	Nugget $(mm)^2$	Range (km)	Threshold $(mm)^2$	Subsample (points)
$ASC - T071$	0.12	1.4×10^{-4}	9.75	1.0×10^{-2}	238
$DSC - T005$	0.038	2.3×10^{-3}	12.07	4.5×10^{-2}	178

3.2.3 InSAR Modeling

We apply the Geodetic Bayesian Inversion (GBIS) approach (Bagnardi and Hooper, 2018) to the ascending and descending space-borne SAR interferograms covering the 2015 Dajal earthquake (Table 3.1). After estimating the experimental semivariogram by masking out the deformation zone, we use full-resolution InSAR data and then subsample both ascending (number of subsamples: 238) and descending (number of subsamples: 178) interferograms based on an adaptive quadtree gradient-based algorithm (P. Jonsson and Eklundh, 2002; Simons et al., 2002) using a threshold variance as given in Table 3.2. The large dataset is commonly subsampled in the Bayesian inversion to reduce the large computation time, and achieve enough information for a successful inversion (Bagnardi and Hooper, 2018). We prefer the gradient-based algorithm because the density of the samples is directly proportional to the displacement gradient and it recursively divides the LOS displacement into further four polygons each time, unless it achieves the selected threshold variance for ascending $(1.0 \times 10^{-2} mm^2)$ and descending $(4.5 \times 10^{-2} mm^2)$ interferograms (Figure 3.3a, c).

We generate a kinematic synthetic model for a uniform rectangular dislocation source (Okada, 1992). The ascending and descending interferograms show the surface deformation of approximately 45 and 50 mm along their respective LOS direction (Figure 3.6a, b). Synthetic models (Figure 3.6c, d) with a single fault patch agree well with InSAR observed data, with average residuals of the order of average 2.3 mm for both interferograms (Figure 3.6e, f). We efficiently categorize the posterior probability density (PDF) of the ruptured fault geometry of the 2015 Dajal earthquake with automatic step size using the Metropolis-Hastings algorithm and the Monte Carlo Markov chain method (Fukuda and K. M. Johnson, 2008; Hastings, 1970; Metropolis et al., 1953; Tarantola, 2005; H. Wang et al., 2017). We use 10^6 iterations to define posterior PDF, discarding the first 20,000 samples. We have used the epicentral location from seismic waveform modeling retrieved from the US Geological Survey (USGS, 2020),

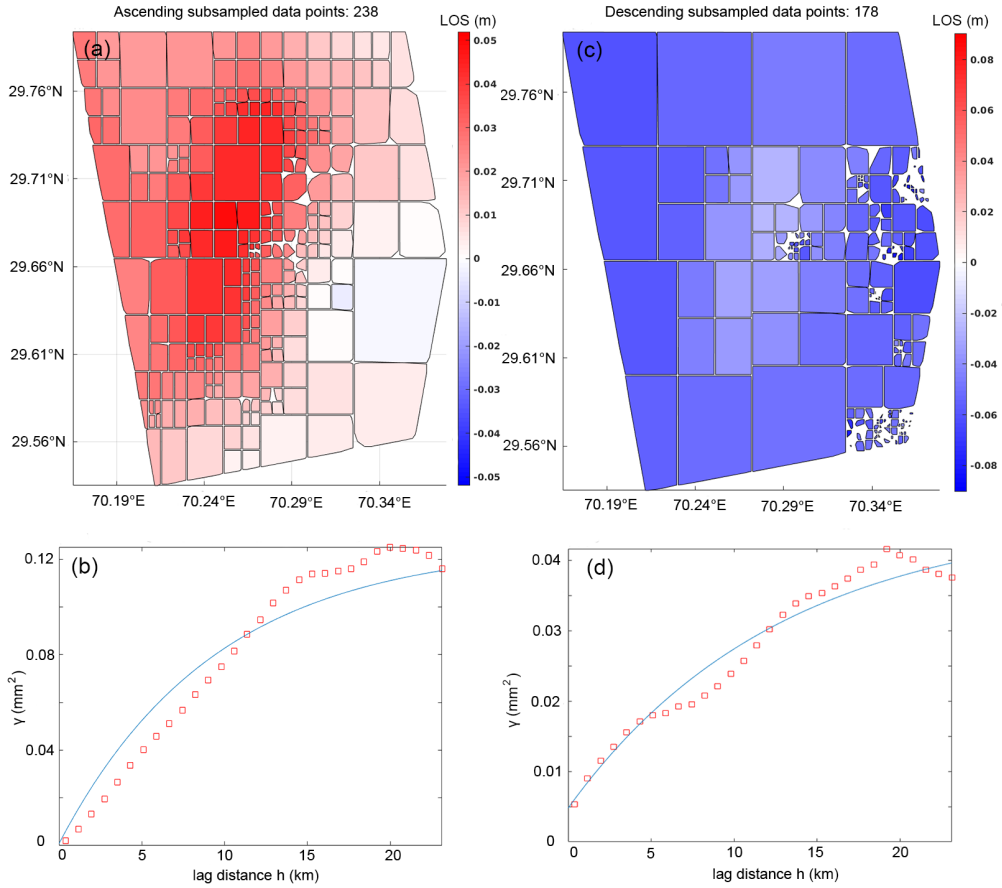

Figure 3.3: The adaptive quadtree gradient-based subsampling and semi-variogram analysis. a, b) The subsampling and semi-variogram to estimate the covariance of the processed interferogram during ascending track respectively. The ascending interferogram is subdivided into 238 points with the threshold variance of 1.0×10^{-2} mm^2. c, d) The subsampling and semi-variogram to estimate the covariance of the processed interferogram during descending track respectively. The descending interferogram is subdivided into 178 points with the threshold variance of 4.5×10^{-2} mm^2. Blue (solid lines) is the exponential function of the semivariogram while Red (blocks) is the experimental semivariogram. The local origin for both interferograms is 70.289°E and 29.662°N.

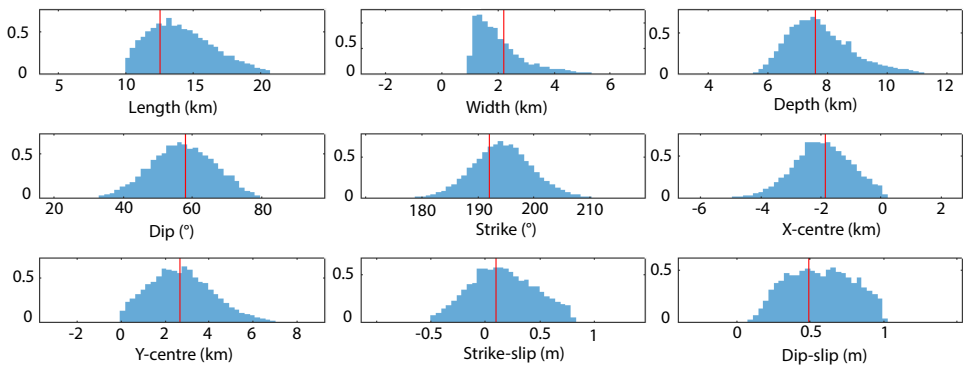

Figure 3.4: Histograms of source fault model parameters through Bayesian inversion approach with 10^6 samples, on wider area of 0.6° x 0.6°. The y-axis represents the probability density, and the red line indicates the optimal model values with 95% confidence interval for GACOS corrected data. (Rejected solution).

and ISC (International Seismological Centre) (Lentas et al., 2019) database as prior information. The inversion is also done on the wider area of 0.6° × 0.6°, which extends beyond the central earthquake deformation zone (Figure 3.2). The wider area is significantly affected by the atmospheric noise accentuated westwards of the epicenter. The noise in the wider area propagates into a greater uncertainty level and misfit in the results, for which reason this solution is discarded (Figure 3.4). The posterior distribution of the final ruptured fault geometry is shown in Figure 3.5. The observation, synthetic, and residual of the final rupture models for the ascending and descending tracks are shown in Figure 3.6 The fault geometry with the 95% confidence interval is given by fault dip (40° ± 12), strike (194° ± 6), length (14.7 km ±2.8), width (2.9 km ±1.2), and depth (6.5 km ±1.2) (Table 3.3). We use 10^6 iterations to define posterior PDF, discarding the first 20,000 samples. We have also used the epicentral location from seismic waveform modeling retrieved from the USGS NEIC database as prior information.

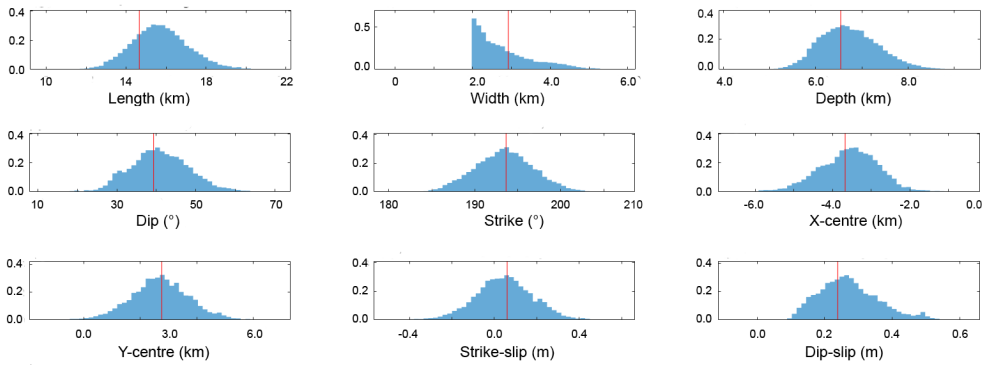

Figure 3.5: Histograms of source fault model parameters through Bayesian inversion approach with 10^6 samples, on area of 0.2° x 0.2°. The y-axis represents the probability density, and the red line indicates the optimal model values with 95% confidence interval. The optimal model has fault length around 15 km, width 2.9 km, depth 6.5 km, dip 40°, strike 194°, and average slip 0.28 m. (Best solution).

Table 3.3: The estimated source fault parameters, inverting both ascending and descending interferograms along with their uncertainties by assuming single fault plane and ignoring fault-bends

Model	Lon (°)	Lat (°)	Str (°)	Dip (°)	Rake (°)	L (km)	W (km)	Dep (km)	Slip (m)	Mo ($10^{17} Nm$)	Mw
USGS	70.326	29.638	194	30	70	-	-	15.5	-	3.096	5.59
	-	-	182	47	68	-	-	11.0	-	1.792	5.44
GCMT	-	-	186	41	56	-	-	12.0	-	3.471	5.63
ISC	70.353	29.618	192	46	45	-	-	19.8	-	-	5.5
InSAR	70.28± 0.03	29.66± 0.02	194± 6	40± 12	79± 10	14.7± 2.8	2.9± 1.2	6.5± 1.2	0.28± 0.14	3.94 ± 4.0	5.66± 0.30

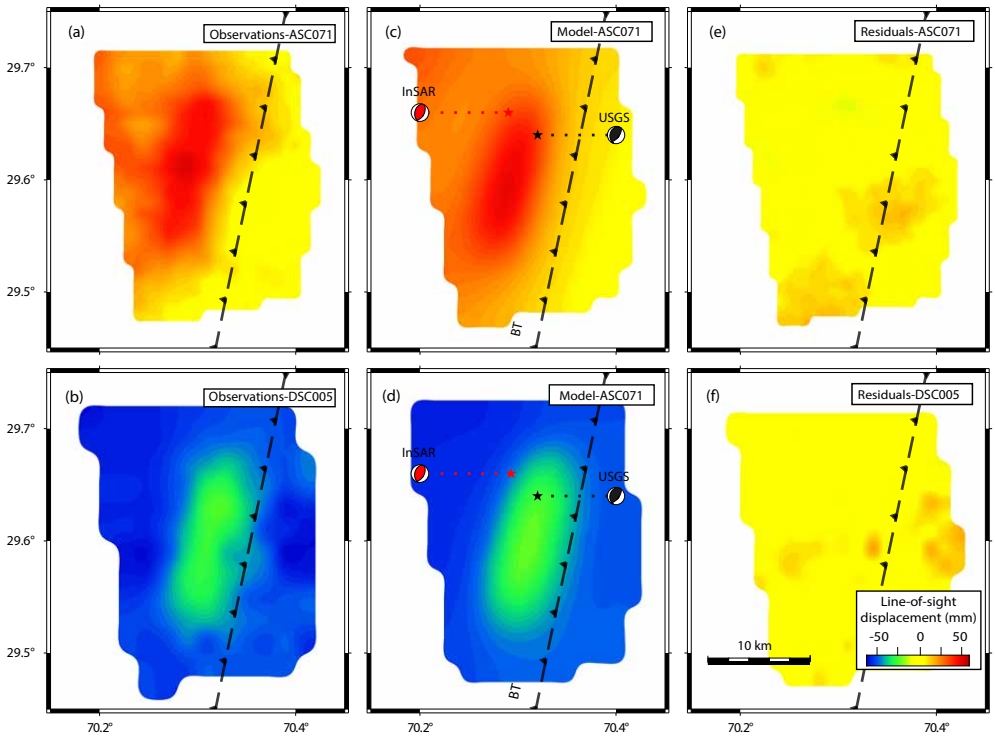

Figure 3.6: Single fault plane solution by using GBIS approach a, b) observation, c, d) synthetic interferogram and e, f) residual of the ascending track (T071) and descending track (T005) respectively. The deformation along the LOS displacement is approximately 50 mm and 45 mm along with less than 2.3 mm residual for descending and ascending track respectively. The focal mechanism solution (red colored) is produced by using inverted ruptured fault parameters and the focal mechanism solution (black colored) is taken from USGS.

3.3 Kinematic Inversions and Folding

Considering the uncertainties in fault orientation, we present kinematic inversions of InSAR for two end-member models of coseismic folding that imply different stages of development of the frontal section: a double synclinal and anticlinal FBF system (Suppe, 1983) and a FPF system (Suppe and Medwedeff, 1990) (Figure 3.7). In addition, we consider either a forward-vergent (dipping westward), or a backward-vergent (dipping eastward) thrust. We take folding in the hanging wall into account explicitly by inverting for the spatial distribution of flexural slip along the active axial surfaces. In the FBF model with a backward-vergent thrust, considerable movement occurs on the west-dipping axial surfaces, which is physically implausible (Figure 3.8c). In the forward-vergent cases, flexural slip accumulates above the hinge of the ramp-décollement system (Figure 3.8a, b), with an amplitude compatible with predictions from balanced cross-sections for long-term deformation (Sathiakumar et al., 2020). Our observations show that folding occurred either during the earthquake rupture or during the short post-seismic phase that followed, which is also captured by the InSAR data. The 2015 Mw 5.7 Dajal earthquake was presumably confined within the blind ramp of the FPF or of the FBF system representing the frontal extension of the BT, where it is buried under the Miocene or younger sediment of the Indus River floodplain. These observations document the seismic potential of blind ramps and axial surfaces in fold-and-thrust belts and the control on final rupture size by fault-bends and surrounding folds.

In FBF and FPF models, the geometry of the active axial surfaces is obtained assuming the conservation of layer thickness, length, and cross-sectional area of the incoming sediment in a balanced cross-section (Suppe, 1983; Suppe and Medwedeff, 1990). Assuming no cut-off angle between the incoming thrust sheet and the basal décollement for the FBF model (Figure 3.7a), the axial surface must bisect the décollement-ramp system, resulting in an angle of 70° clockwise for the deeper décollement, and 110° anti-clockwise for the shallower décollement (Figure 3.7b). For the FPF (Figure 3.7c), the axial surface 1 bisects the ramp-décollement with 70°, the axial surfaces 3 and 4 bisect the wedge above the top of the fold at 55° and 70°, respectively, whereas axial surface 2 bisects the frontal fold with 55° (Figure 3.7d). We consider V_1, V_3, the long-term slip-rate above and below the fault (dark line), and V_2 is the long-term slip-rate along the active axial surface (Figure 3.7a,b). The angle between V_1 and V_3 is 40°, V_1 and V_2 is 70° forms the closed hodograph shown as an inset in the (Figure 3.7b). The hodograph of the axial surface 2 is the same, but with a reversed sense of slip rates (Sathiakumar et al., 2020). The motion along the two top-fold axial surfaces 3, and 4 is explained by the closed hodographs (Figure 3.7d). V_2 is the long-term motion of the rocks in wedge above the two top-fold axial surfaces

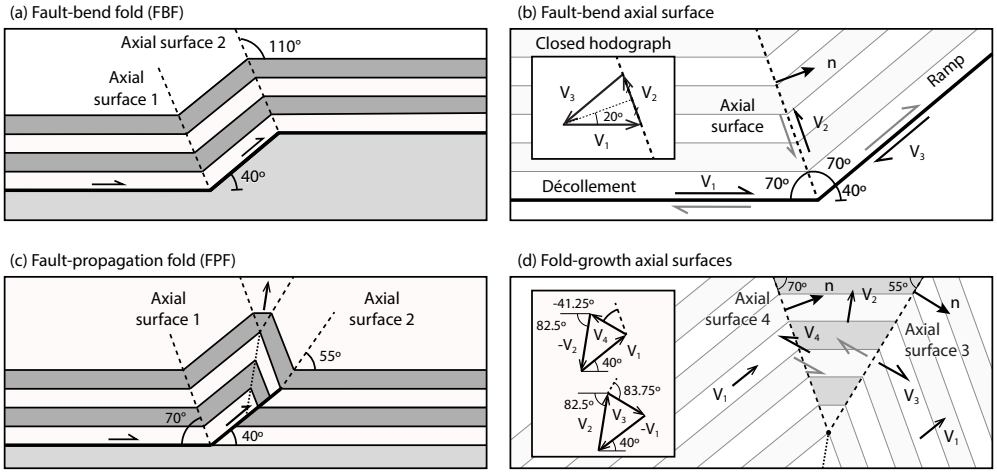

Figure 3.7: End-member models of fault-related folds in a representative cross-section. a) Double FBF model with syncline and anticlinal fault bends and active axial surfaces. b) Long-term slip directions along the décollement, ramp, and axial surfaces. The three velocity vectors close the hodograph (inset). Flexural slip on axial surfaces accommodates the advection of thrusted sediments as they start or stop climbing the ramp. The unit vector **n** is normal to the axial surface. c) FPF with four active axial surfaces (long dashed lines). The domains surrounded by active axial surface move at the same long-term velocity. The passive axial surface (short dashed line) does not contribute to internal deformation. d) Relative motion along the top axial surfaces 3 and 4 of the fault-propagation fault model closing the hodographs (inset). The end-member models are extruded along a 194° strike to form a three-dimensional structure for the purpose of inversion.

parallel to the passive axial surface – connects the dipping ramp and the two top-fold axial surfaces – at an angle of 82.5° from the horizontal. V_4 is -41.25° from the axial surface 4, and V_3 = 83.5° from axial surface 3 forms the two closed hodographs at axial surface 4, 3 respectively (Figure 3.7d). We also consider alternative models with the conjugate dip direction for the ramp with a similar structure but the opposite sense of motion.

3.4 Kinematic Inversion of Coseismic Slip and Folding

The 2015 Mw 5.7 Dajal earthquake occurred in a remote location, outside of any ground-based geodetic observatory. Fortunately, the deformation was captured by the spaceborne SAR Sentinel-1A. To document the surface deformation induced by the earthquake, we generate the Sentinel-1A ascending (ASC071) and descending (DSC005) interferograms (Figure 3.1b, c), allowing us to constrain two directions of deformation. The ascending radar images were acquired

on October 17th and November 10th; the descending images on October 1st and November 18th, 2015, capturing 18 and 26 days of potential postseismic deformation in addition to the coseismic deformation. The seismic moment $M_0 = 3.94 \times 10^{17}$ N m, assuming a shear modulus of 32 GPa, is calculated using the mean value of the probability distribution of the source model parameters, corresponding to Mw 5.7. The epicentral location and source properties are similar to inferences from the U.S. Geological Survey (USGS) (USGS, 2020), and the ISC (Lentas et al., 2019) (Table 3.3). The depth of 6.5 ± 1.2 km is similar to past events in the Eastern SFT region (Reynolds et al., 2015). This simple model indicates that the rupture took place on a 40 ± 12°-dipping thrust with strike 194 ± 6°, located east of the exposed SFT, buried deep below the Miocene or younger sediment of the Indus River floodplain. We use this result to construct a three-dimensional model of coseismic deformation compatible with the fold-and-thrust tectonic setting.

Based on the fold-and-thrust tectonic environment, we investigate forward- and backward-vergent thrusts for two relevant end-members of fault-bend geometries of crustal deformation that involve fault slip at the base of the thrust sheet and folding in the overlying sedimentary strata. In all cases, we surmise that a blind extension of the BT extends towards the Dajal earthquake epicentral area. In the FBF model, we consider slip on the décollement-ramp-décollement, and flexural slip along two active axial surfaces initiated at the fault-bends (Figure 3.7a). For the FPF, the model includes slip on the décollement-ramp system and flexural slip on the four active axial surfaces: one aligned with the hinge of the fault bend, two at the top of the fold, and one at the tip of the ramp (Figure 3.7c). In simple models of folding, flexural slip accommodates the advection of thrusted sediments through the active axial surface as they start or stop climbing the ramp. This localized plastic deformation can be represented by dislocation theory, whereby the nucleus of strain is defined by the unit normal vector **n** of the axial surface and the direction of long-term motion (Sathiakumar et al., 2020). Even though faults and active axial surfaces are drastically different objects, their short-term effect on displacement and stress in the surrounding elastic medium can be represented by double-couple moment tensors and elastic solutions. The direction of long-term motion along an axial surface is the difference between the long-term velocity vectors in the domains that it separates (Daout et al., 2016a; b; Sathiakumar et al., 2020) (Figure 3.7b, d). Assuming no cut-off angle of incoming sediment implies the same slip-rate on the ramp and on the décollement, although with different vector directions. The absolute value of long-term slip rate is not required to determine the direction of long-term relative motion along axial surfaces. The geometry of the active axial surfaces is obtained assuming the conservation of layer thickness, length, and cross-sectional area of the incoming sediment in a

balanced cross-section (Suppe, 1983; Suppe and Medwedeff, 1990). If folding is entirely coseismic with 40° fault-bends, flexural slip should amount to a fraction of the coseismic slip equal to $2\sin(20°) = 0.68$, corresponding to the closure of the hodograph formed by the relative velocity vectors on the décollement, ramp, and axial surface for both forward and backward-vergent models (Figure 3.7).

We consider the fault-related fold geometries laid out in Figure 3.7 and the full resolution InSAR observations to estimate the deformation models and corresponding residuals for the forward- and backward-vergent thrusts (Figure 3.9a-r). We model surface deformation due to slip on the ramp and the décollement using analytic solutions (Okada, 1985). For the forward- and backward-vergent FBF models, we determine the distribution of slip on the ramp, two décollements, and the flexural slip over the two axial surfaces through a non-negative least-squares inversion where motion is aligned with the direction of long-term motion (Barbot et al., 2013; Jónsson et al., 2002). We discretize the model into square patches of 800 m length allowing non-zero along-strike and down-dip slip. We use a L-curve (Aster et al., 2012; Parker, 1994) to resolve the trade-off between misfit and roughness (Figure 3.10c). The coseismic rupture is much elongated, almost entirely confined to the ramp, with along-strike rupture propagation from north to south, parallel to the BT. Virtually no slip takes place on the shallower or deeper décollements (Figure 3.8a). The model produces up to 24 cm of flexural slip along the deeper axial surface 1, concentrated near the nucleation area to the north. There is virtually no flexural slip on the shallow axial surface (axial surface 2). There are notable differences for the backward-vergent FBF, which showcases more flexural slip on the axial surfaces than fault slip in the immediate neighborhood of the ramp (Figure 3.8c).

We now consider the FPF with either a forward- or backward-vergent thrust (Figure 3.8b, d), modeled as a ramp-décollement system with four active axial surfaces. We resolve the spatial distribution of fault and flexural slip using the same approach as above. Both FPF models reveal around 20 cm of flexural slip on axial surface 1, but virtually no flexural slip on surfaces 2, 3, and 4 (Figure 3.8b, d). In the forward-vergent FBF and FPF, the flexural slip follows the pattern of coseismic slip on the ramp. For the backward-vergent models, flexural slip only occurs near the up-dip tip of the ramp rupture, and coseismic slip is mostly confined on the frontal ramp, with the maximum slip of 50 and 45 cm found at 7.0 km depth respectively (Figure 3.8b, d). The potency density — the average change of strain around the earthquake, i.e., the stress drop divided by the rigidity of the country rocks — is 44 micro-strain, comparable with that of the 2013 Mw 7.7 Balochistan, Pakistan earthquake, which had a similar centroid depth, and consistent with the general trend of potency density of thrust earthquakes worldwide (Nanjundiah et al., 2020).

We explore the orientation of the ramp with dip of 30°, 40°, and 50° for all

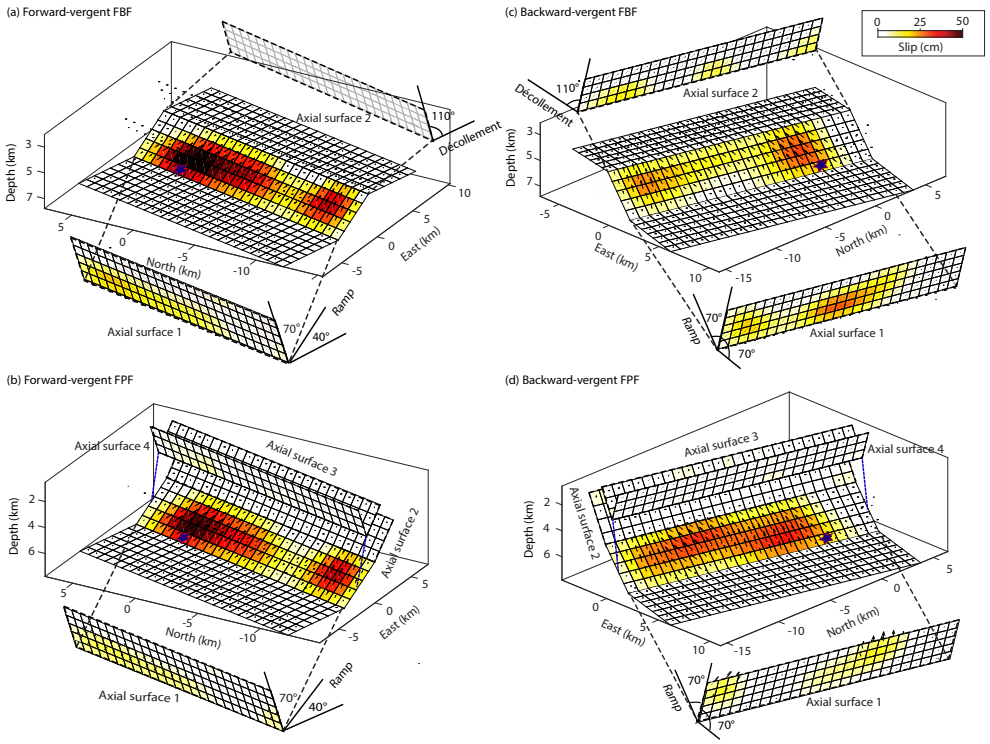

Figure 3.8: Kinematic models of the Mw 5.7 Dajal earthquake for two-end member fault-related fold geometries and two vergence directions. a, c) Forward- and backward-vergent FBF coseismic slip distribution on the décollement-ramp-décollement system and flexural slip on two axial surfaces. b, d) Forward- and backward-vergent FPF coseismic slip distribution on the décollement-ramp system and flexural slip on four active axial surfaces.

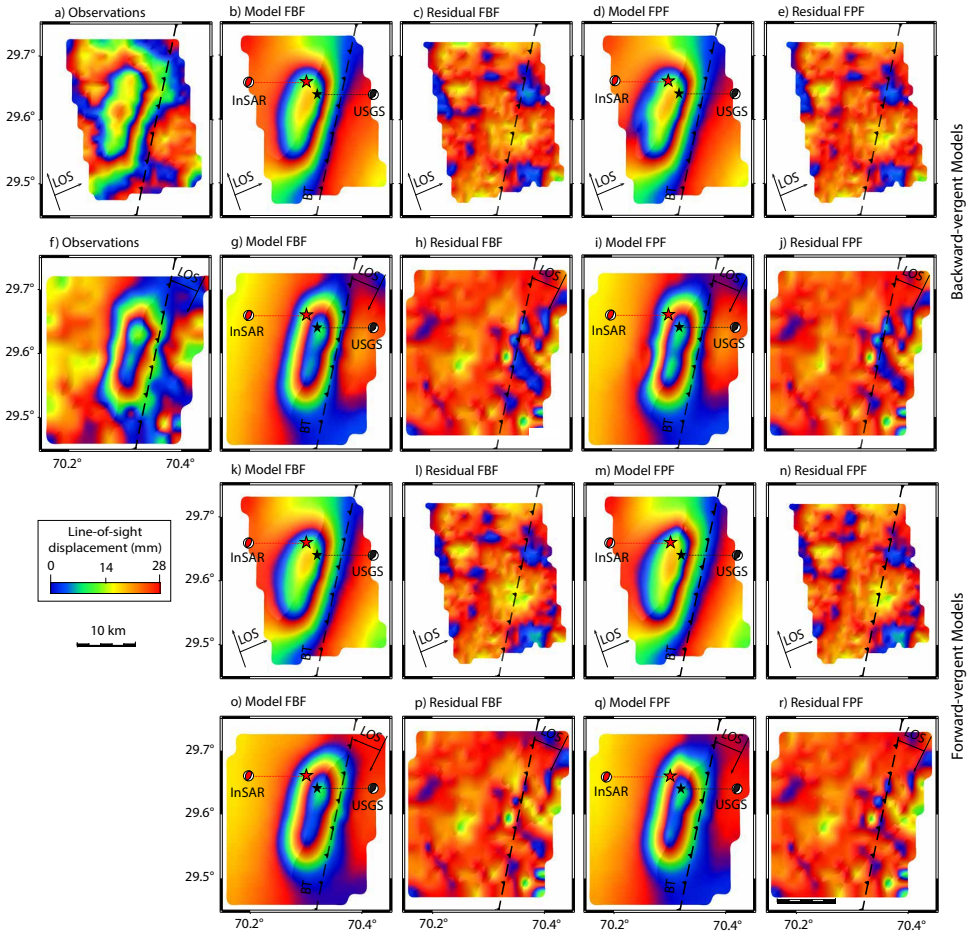

Figure 3.9: The FBF, and FPF model solutions a, f) ascending and descending InSAR observations, b - i) Ascending and descending backward-vergent fault-bend fold and fault-propagation fold models and residuals, k - r) Ascending and descending forward-vergent fault-bend fold and fault-propagation fold models and residuals. The maximum coseismic slip along the LOS displacement is approximately 50 mm along with less than 2.8 mm residual for descending and ascending track respectively. Focal mechanism solution (red colored) is produced by using inverted ruptured fault parameters and focal mechanism solution (black colored) is taken from USGS.

models. The misfit of 40° dip is favored by the data with the lowest RMS for the forward-vergent models (Table 3.4). In all cases, the ramp is where most of the blind rupture took place, compatible with our preliminary investigation. In addition, we perform the Akaike Information Criterion (AIC) (Akaike, 1985; Barkat et al., 2022), and reduced-chi-square analyses (Hubbard et al., 2015; Tsang et al., 2016) to evaluate the preferred models (Table 3.5). The forward-vergent FPF model shows the lowest RMS, AIC, and reduced-chi-square values with a 40° dipping ramp. We also investigate the depth of the deeper décollment at 6.5, 7.5, 8.5 and 9.5 km (Table 3.6). The least systematic residuals correspond to a 7.5 km décollement depth.

The forward-vergent FBF and FPF models (Figure 3.10a, b) explain the observations well, with residuals less than 2.8 mm, and 2.59 mm (Figure 3.10), (Table 3.5). The reduced-chi-square for the forward-vergent FBF and FPF models is 0.82 and 0.72, respectively, even slightly lower for backward-vergent models, with 0.79 and 0.72 (Figure 3.10c), respectively. However, the forward-vergent models exhibit more internal consistency than the backward-vergent ones. In the backward-vergent FBF case, there is more flexural slip on the axial surface than fault slip on the ramp at the same along-strike distance, incompatible with fault-related fold kinematics. In the FPF case, the distribution of flexural slip on the deep axial surface is discontinous. In contrast, the forward-vergent models exhibit features compatible with FBF and FPF kinematics with a distribution of flexural slip on the deep axial surface following the distribution of slip on the ramp and the amount of flexural slip representing 70% of the expected value for coseismic folding. The remaining fraction may occur later in the postseismic period, when folding propagates up-dip of the axial surface through the entire sedimentary stack (Sathiakumar et al., 2020). The 2015 Mw 5.7 Dajal earthquake likely represents the rupture of the frontal section of the BT at the easternmost boundary of the SFT. The rupture can be understood as the seismic activity of the blind, forward-vergent ramp of a FBF or FPF.

Table 3.4: The FPF and FBF models with varying dips at 7.5 km depth and their corresponding residuals. The 40° dip results consistently with the lowest RMS residuals.

Dip (°)	Forward-vergen FPF (mm)	Forward-vergent FBF (mm)	Backward-vergent FPF (mm)	Backward-vergent FBF (mm)
30	3.06	2.91	3.27	2.90
40	2.59	2.80	2.72	2.86
50	3.06	2.76	2.80	2.92

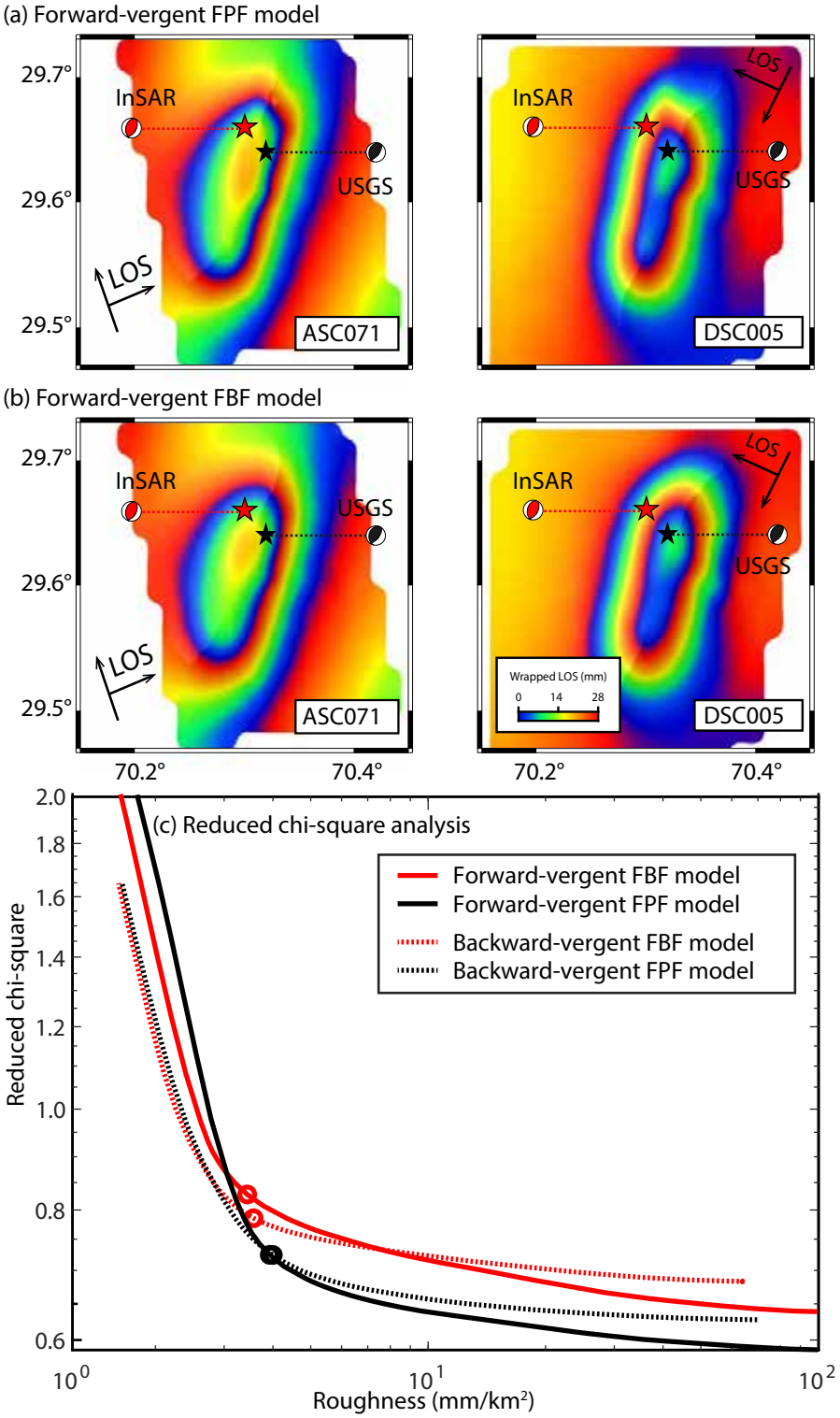

Figure 3.10: Model comparison. a) Forward-vergent FPF models for ascending and descending InSAR tracks. b) Forward-vergent FBF models during ascending and descending InSAR tracks. Focal mechanisms based on InSAR (red) or from USGS (black). c) Tradeoff between data misfit and model roughness (L-curve) for forward- and backward-vergent FBF and FPF models. The black and red color circles show selected smoothing factors for the FBF and FPF models, 0.06, and 0.05, respectively.

Table 3.5: AIC, RMS and Reduced-Chi-square analysis for forward- and backward-vergent models, depth = 7.5 km, dip = 40°. The reduced-chi-square statistic is a measure of the squared difference between the observed and modeled values, considering the degrees of freedom, and the sample size

Models	N	Np	RSS (mm^2)	RMS (mm)	AIC	Reduced Chi Square
Forward-vergent FPF	17331	675	0.1246	2.59	2707.64	0.720
Forward-vergent FBF	17331	675	0.1401	2.80	2708.52	0.820
Backward-vergent FPF	17331	675	0.1285	2.72	2708.04	0.725
Backward-vergent FBF	17331	675	0.1429	2.86	2708.88	0.792

FBF: Fault Bend Fold
FPF: Fault Propagation Fold
N: InSAR data points
Np: Model parameters
RSS: Residual sum of square
RMS: Root mean square
AIC: Akaike Information Criterion

Table 3.6: AIC, RMS for forward- vergent FPF model with dip = 40°with, and varying depth.

Depth (km)	N	Np	RSS (mm^2)	RMS (mm)	AIC
6.0	17331	675	0.2009	3.40	2712.57
7.5	17331	675	0.1227	2.59	2707.64
9.0	17331	750	0.1095	2.51	3006.92
10.5	17331	900	0.1022	2.42	3606.59

3.5 Discussion

The SFT represents a complex duplex structure with multiple faults and folds that increase in maturity westwards towards the interior of the belt (Khan and Scarselli, 2021; Saif-Ur-Rehman et al., 2019; 2020). North of the Dajal earthquake,

where the BT is exposed, the SFT features the Zindapir anticlinorium, characterized by bare Paleocene sediment surrounded by Miocene and younger sediments. The nearby Sakhi Sarwar anticline (Humayon et al., 1991; Saif-Ur-Rehman et al., 2020) shows the development of a fault-bend structure that is less developed and exposes only Miocene and younger sediments. Following this latitudinal progression, we suggest that the Dajal earthquake occurred on the underlying ramp of an even less developed anticlinal structure formed by FPF or FBF buried under the Miocene and younger sediments of the Indus River floodplain (Figure 3.11). Our interpretation is substantiated by nearby seismic reflection profiles (Humayon et al., 1991; Jadoon, 1995; Saif-Ur-Rehman et al., 2019; 2020) that suggest the presence of a shallow east- and west-dipping décollement at a depth of 7 to 9 km for fault-related fold structures. The basal décollement and forward-vergent blind ramp may constitute the eastern termination of the SFT, extending the BT farther south and east. The prolongation of the BT is compatible with the overall strike and longitude of the Dajal earthquake ramp. The buried BT may thrust the same sequence of Cretaceous-to-recent sediments that is ubiquitous elsewhere in the SFT. If shortening continues, the fault-related fold will eventually be exposed, as at the Sakhi-Sarwar anticline farther north. It is possible that other thrusts may be found to the west, forming an imbricate structure that can host other earthquakes.

The 2015 Dajal earthquake illuminates the structural control of seismic ruptures and the relationship between faulting and folding at time scales of the seismic cycle. The large aspect ratio (length/width=6) of the rupture is presumably caused by the termination of the ramp below folded sediments, forcing the rupture to propagate primarily along-strike. If not for the termination of the fault below a synclinal fold, the rupture may have propagated up-dip, producing a larger earthquake with surface breaks. Instead, the rupture concentrates at the base of the ramp, which often constitutes a region of rapid stress accumulation (Sathiakumar and Barbot, 2021). The crustal deformation indicates an apparent synchronicity between coseismic slip and folding of the hanging wall. However, the temporal resolution of radar acquisitions is insufficient to determine whether folding occurred within a few tens of seconds during the earthquake, or within the following hours and days. Truly coseismic folding would imply unstable weakening friction along the bedding planes, corresponding to propagation of flexural slip up-dip of the axial surface at a fraction of seismic shear wave speed. In contrast, flexural slip during the early postseismic period would be compatible with velocity-strengthening friction on the bedding planes that accommodate the deformation. If the spatial distribution of flexural slip — representing only 70% of the maximum expected value — is any indication, the velocity dependence of flexural slip should be strengthening or conditionally stable (Sathiakumar et al., 2020). Otherwise, flexural slip would have propagated

farther up-dip as a self-sustaining process. Regardless, folding appears closely synchronized with seismic ruptures, illustrating the strong mechanical coupling between the two modes of brittle deformation at the time scales of the seismic cycle.

Active blind thrusts have shown their seismic potential on many occasions, e.g., the 1994 Mw 6.7 Northridge, California (Hudnut et al., 1996), 1999 Mw 7.7 Chi-Chi, Taiwan (A. Lin et al., 2001), and the 2005 Mw 7.6 Kashmir, Pakistan (Powali et al., 2020) earthquakes. Better understanding of crustal dynamics in fold-and-thrust belts is therefore paramount to characterize seismic hazard in regions of active shortening. In the past hundred years, the frontal part of the eastern SFT has not experienced any earthquake of Mw>6. In contrast, in the Western and Central SFT, several Mw 6.0 to 6.9 earthquakes occurred in the last decades, including a Mw 6.7 and 6.9 doublet in 1997 in the Sibi Syntaxis (Figure 3.11a) and Mw 6.4 events in 2008 in the Quetta Syntaxis (Figure 3.1a) (Nissen et al., 2016; Reynolds et al., 2015; Usman and Furuya, 2015). Ultimately, earthquakes accommodate fault slip and the frequency of earthquakes is linked to the long-term fault slip-rate. However, long-term slip-rates vary greatly in space and time in fold-and-thrust belts because shortening occurs both by folding and faulting. During periods of crestal narrowing and uplift, when folds grow mostly vertically, the long-term slip-rate of linked fault sections located up-dip of the fold is momentarily reduced (Suppe, 1983). The long-term slip-rate can be homogeneous along dip during the phase of crestal growth, when a synclinal fold extends forward. As the SFT contains many ramps overlain by folds, the frontal section may experience slower long-term slip-rates, gradually diminishing towards the BT. When shortening is taken up by folding within the belt, the frequency of earthquakes towards the foreland should accordingly decrease, possibly explaining the relative scarcity of earthquakes near the deformation front of the SFT belt in the last hundred years. However, as illustrated by the Dajal earthquake, the propagation of faults into the foreland basin can occur seismically, highlighting the potential seismic hazard of deformation fronts. The interactions of faulting and folding in fold-and-thrust belts therefore exert a control on earthquake processes at the time scales of seismic ruptures, guiding their propagation along strike, and at longer time scales, affecting the average frequency of ruptures.

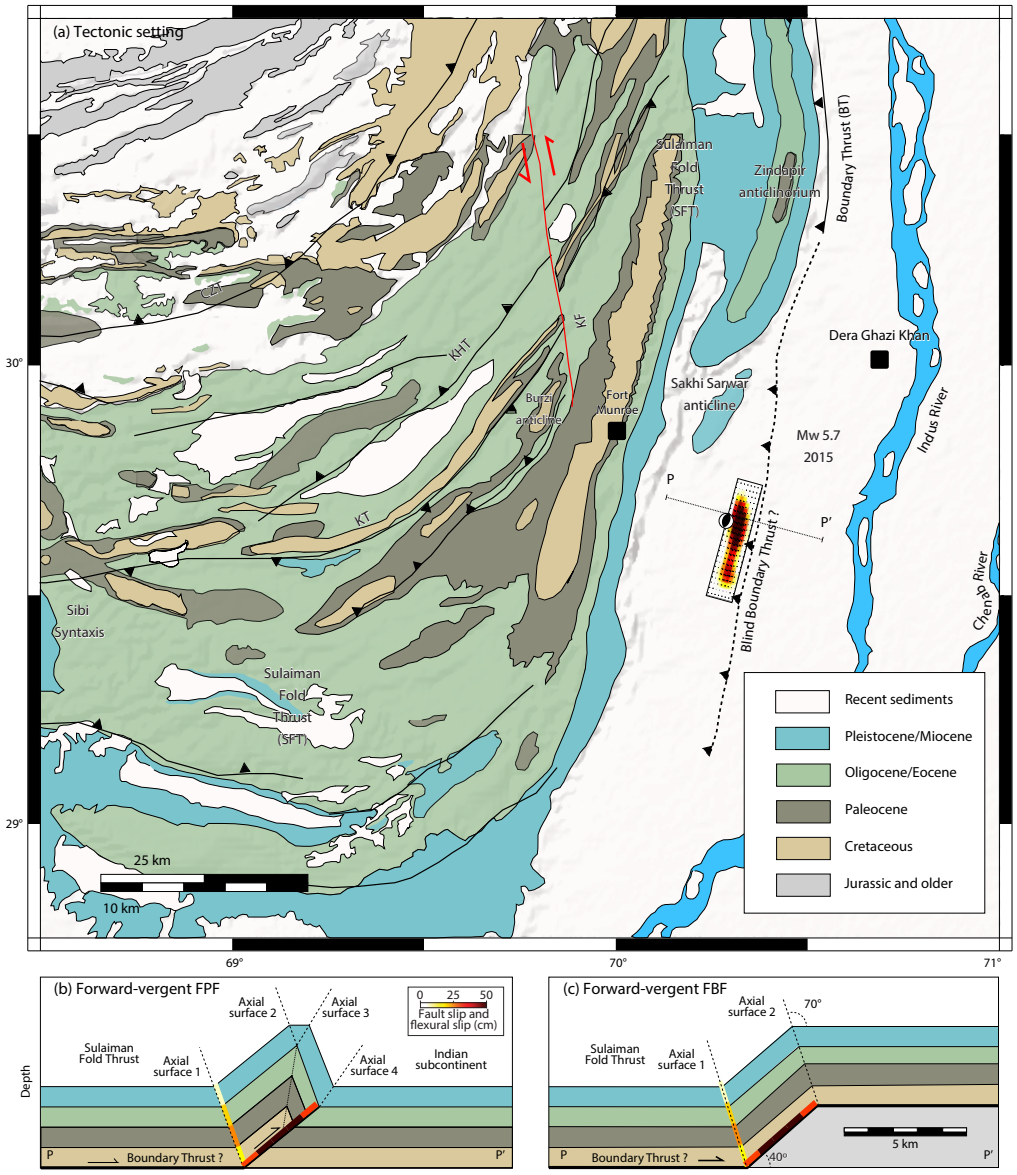

Figure 3.11: Blind frontal ramp of the Eastern SFT. a) The dashed line with chevron is the proposed extension of the BT south of the Zindapir anticlinorium and the Sakhi Sarwar anticline without surface expression. The ramp is buried under recent sediments from the Indus River flood plain, 30 km east of the Eastern SFT. b, c) Cross-sections of FBF and FPF geometries across the Dajal earthquake epicentral area with a FPF extending from the southern extension of the BT buried under Miocene or younger sediments. The colors indicate the concentration of slip on the ramp and flexural slip along the active axial surface. Vertical exaggeration (x1).

3.6 Conclusions

The 2015 Mw 5.7 Dajal, Pakistan earthquake represents the seismic rupture of a frontal blind ramp of the SFT, presumably as the seismic expression of an FBF or FPF. The earthquake illuminates the possible extension of the BT 30 km south of the Zindapir anticlinorium where it breaks the surface, corresponding to the propagation of the SFT some 30 km east into the Miocene and younger sediments of the Indus River floodplain. The earthquake was accompanied by coseismic folding accommodated by flexural slip along an active axial surface. The deformation is captured at the temporal resolution afforded by the radar acquisitions, which includes between 10 and 18 days of potential postseismic deformation. Despite this short period of observation, flexural slip is tantamount to 70% of the expected value for coseismic folding, indicating strong mechanical coupling and synchronicity between faulting and folding at the time scales of the seismic cycle. While the Dajal earthquake demonstrates the seismic potential of the deformation front of fold-and-thrust belts, the folded sediments above the blind ramp exert a strong control on the rupture propagation. Further seismic exploration of fold-and-thrust belts will be crucial to anticipate the location and size of future seismicity in this widespread tectonic setting.

4 Insights into the Western Sulaiman Fold and Thrust belt

Abstract

Continental convergence of Indian and Eurasian plates produces the Himalayan mountain range to the North, while to the East tectonically complex trans-pressional zones of the Sulaiman Fold and Thrust (SFT) belt, and the Kirthar Fold and Thrust (KFT) belt have formed. Seismic hazard in the zones is very high and full understanding is lacking due to trans-compressional complex tectonic setting. Here, we take advantage of spaceborne SAR interferometry and use the Sentinel-1, and ALOS-2 ScanSAR satellite observations to estimate the coseismic deformation caused by the 2021 Mw 6.0 Harnai earthquake in the western zone of the SFT belt. We obtain the line-of-sight (LOS) displacement of 80 and 70 mm from Sentinel-1 descending and ascending interferograms, respectively. We find 50 mm of LOS displacement from the ALOS-2 descending interferogram, but it is majorly biased by lower and upper atmosphere noise even after the GACOS and the ionosphere corrections. In order to avoid the major noise components that may affect the accuracy of the fault displacement inversions, we discarded the ALOS-2 LOS displacement and relied only on the Sentinel-1 data.

The deformation has an oblique component but is mostly dominated by thrusting on the NW-SE trending Harnai fault. First, we invert the LOS displacement using geodetic Bayesian inversion, and find two plausible fault planes which are a NW-SE trending, and a NE-SW trending solution. The simplified fault parameters have a strike of 327°± 12, a dip of 31°± 9, a length of 8.3 ± 2.1 km, and width of 2.5 ± 2.0 km, which fits well with the ISC and USGS fault models. Then, we determine the finite slip distributions on both plausible faults. The NW-SE trending fault shows the maximum slip, which is found to be 70 cm at around 8 km depth. The slip distribution along the down dip and strike of the fault shows that 85 % of the slip is concentrated in an area of (9 × 9) 81 km^2 at a down dip distance of 3 - 12 km. Furthermore, the results show the earthquake propagates along strike and dip. For the NE-SW trending fault the maximum slip is similar but has higher residuals. We prefer the NW-SE trending

fault plane solution because it is compatible with fault structures in the region. We also determine the preseismic and postseismic phases of the 2021 Mw 6.0 Harnai earthquake using SBAS time series analysis of spaceborne Sentinel-1 SAR data, but no significant afterslip signals are found.

4.1 Introduction

The Indian-Eurasian plates convergence is accommodated by the combination of under-thrusting, strike-slip movement, and fold-and-thrust belts. Approximately half of the 36-45 mm/yr northward movement of the Indian plate is absorbed by under-thrusting beneath the Himalayas and the Tibetan plateau (Ul-Hadi et al., 2013; Thatcher, 2007). 17-19 mm/yr of the lateral movement is accommodated along the transform boundary of the Chaman fault (CF) system and the transpressional zones of the Kirthar fold thrust (KFT) and Sulaiman fold thrust (SFT) belts (Jadoon, 1995; Reynolds et al., 2015; Saif-Ur-Rehman et al., 2019; Yadav et al., 2013). The majority of previous studies (England and Houseman, 1986; X. Wang et al., 2017) focused on the northern part of the Indian-Eurasian collision zone to estimate earthquake potential, crustal deformation, fault geometry and seismic hazards. In contrast, the western part of the Indian-Eurasian plates convergence is comparatively less studied due to insufficient seismo-geodetic instrumental coverage. The evolution of the active asymmetric Kirthar and Sulaiman Fold Thrust belts, along with their geological structures, has been reported in numerous studies (Bernard et al., 2000; Reynolds et al., 2015; Saif-Ur-Rehman et al., 2019). However, sources of crustal deformation, fault geometry, lithospheric rheology, and stress orientation on faults are less understood to estimate earthquake potential and associated hazards.

InSAR enables us to investigate sources of crustal deformation accurately in the complicated regions of the SFT belt (Nissen et al., 2016; Pezzo et al., 2014; Usman and Furuya, 2015). The convergence at the western Indian-Eurasian plates margin is partly absorbed by the transpressional zone of the southward-verging SFT belt (Figure 4.1). The analogue and viscoelastic models suggested that the southward movement of the eastern CF block generated the structure and shape of the SFT belt (Bernard et al., 2000; Haq and D. M. Davis, 1997; Jadoon et al., 1993). The southward movement is accommodated with the right-lateral Urghargai fault in the western SFT and left-lateral Kingri fault in the eastern zones of the SFT belt. Overall, crustal shortening has been observed along the seismically active boundary thrust (BT), Zhob Valley fault (ZVF), Karahi thrust (KT), and various blind faults (Figure 4.1).

The central SFT belt is considered the most seismically active zone at the western boundary of the Indian plate, with many devastating earthquakes due to

the complicated and blind network of thrusts, duplex structures, and strike-slip faults (Ambraseys and Bilham, 2012; Banks and Warburton, 1986; Prevot et al., 1980) (Figure 4.1). The fault plane solutions of historical earthquakes in the SFT belt show the region is dominated by thrust and several strike-slip events. We observe the most recent seismicity occurred in the central, and western sides of the SFT belt (Figure 4.1). Two major doublet earthquakes struck in the last two decades near the recent 2021 Mw 6.0 Harnai earthquake (blue colored rectangle in Figure 4.1). First doublet occurred with Mw 6.9 (Nissen et al., 2016) on February 27, 1997, in the southeast of the recent earthquake on the Harnai fault, and the second doublet occurred with Mw 6.4 (Usman and Furuya, 2015) on October 28, 2008, in the northwest of the recent earthquake on a nearby strikeslip fault (Figure 4.1). Both doublets reported numerous fatalities and major economic losses.

To better understand the earthquake source process in the region, we utilize InSAR observations to compute coseismic crustal deformation caused by the 2021 Mw 6.0 Harnai earthquake [30.193°N, 67.995°E]. The epicenter lies in the western zone of the SFT belt on the NW-SE trending Harnai fault (Figure 4.1). The Harnai earthquake occurred on 06 October 2021 at 22:01:08 (Coordinated Universal Time, UTC) 80 km east of Quetta, the most populated city of Balochistan province, Pakistan. We use the Sentinel-1 observations before and after the occurrence of the earthquake. We first estimate simplified source parameters (i.e., dip, strike, depth, width, length, rake, and average slip) by inverting the InSAR interferogram for ascending and descending tracks using the Bayesian inversion approach (Bagnardi and Hooper, 2018; Javed et al., 2022). The seismic source parameters help us understand the regional style of deformation and faulting that control the earthquake magnitude. We then perform finite-fault inversion to constrain the spatial slip distribution of the earthquake.

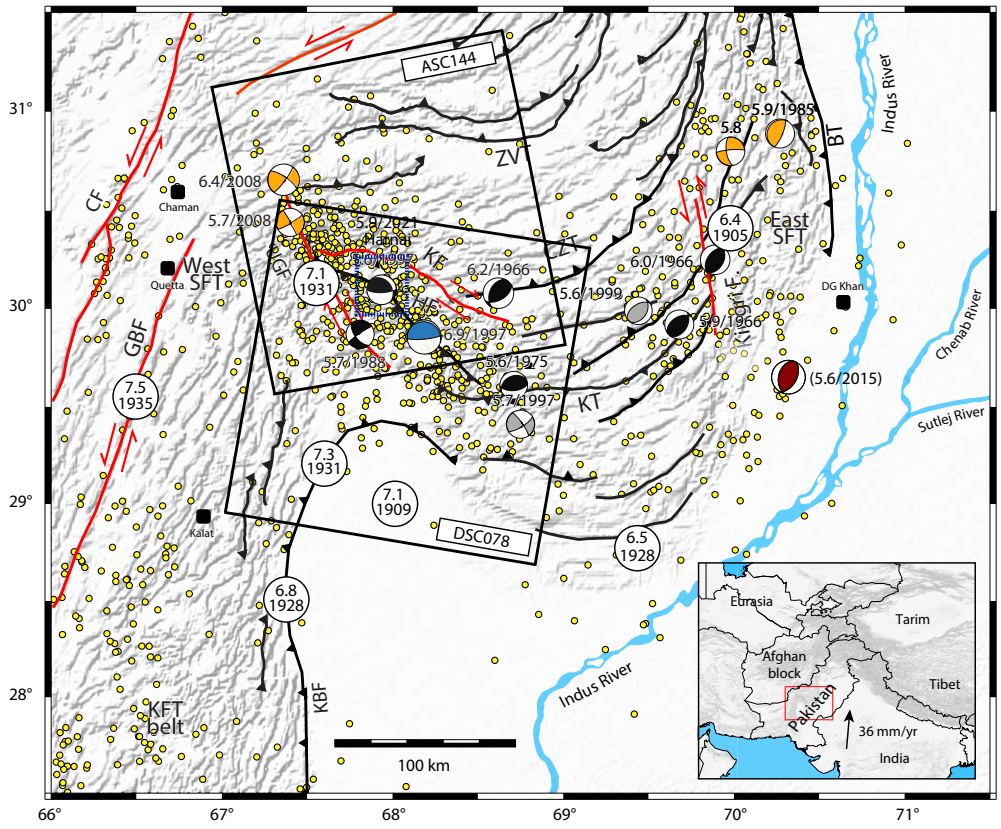

Figure 4.1: Tectonic settings and historical earthquakes (yellow circles) with M>3.5 on SFT belt. a) Faults abbreviated with BT – boundary thrust, CF – Chaman Fault, GBF – Ghazaband Fault, KF – Karahi Fault, KT – Kamari Thrust, HF – Harnai Fault (Pezzo et al., 2014). Focal mechanism solutions in blue (Nissen et al., 2016), orange (Pezzo et al., 2014), GCMT catalog, dark gray (Reynolds et al., 2015), black (Bernard et al., 2000), and white circles (Ambraseys and Bilham, 2003). The black-colored beach solution in a blue rectangle is produced by using inverted fault model parameters of the 2021 Mw 6.0 Harnai earthquake. The inset shows the geographical location of the SFT belt and the relative motion (36 mm/yr) between India and the Afghan block (Ul-Hadi et al., 2013).

4.2 Methodology

4.2.1 InSAR Data Processing

First, we process the Sentinel-1 ascending and descending tracks single-look complex (SLC) products through the GMT5SAR code (Sandwell et al., 2011). The detail of the Sentinel-1 data used in this study is given in Table 4.1. The amplitude of both tracks along with the 1-arc-second DEM model (Farr et al., 2007) is used for co-registration and to produce the topographic phase correction. After producing an unwrapped interferometric phase, co-registration is improved by applying 1) accurate geometric alignment using precise orbit information (Sansosti et al., 2006), 2) removing long wavelength ramp effects (Miranda et al., 2015), and 3) reduction of misregistration (Prats-Iraola et al., 2012). The topographic effect is removed from the phase interferogram using 1-arc-second DEM models, then the phase is unwrapped through the SNAPHU algorithm (C. Chen and Zebker, 2001). However, due to high levels of stratified atmospheric noise correlated with topography, turbulent atmospheric noise, and other sources of scattered noise, the interferograms were not very useful for inverting and estimating the simplified ruptured fault geometry (Figure 4.3a, b) respectively.

To accurately account for the crustal deformation caused by the 2021 Mw 6.0 Harnai earthquake, we perform a time series analysis to calculate the average surface displacement using the SBAS time series analysis (Berardino et al., 2002; Morishita et al., 2020). In this approach, we produce multiple interferograms of Sentinel-1 in the time span of one year constrained with the required small temporal and spatial baselines (Table 4.1). For this scope, we use the LiCSBAS platform (Morishita et al., 2020) that utilizes co-registered unwrapped interferograms of the Sentinel-1 satellites (Lazeckỳ et al., 2020) to calculate the surface displacement in time. We select 103 interferograms for the ascending track (AT144) and 101 interferograms for the descending track (DT078). The interferograms are automatically unwrapped using SNAPHU algorithm at the LiCSBAS platform (C. Chen and Zebker, 2001; 2002; Lazeckỳ et al., 2020; Morishita et al., 2020). The areas with a higher decorrelation than the threshold value of 0.5 are masked out. In addition, it allows us to minimize atmospheric, and orbital errors for each interferogram.

We retain the interferograms that have a perpendicular baseline smaller than 150 m and are least affected by seasonal atmospheric variation to retain a high correlation. Each interferogram is corrected by the path delays produced by atmospheric turbulence using the globally available GACOS corrections. The time series network of the ascending (AT144), and descending (DT078) tracks are shown in Figure 4.2a, b respectively. We have tested the effectiveness of a

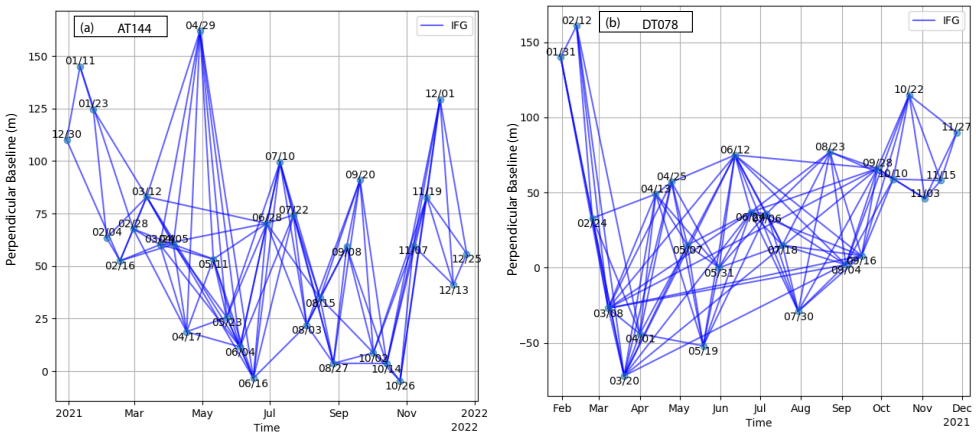

Figure 4.2: Network of ascending (AT144) and descending (DT78) track interferograms used for the SBAS time series analysis with the LiCSBAS software.

spatio-temporal filter to enhance the signal to noise ratio and further eliminate the remaining inaccuracies incurred by the atmosphere. We find however, that applying such filters – for instance, 50 days of temporal, and 40 km spatial filter may over smooth the true deformation produced by tectonic processes– that can introduce a bias which is disturbing for the estimate of the true deformation produced by tectonic processes (Morishita et al., 2020). Finally, we prefer to not apply the spatio-temporal filters, and keep the true deformation for each pixel. However, we remove the long wavelength linear trend by applying a de-ramping function (Morishita et al., 2020). The line-of-sight deformation produced by the 2021 Mw 6.0 Harnai earthquake using SBAS time series in ascending and descending tracks is shown in Figure 4.3c, d respectively.

Table 4.1: Features of Sentinel-1 data

Duration (yy/mm/dd)	Track no.	Perp. baseline (m)	Inc. angle (°)	Head. platform (°)
2021/09/28–2021/10/10	*DES.T*078	15	36 – 39	167 *to* 169
2021/10/02–2021/10/14	*ASC.T*144	9	36 – 39	−11 *to* −12.6
2020/11/28–2021/11/27	*DES.T*078	−75 *to* 150	36 – 39	167 *to* 169
2020/12/26–2021/12/25	*ASC.T*144	0 *to* 160	36 – 39	−11 *to* −12.6

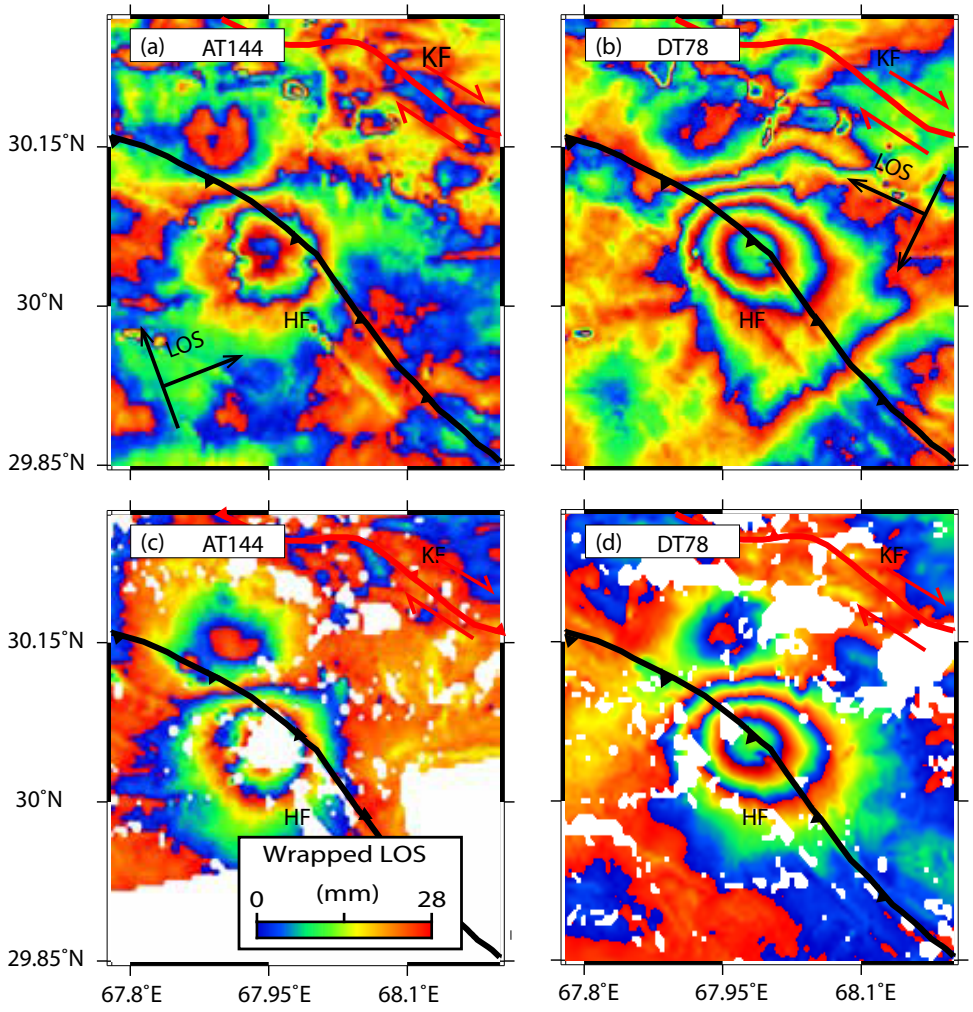

Figure 4.3: Comparison of using single pair of interferograms and multiple pairs of interferograms of ascending and descending tracks to estimate coseismic deformation of the 2021 Mw 6.0 Harni earthquake (a, b) Coseismic deformation obtained through GMTSAR software using a single pair of interferograms. (c, d) Coseismic deformation obtained through SBAS time series in LiCSBAS software using multiple pairs of interferograms. KF – right lateral Karahi Fault, HF – thrusting Harnai Fault

4.2.2 Error Estimation

Before running the Bayesian inversion, we estimate the variance and covariance in the datasets to determine the errors, produced by phase decorrelation. The phase decorrelation can occur due to uneven distribution of water vapor content in the lower atmosphere and turbulence of ions and currents in the upper atmosphere (Hanssen et al., 1999). In addition, it can also be encountered due to steep topographic variation at the site and anisotropic spatial variability (Knospe and S. Jonsson, 2009).

Presumably, satellite-based interferograms are spatially correlated and ionosphere structures are considered coherent over a scale of hundreds of kilometers. However, water vapor content varies unevenly with topography which can introduce delays in LOS direction (Emardson et al., 2003; P. Jonsson and Eklundh, 2002). Therefore, we estimate the spatial variability of both ascending and descending interferograms using a semi-variogram (Wackernagel, 2003) by measuring the dissimilarity among the processed interferogram. In order to accurately account for the long wavelength ramp, we perform the semi-variogram analysis over an area 10 times larger than the area that is subjected to surface deformation and calculate the range, sill, and nugget values for the ascending and descending interferograms separately (Table 4.2).

Table 4.2: Detail of interferogram errors calculated using semi-variogram

Track	Sill $(mm)^2$	Nugget $(mm)^2$	Range (km)	Threshold $(mm)^2$	Subsample (points)
$DES - T078$	0.14	10.1×9.04^{-6}	10.1	1.2×10^{-4}	733
$ASC - T141$	0.024	2.79×10^{-15}	3.2	4.5×10^{-2}	648

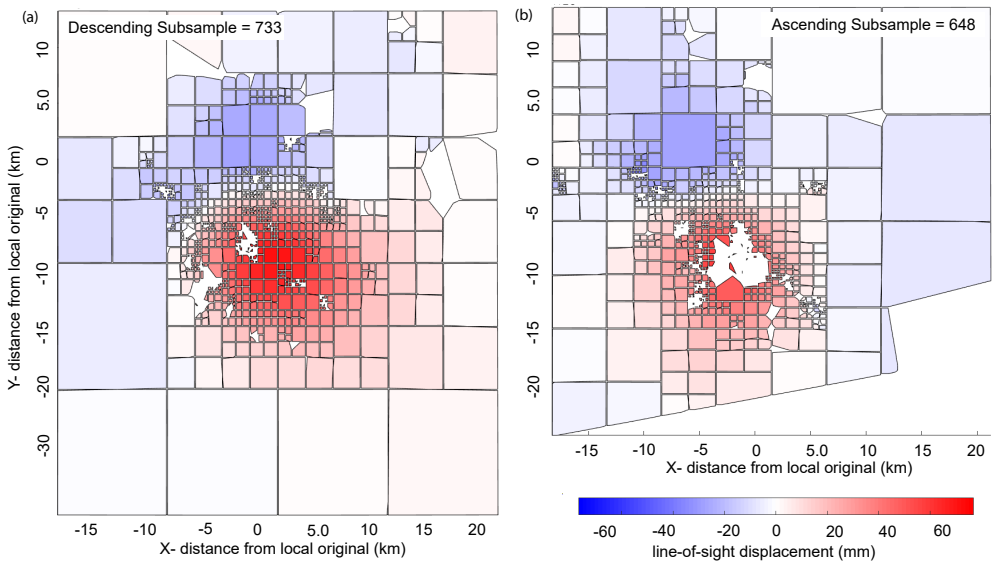

Figure 4.4: Subsampling of ascending (AT144) and descending (DT78) track interferograms using Bayesian inversion.

4.3 Kinematic Inversions

4.3.1 InSAR Modeling

We estimate the fault rupture geometry such as fault dip, strike, length, width, rake, slip, epicentre location, and depth of the 2021 Harnai earthquake by inverting Sentinel-1 ascending and descending SBAS time series LOS displacement (Figure 4.3c, d) using the Bayesian inversion (GBIS) approach (Bagnardi and Hooper, 2018; Javed et al., 2022). After estimating the semi-variogram parameters, we subsample the datasets to reduce the computational cost and obtain enough samples that accurately depict the true surface displacement. We downsample the full-resolution ascending interferogram (AT144: 648) and descending interferogram (DT078: 733) using a quadtree gradient-based approach (Simons et al., 2002) (Figure 4.4a, b). It recursively divides the surface deformation into further four polygons unless we achieve the threshold variance for ascending ($4.5 \times 10^{-2}\ mm^2$) and descending ($1.2 \times 10^{-4}\ mm^2$) interferograms as given in Table 4.2. The density of the subsamples is directly proportional to the areas with high gradient surface displacement (Figure 4.4a, b).

We generate a synthetic model in a homogeneous elastic half-space based on a uniform rectangular dislocation model (Okada, 1992). The Okada model has been proven effective in simulating coseismic deformation caused by earthquakes (Barbot et al., 2023; Barkat et al., 2022; Garthwaite et al., 2013; Javed et al., 2022; H. Wang et al., 2017; W. Xu et al., 2018). In this model, all source fault

parameters except the slip over the fault are non-linearly related to the surface deformation. However, the fault slip is proportional to surface displacement. The search parameters are shown in Table 4.3.

The posterior PDF of search fault model parameters of the 2021 Mw 6.0 Harnai earthquake have been characterized by using the MCMC algorithm (Mosegaard and Tarantola, 1995; Sambridge and Mosegaard, 2002). We constrain the step size automatically through the Metropolis-Hastings algorithm (Hastings, 1970). The Bayesian inversion approach utilizes the InSAR to characterize Posterior PDFs of search fault parameters and estimate uncertainties. Moreover, we also utilize some available prior information (USGS and Shaukat et al., 2023) of the fault model parameters of the 2021 Mw 6.0 Harnai earthquake. Initially, we applied no constraints on the fault model parameters, for instance, we kept the strike range 0° *to* 360°, and dip range $+90^{\circ}$ *to* -90° along with other fault parameters to insight all possible outcomes of the kinematics of the ruptured fault. After multiple trials, the final ranges of the fault model parameters were selected based on the minimum residual and consistency. After inverting, an optimal set of fault model parameters has been computed from the posterior PDF for the 2021 Mw 6.0 Harnai earthquake by calculating the maximum of posterior probability solutions (Table 4.3).

As mentioned above, the ALOS-2 acquisitions were also available, and we tested adding these data to the inversion of both track interferograms from Sentinel-1 and the ALOS-2 descending track LOS displacement. We find that ALOS-2 ScanSAR data are affected by a major ionospheric and tropospheric atmospheric noise which increases the uncertainty and makes the results incorrect (Figure 2.9). Therefore we discard the ALOS-2 data and constrain the fault models using only ascending and descending Sentinel-1 data to fully explore the posterior PDF with a feasible uncertainty level of the ruptured fault parameters.

4.4 Results and Discussion

4.4.1 Results

The ascending and descending interferograms show the surface deformation of approximately 70 and 80 mm along their respective LOS direction. Synthetic models with a single fault patch agree well with InSAR observed data, with average residuals in the order of 2 mm for both interferograms in the deformation zone (Figure 4.5, 4.8). We efficiently categorize the posterior PDF of the ruptured fault geometry of the 2021 Harnai earthquake with automatic step size using the Metropolis-Hastings algorithm and the Monte Carlo Markov chain method (Hastings, 1970; Metropolis et al., 1953; Tarantola, 2005). We

use 10^7 iterations to define posterior PDF, discarding the first 20,000 samples (Figure 4.6, 4.9).

We find two plausible fault plane solutions for the rupture propagation of the 2021 Harnai earthquake named (1) the NW-SE trending rupture model and (2) the NE-SW trending rupture model. Both solutions agree well with InSAR observation in terms of deformation. The calculated parameters of both rupture models along with the fault parameters calculated by USGS and (Shaukat et al., 2023) using seismic waveform data are given in Table 4.3.

4.4.1.1 The NW-SE Rupture Model

The NW-SE trending rupture models are consistent and agree well with surface deformation observed by InSAR in both ascending (Figure 4.5a - c) and descending interferograms (Figure 4.5d - f). The first plane has NW-SE trending strike with a shallow dipping rupture, and the second one has a NE-SW trending strike with a steep dipping rupture. The NW-SE trending fault plane solution has a dip of 31° ± 9, and strike of 327° ± 12, depth of 8.3 ± 2.1 km. The seismic moment (M_o) is calculated using the mean value of source model parameters with fault rupture area $A = 20.75\,km^2$, average slip $s = 2.4 \pm 1.1\,m$, assuming a Poisson's ratio of 0.25 and a shear modulus of $\mu = 32.0\,GPa$. The estimated seismic moment $M_o = 1.6 \times 10^{18}\,Nm$ corresponds to $Mw = 6.0$. The posterior PDF of each source fault model is shown in Figure 4.6. Histograms of ruptured fault model parameters are generated during the Bayesian inversion with 10^7 iterations. The y-axis shows the probability density based on 10^7 iterations with 95% confidence interval. In order to evaluate the quality of inversions, we also check the convergence of each ruptured fault model parameter as shown in Figure 4.7. Each fault parameter converges well around the average and optimal value of the fault parameter.

4.4.1.2 The NE-SW Rupture Model

The second fault plane solution, NE-SW trending rupture is also found consistent and agrees well with the spaceborne SAR deformation of the 2021 Harnai earthquake in both ascending (Figure 4.8a - c) and descending interferograms (Figure 4.8d - f). This model has a NE-SW trending strike with a steeply dipping rupture at the depth of approximately 13 km. The rupture geometry has a dip of 76° ± 4, and strike of 77° ± 7, depth of 13 ± 3.5 km. The seismic moment (M_o) is calculated using the mean value of source model parameters with fault rupture area $A = 18\ km^2$, average slip $s = 3.5 \pm 1.5\,m$, assuming a Poisson's ratio of 0.25 and a shear modulus of $\mu = 32.0\ GPa$. The estimated seismic moment $M_o = 2.0 \times 10^{18}\,Nm$ corresponds to $Mw = 6.0$. The posterior PDF of each

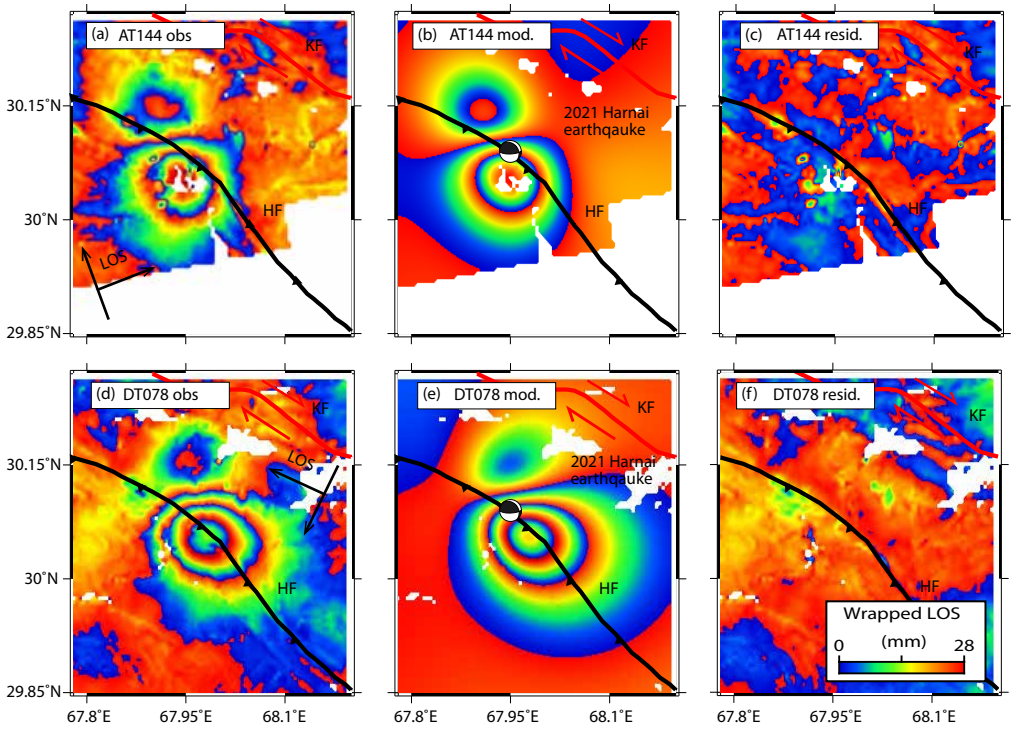

Figure 4.5: Uniform fault plane solution obtained NW-SE trending model by using GBIS approach a, b) observation, c, d) synthetic interferogram and e, f) residual of the ascending track (AT144) and descending track (DT78) respectively. The deformation along the LOS displacement is approximately 70 mm and 80 mm. The focal mechanism solution (black colored) is produced by using inverted ruptured NW-SE trending model.

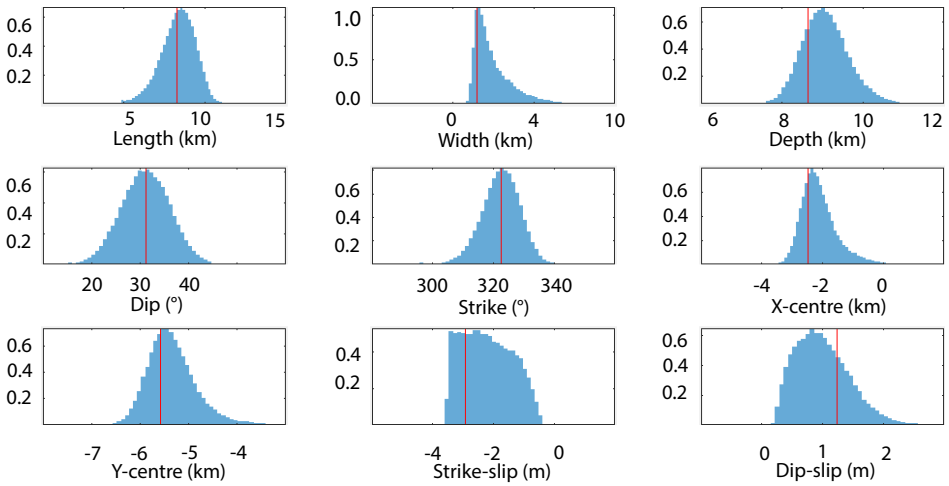

Figure 4.6: Histograms of NW-SE trending ruptured fault model parameters through Bayesian inversion approach with 10^7 samples. The y-axis represents the probability density, and the red line indicates the optimal model values with 95% confidence interval

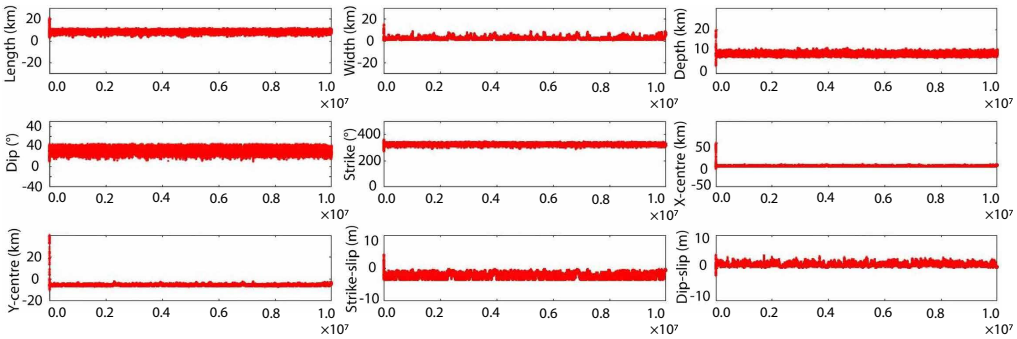

Figure 4.7: Convergence of NW-SE trending ruptured fault model parameters through Bayesian inversion approach with 10^7 samples. The y-axis represents the range of fault parameters, while the x-axis shows the number of samples used in the inversions.

source fault model is shown in Figure 4.9. Histograms of ruptured fault model parameters are generated during the Bayesian inversion with 10^7 iterations. The y-axis shows the probability density based on 10^7 with 95% confidence interval. Each fault parameter converges well around the average and optimal value of the fault parameter.

The ruptured fault geometry of the Harnai earthquake demonstrates the epicenter location of the earthquake is slightly southwest of the epicenter proposed by the USGS, and (Shaukat et al., 2023). Our derived moment magnitude is slightly higher than the one calculated by USGS based on seismoloical observations. Inverted ruptured fault parameters are in good agreement with the USGS results, and (Shaukat et al., 2023) including a moment magnitude $Mw = 6.0$ calculated by InSAR, and $Mw = 5.94$ by USGS (Table 4.3). Two moment tensor solutions for the Mw 6.0 Harnai earthquake have been provided by USGS and (Shaukat et al., 2023). All fault plane solutions of the 2021 Harnai earthquake proposed by USGS, and InSAR indicate the compressional regime along with a strike-slip component which is compatible with the tectonic settings of the regime. Our results show the inversions of both interferograms constrain the posterior probability density functions efficiently and approximate the target distribution adequately (Table 4.3).

4.4.1.3 Finite Fault Slip Distribution

We invert the kinematic slip for two plausible fault plane solutions i.e. the NW-SE trending strike (Figure 4.10), and (Figure 4.11) and the NE-SW trending strike (Figure 4.12), and (Figure 4.13). We constrained the finite fault slip distribution through the least square inversions method (Barbot et al., 2023; Javed et al., 2022). We fix the strike and dip based on the ruptured fault geometry of the

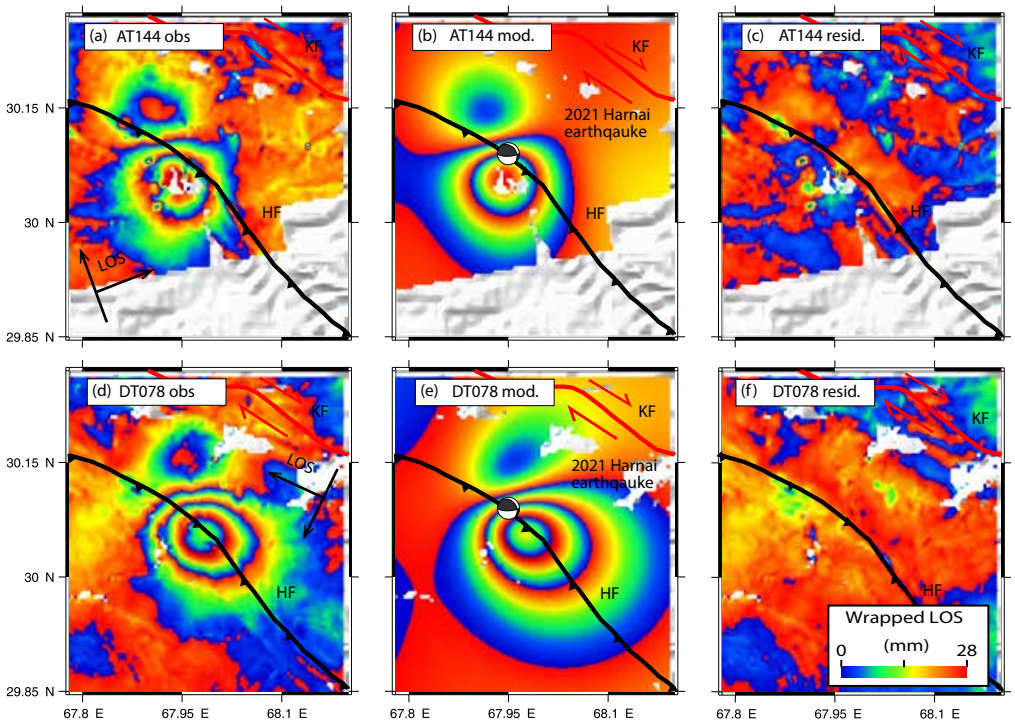

Figure 4.8: Uniform fault plane solution obtained NE-SW trending model by using GBIS approach a, b) observation, c, d) synthetic interferogram and e, f) residual of the ascending track (AT144) and descending track (DT78) respectively. The deformation along the LOS displacement is approximately 70 mm and 80 mm. The focal mechanism solution (black colored) is produced by using an inverted ruptured NW-SE trending model.

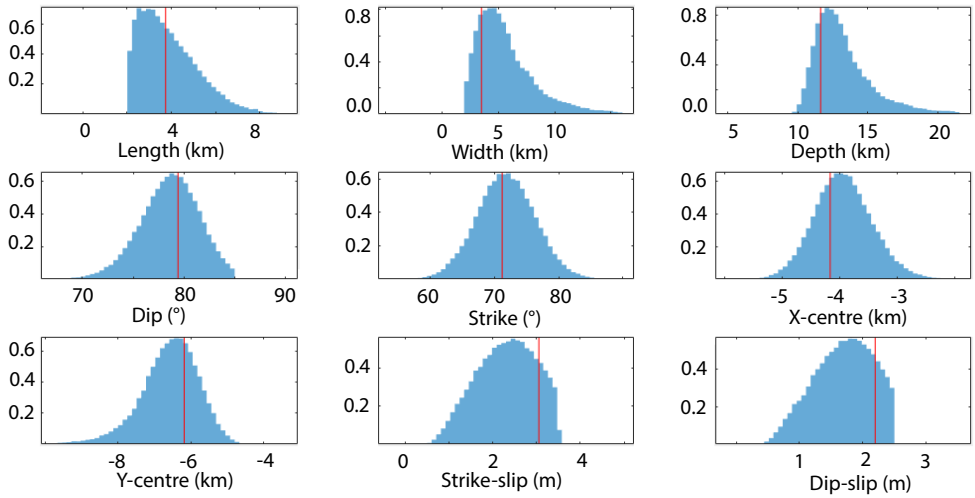

Figure 4.9: Histograms of NE-SW trending ruptured fault model parameters through Bayesian inversion approach with 10^7 samples. The y-axis represents the probability density, and the red line indicates the optimal model values with 95% confidence interval

Table 4.3: The inverted ruptured fault parameters using Sentinel-1 ascending and descending deformation data

models	lon (°)	lat (°)	str. (°)	dip (°)	rake (°)	len. (km)	wid. (km)	dep. (km)	slip (m)	M_o $\times 10^{18}$ (Nm)	Mw
USGS	67.99 -	30.19 -	292 57	20 78	144 74	- -	- -	9.0 -	- -	1.02 -	5.94 -
Shaukat et al., 2023	67.99 -	30.19 -	309 65	27 78	152 67	- -	- -	12.0 -	- -	- -	5.9 -
InSAR (NW-SE)	67.95 ± 0.012	30.09 ± 0.009	327 ±12	31 ±9	160 ±6	8.3± 2.1	2.5 ± 2	8.9± 1.1	2.4 ±1.1	1.6 ±1.4	6 ± 0.5
InSAR (NE-SW)	-	-	77 ± 7	76 ±4	65 ±9	3 ± 1.5	6 ± 3.5	13± 3.5	3.5 ±1.5	2.0 ±1.4	6 ± 0.56

2021 Mw 6.0 Harnai earthquake, requiring a small strike rotation from the simplified geometry model. We extend the width and length of the fault plane to the ground surface and discretize the slip. We discretize the NE-SW fault model into 625 rectangular fault patches, and the NW-SW trending fault model into

324 rectangular fault patches with along-strike and down-dip slip components (Okada, 1992). We use an L-curve to resolve the tradeoff between smoothness and residual size (Barbot et al., 2023). We calculate slip distribution models based on variable smoothening factor i.e. k = 0.001, k = 0.002, k = 0.01, and k= 0.02, but the best solutions are found to be at k = 0.001 for both fault models.

The NW-SE trending rupture surface models with residuals and finite slip distribution is shown in Figure 4.10, and 4.11. The observations fit well synthetic models upto 97% for ascending track (Figure 4.10a - c) and approximately 92% for descending track (Figure 4.10d - f) interferograms. The residuals between the observations and models are found to be less than 6 mm. We divide the uniform fault into 18 × 18 rectangular patches along dip and strike to estimate the coseismic slip distribution of Mw 6.0 2021 Harnai earthquake on a 31° dipping, and 327° strike fault from north (Figure 4.11a). The maximum slip is found to be 70 cm at around 8 km depth. The slip distribution along the down dip and strike of the fault shows that 85% of the slip is concentrated in an area of (9 × 9) 81 km^2 at a down dip distance of 3 - 12 km (Figure 4.11b). Furthermore, the results show the earthquake rupture propagates equally along strike and dip, without reaching the surface around the epicenter.

The NE-SW trending rupture surface models and residuals generated by finite slip inversions are shown in Figure 4.12. The observations fit well synthetic models with approximately 89% for the ascending track (Figure 4.12a - c) and 85% for the descending track (Figure 4.12d - f) interferograms. The residuals between the observations and models are found to be less than 10 mm. We divide the uniform fault into 25 × 25 rectangular patches along dip and strike to estimate the coseismic slip distribution of Mw 6.0 2021 Harnai earthquake on a 76° dipping, and 77° strike fault from North (Figure 4.13a). The maximum slip is found to be 50 cm at around 7 km depth. The slip distribution along the down dip and strike of the fault shows that 80% of the slip is concentrated in an area of (7 × 10) 70 km^2 at a down dip distance of 3 - 10 km (Figure 4.13b). Furthermore, the results show the earthquake rupture propagated along dip, without reaching the surface around the epicenter.

4.4.2 Discussion

Trans-compressional faults are important tectonic features in the SFT belt and the deformation along these faults often occurs due to combined compressional and strike-slip movement. However, these fault systems are very complicated and mostly characterized by bending and step-over faults along the main fault (Barka and Kadinsky, 1988; Javed et al., 2022; Sathiakumar and Barbot, 2021). Several examples of such active complex fault systems i.e., the Gargano fault system in central Adriatic region (Billi et al., 2007), North Anatolian fault system

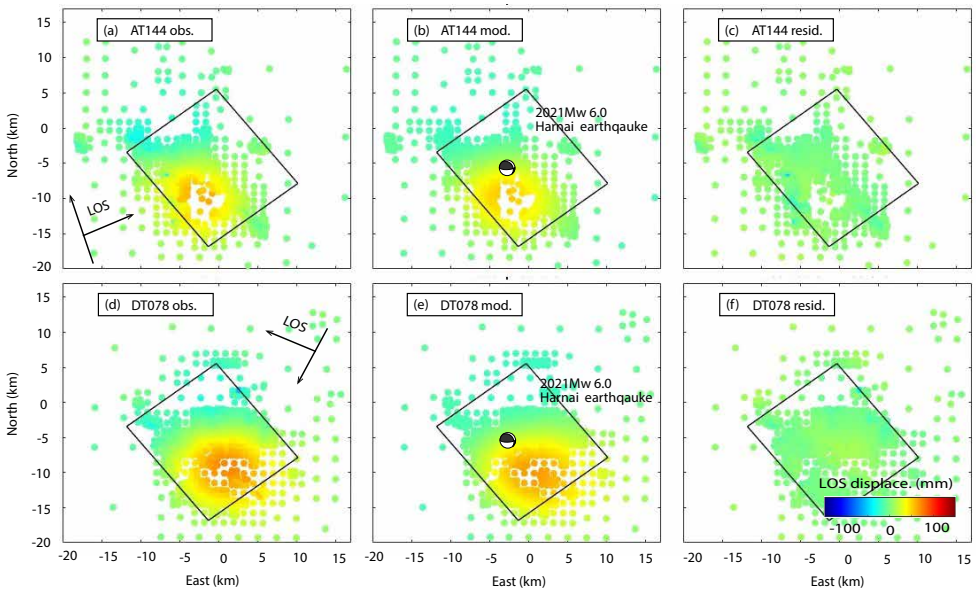

Figure 4.10: The kinematic finite slip surface deformation models obtained from the NW-SE trending rupture of the 2021 Mw 6.0 Harnai earthquake. (a, d) Ascending and descending InSAR observations. (b, e) Ascending and descending synthetic models. (c, f) Ascending and descending residuals, respectively. The maximum of co-seismic deformation along the LOS displacement is around 70 mm, and 80 mm along the line-of-sight direction with less than 6 mm residual for both ascending and descending interferograms respectively. Focal mechanism obtained from Bayesian inversions using NW-SE trending rupture fault model.

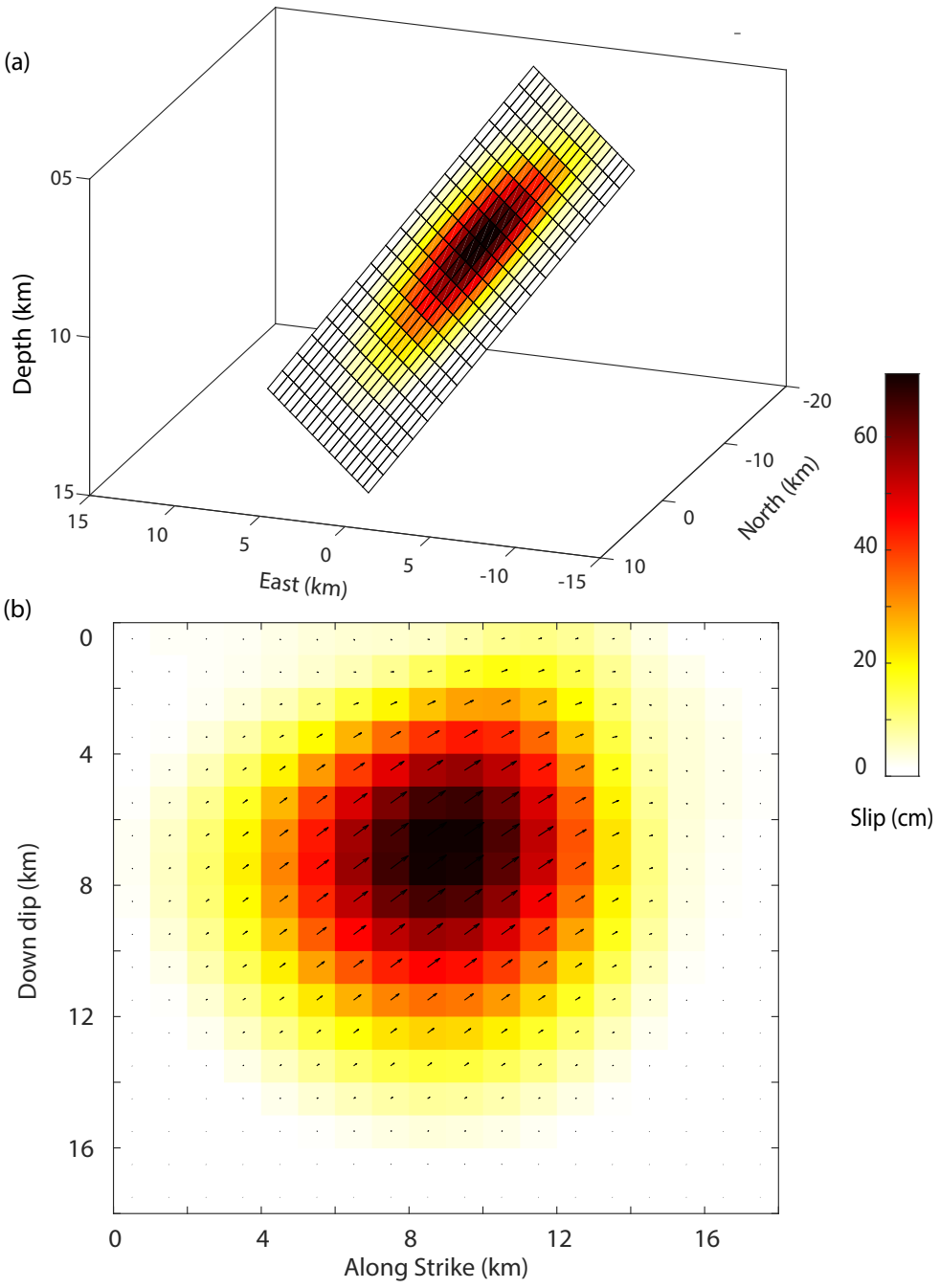

Figure 4.11: Kinematic rupture model of the Mw 6.0 Harnai earthquake (a) 3D coseismic slip distribution on the NW-SE trending rupture model estimated from Bayesian inversion. (b) 2D coseismic slip distribution along the dip and strike of the NW-SE trending fault.

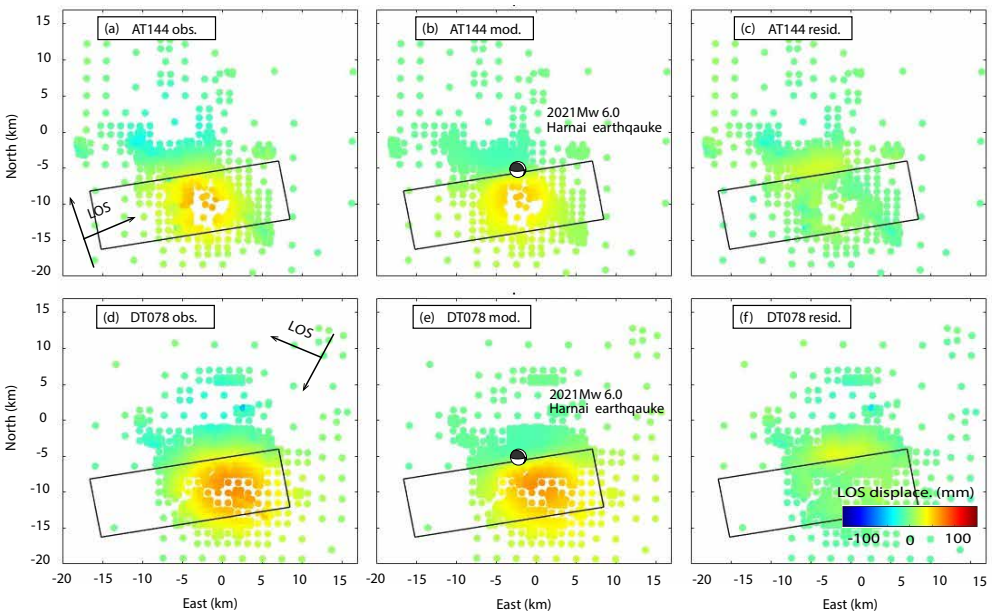

Figure 4.12: The kinematic finite slip surface deformation models obtained from NE-SW trending rupture of 2021 Mw 6.0 Harnai earthquake. (a, d) Ascending and descending InSAR observations. (b, e) Ascending and descending synthetic models. (c, f) Ascending and descending residuals, respectively. The maximum LOS displacement is 70 mm, and 80 mm in the ascending and descending interferograms respectively. Focal mechanism obtained from Bayesian inversions using NE-SW trending rupture fault model.

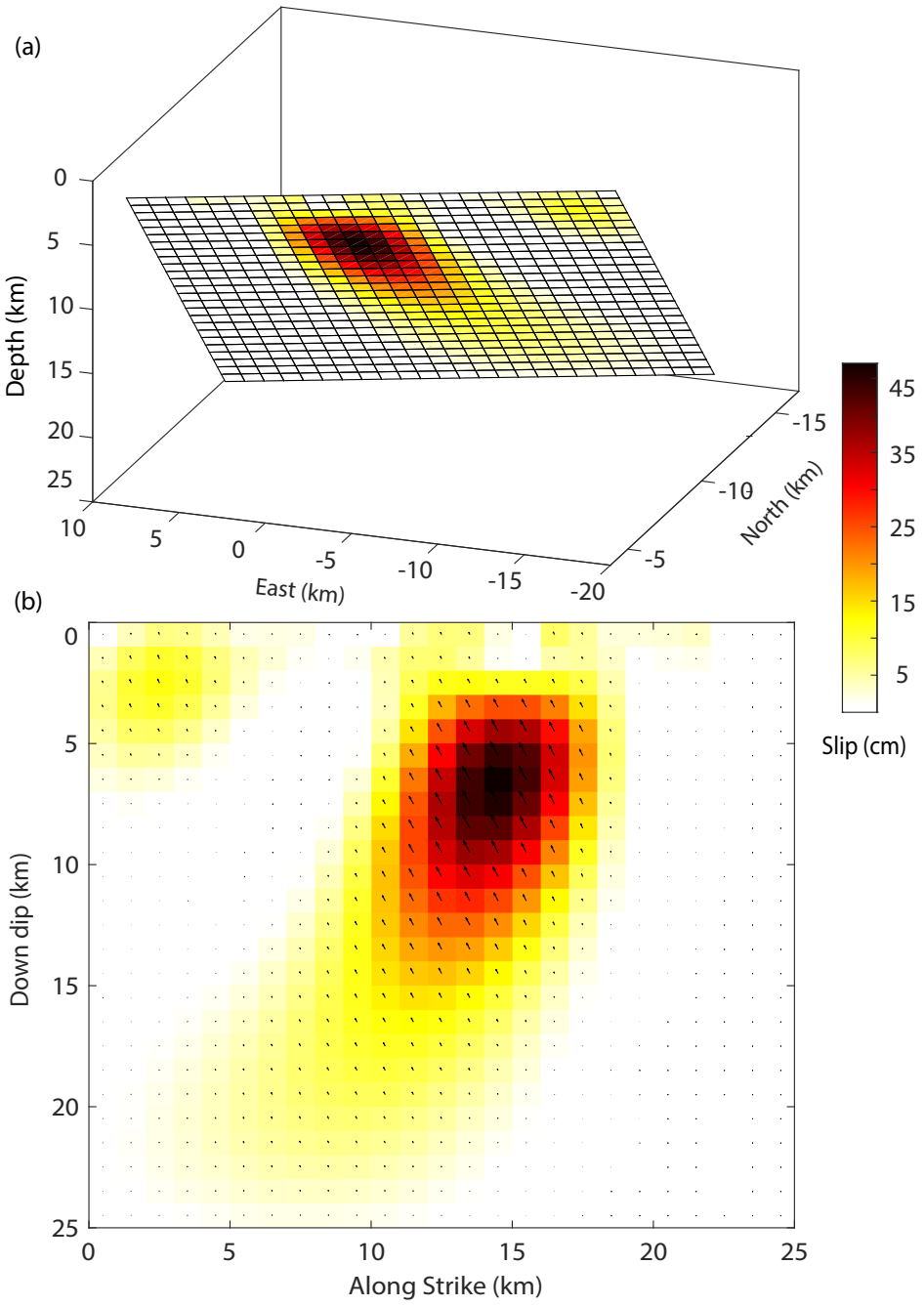

Figure 4.13: Kinematic rupture model of the Mw 6.0 Harnai earthquake (a) 3D coseismic slip distribution on the NE-SW trending rupture model estimated from Bayesian inversion. (b) 2D coseismic slip distribution along the dip and strike of the NE-SW trending fault.

(Barka, 1996; Hamiel and Fialko, 2007; Şengör et al., 2005; Wright et al., 2001), Marlborough fault system in New Zealand (Mason and Little, 2006; W. Xu et al., 2018) and San Andreas fault system (Barbot et al., 2013; Chang et al., 2013) are widely known for high seismicity.

The complicated fault geometries in trans-compressional regions are considered to affect the nucleation and rupture propagation that ultimately controls the magnitude of an earthquake (King and Nábělek, 1985; Wesnousky, 2006). Recently, on 06 February 2023 the Mw 7.8 Kahramanmaraş, and Mw 7.6 the Elbistan earthquakes ruptured the major part of the EAF from the southern termination of the Pütürge segment to the Antakya fault near the DSF (Barbot et al., 2023). Both major earthquakes have ruptured the 13 major segments of the EAF system during the coseismic phase of the earthquake. However, the stress transfer of the Mw 7.8 Kahramanmaraş earthquake to the Mw 7.6 the Elbistan earthquakes still need to be determined. Similarly, the 2016 M 7.8 Kaikoura earthquake occurred on the Marlborough branching fault system that ruptured at least 21 fault segments and produced approximately 10 m coseismic surface displacement (Ando and Kaneko, 2018; W. Xu et al., 2018). The off-fault deformation has also been observed due to the occurrence of multiple earthquakes with $Mw \geq 5.7$ before the mainshock of the Kaikoura earthquake.

The trans-compressional fault system of the SFT belt is also complicated and characterized by buried faults, fault-bend folds, branches, ramp-décollement fault systems, and step over structures across thrust and strike slip faults (Javed et al., 2022; Karaca et al., 2021; Saif-Ur-Rehman et al., 2019; 2020). Moreover, active blind thrusts are proved to be seismic hazards that sometimes may cause significant destruction due to lack of knowledge and preparation, such as the recent 2019 Mw 5.8 Mirpur earthquake in Pakistan (Barkat et al., 2022), 2017 Mw 6.1 Sangsefid earthquake (Ghayournajarkar and Fukushima, 2020), 2016 Mw 5.9 Menyuan earthquake (H. Wang et al., 2017), 2013 Mw 7.0 Lushan earthquake (X. Xu et al., 2013), 2003 Mw 6.5 Bam earthquake (Fialko et al., 2005; Fielding et al., 2009).

The SFT belt represents the complex active tectonic deformation and exhibits complex tectonic structures such as fault-propagation folds, bookshelf structures, and fault-bend folds. The frontal SFT belt mostly hosted moderate-size earthquakes, while the western side hosted major earthquakes in the region (Figure 4.1). A key question that requires attention is why moderate-sized seismic activity is observed along the frontal zone of the SFT belt, in contrast to the western zone. Do geometric complexities or fault dimensions exist in the frontal SFT belt zone that control the coseismic slip propagation? Javed et al. (2022) shows the frontal SFT belt exhibits complicated tectonic structures e.g. fault-propagation fold, and fault-bend-fold consists of a shallow décollement that branches into a narrow ramp. These complicated structures may control the

coseismic slip propagation, eventually control the size of earthquakes (Namson and T. L. Davis, 1988; Sathiakumar and Barbot, 2021; Sathiakumar et al., 2020; Weng and Yang, 2017).

The western SFT belt has a complex combination of thrust and strike-slip movement, and a mature fold-and-thrust fault system, passive roof duplex structures, and en-echelon structures (Karaca et al., 2021; Saif-Ur-Rehman et al., 2019; 2020). The continental-scale 850 km long sinistral Chaman fault (CF) that marks the western segment of the Indian and Eurasian plate boundary, played a significant role in the evolution of the structure and shape of the SFT belt (Bernard et al., 2000; Haq and D. M. Davis, 1997; Karaca et al., 2021) . The strike of the CF is approximately 10° to 35° and the slip rate along the SFT belt is about 19-24 mm/yr (Ul-Hadi et al., 2013; Lawrence and Yeats, 1979). The azimuth of the northward movement of the Indian plate is approximately $N12°E$ against the $N34°E$ average azimuth of the CF, that produces strain partitioning in the SFT belt (Bernard et al., 2000; Karaca et al., 2021) (Figure 4.1).

The southward motion of the SFT is compensated by the right-lateral Urghargai fault (UGF) on the western SFT belt and the left-lateral Kingri fault on the frontal SFT belt. The northward movement and underthrusting of the Indian plate are being accommodated with the Boundary thrust (BT) and Zhob valley thrust (ZVT), which produced several major earthquakes in the last three decades (Ambraseys and Bilham, 2003; Bernard et al., 2000; Reynolds et al., 2015) (Figure 4.1).

In the western SFT belt, a few major earthquakes have been reported along with two doublet events Mw 6.9 in 1997 in the Sibi Syntaxis around 80 km SE of the 2021 Harnai earthquake epicentre, and 11 years later another doublet Mw 6.4 in 2008 in the Quetta Syntaxis around 150 km NW of the recent 2021 Harnai earthquake epicentre (Nissen et al., 2016; Reynolds et al., 2015; Usman and Furuya, 2015) (Figure 4.1). In 2016 Nissen et al. (2016) shows that the coseismic slip of the Sibi doublet occurred on two different buried thrust faults between depths of 10 and 20 km respectively. The initial rupture occurred over a shallow blind Harnai fault and triggered the second thrust fault separated by 50 km in just 19 seconds. It is evident that the fault dimensions and geologic structures in the western SFT belt are complicated and at small distances from each other which may favor triggering the rupture propagation to the adjacent faults and produce major earthquakes.

The right lateral Karahi fault and thrusting Harnai fault are two NW-SE trending transpressive parallel faults and are subjected to major sources of seismicity from moderate to large magnitude earthquakes in the western zone of the SFT belt. The KF shows the right lateral movement, while HF is a blind thrust fault with a foot wall in the north, and a hanging wall in the south of the fault (Figure 4.1). The HF which is the causative fault of the 2021 Mw 6.0

Harnai earthquake shows no significant movement prior to the earthquake as analyzed by (Karaca et al., 2021) using space-borne satellites, controlled seismic source data, and borehole data. InSAR time series analysis presented in (Karaca et al., 2021) shows the HF is locked prior to 2021, while right lateral movement is observed at the KF at the rate of approximately 15 mm/yr in the descending and approximately 10 mm/yr in the ascending track parallel to the HF.

In order to assess the afterslip on the HF due to the 2021 Mw 6.0 Harnai earthquake, we perform SBAS time series analysis of spaceborne Sentinel-1 SAR data (Figure 4.14 and 4.15). We follow similar SAR data processing methods and a set of parameters described in Section 4.2.1 through the LiCSBAS (Morishita et al., 2020) platform in the period of December 2020 to December 2022 to analyze the preseismic and postseismic deformation. However, we find no significant pre-seismic and post-seismic phase movement around the deformation zone at point P1 on 30.0347° N, 67.9470° E, and point P2 on 30.146° N, 67.9020° E in ascending descending track interferograms (Figure 4.14c, d and 4.15c, d). We also plot the profile AA' across Harani fault covering the positive and negative LOS displacement produced by the earthquake (Figure 4.14a and 4.15a). We find the positive velocity (movement toward satellite) of around 45 mm/yr in the ascending track (Figure 4.14b), and 55 mm/yr in the descending track (Figure 4.15b). We find a negative velocity of around -30 mm/yr in the ascending and -20 mm/yr in the descending tracks at the footwall segment of the Harnai fault (Figure 4.14b and 4.15b).

Overall, the 2021 Mw 6.0 Harnai earthquake ruptured the fault in the up-dip direction at a depth of 8 km. Most of the deformation is observed in the hanging i.e. at the southern margin of the Harnai fault. We propose our NW-SE rupture model as a preferred causative fault because it correlates with the tectonic settings of the region and the geologic structure of the Harnai fault, while the NE-SW model is incompatible with the Harnai fault. In addition, the NW-SE model explores the observations well, with residuals less than 6.0 mm, while the NE-SW model exhibits a slightly higher residual of the order of 10 mm. Furthermore, the slip distribution of the NW-SE model exhibits more internal consistency than the NE-SW rupture model.

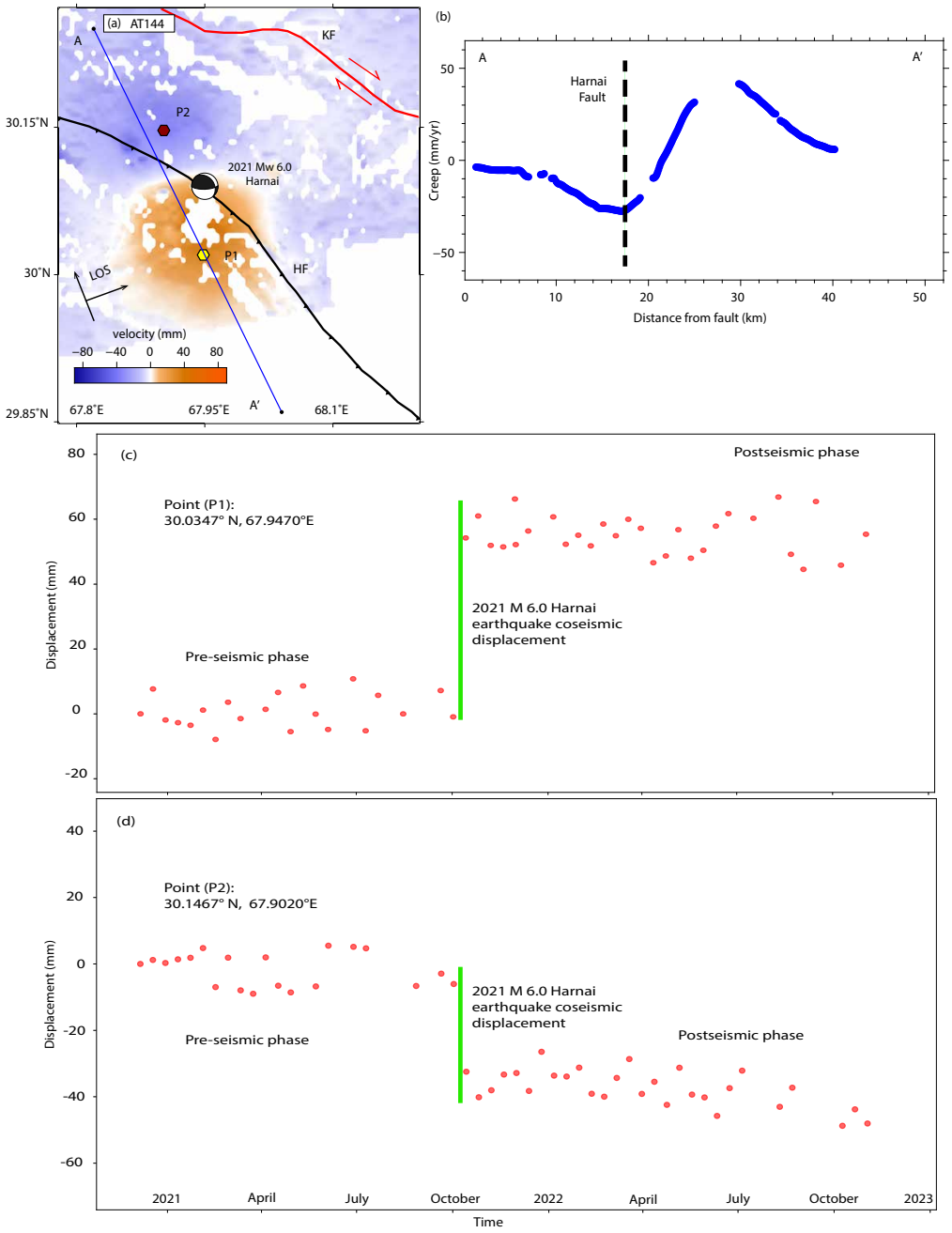

Figure 4.14: Slip rates of ascending track AT144 between December 2020 to December 2022. (a) Positive velocity is the movement towards the satellite, negative velocity is the movement away from the satellite. Beach ball solution of the 2021 Mw 6.0 earthquake. (b) The creep rate across the profile AA' and the black dashed line shows the Harnai fault. (c and d) Pre-seismic, post-seismic, and co-seismic displacement of the Mw 6.0 2021 Harnai earthquake on points P1, and P2. The red dots show the interferograms. The green colored line shows the co-seismic movement due to the Mw 6.0 earthquake.

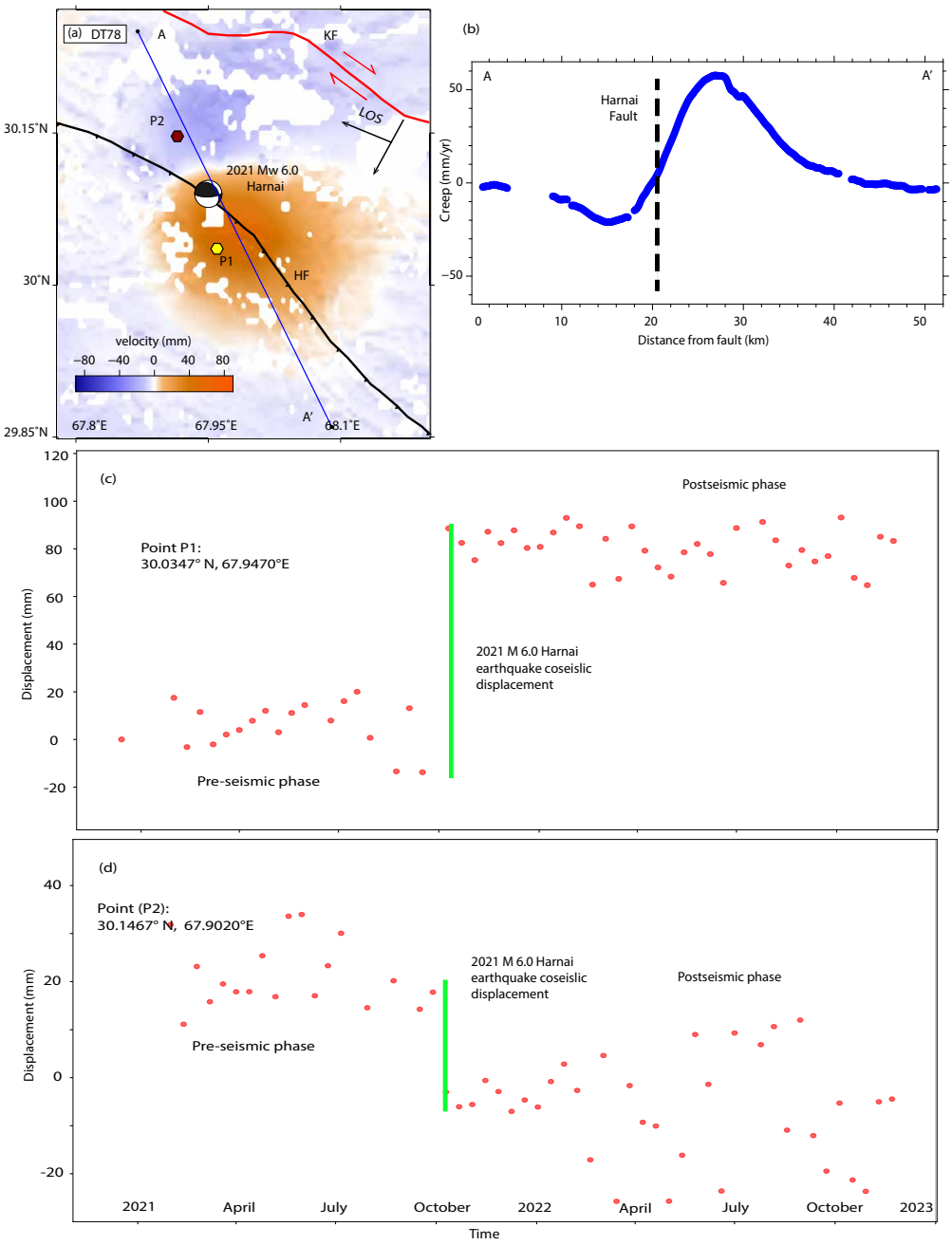

Figure 4.15: Slip rates of descending track DT78 between December 2020 to December 2022. (a) Positive velocity is the movement toward the satellite, negative velocity is the movement away from the satellite. Beach ball solution of the 2021Mw 6.0 earthquake. (b) The creep rate across the profile AA' and the black dashed line shows the Harnai fault. (c and d) Pre-seismic, post-seismic, and co-seismic displacement of the Mw 6.0 2021 Harnai earthquake on points P1, and P2. The red dots show the interferograms. The green colored line shows the co-seismic movement due to the Mw 6.0 earthquake.

4.5 Conclusions

The coseismic surface deformation along the line-of-sight (LOS) is estimated as 70 mm and 80 mm for ascending and descending interferograms, respectively. Modeling of InSAR data reveals primarily thrust-dominated slip in up dip direction with a strike-slip component that is in good agreement with the tectonic context of the transpressional Karahi and Harnai faults. Source fault geometry along with the corresponding uncertainties of the 2021 Mw 6.0 Harnai earthquake and preseismic InSAR analysis shows the fault was locked until 2021 prior to the rupture.

The finite slip shows the 95 % of slip is concentrated between 3 and 10 km depth in both tracks. We find the NW-SE rupture model against the NE-SW model is justified by the tectonic settings and fault structure of the Harnai fault. Major deformation is observed in the hanging wall at the southern block of the Harnai fault. This study helps to understand the crustal deformation mechanism at the western margin of the SFT belt.

5 Insights into the 2023 Earthquake Sequence on the East Anatolian Fault System

Abstract

The East Anatolian Fault (EAF) accommodates the relative motion between the Arabian and Anatolian plates and forms a triple junction at which slip is partitioned among the North Anatolian Fault (NAF), the East Anatolian Fault (EAF), and the faults of the Turkish-Iranian Plateau. The NAF is a 1,200 km long right-lateral strike-slip fault extending from the Karliova triple junction to the Sea of Marmara. The EAF is a 310 km-long left-lateral fault, that extends southwards and branches out diffusely to the Antakya, the Dead Sea Fault (DSF), and the Cyprus Arc to the southwest. The NAF is considered structurally mature while the EAF is structurally immature because it consists of multiple fault segments. These fault segments ruptured over time, and long-term accumulated strain energy is released by bends and step over structures that connect the EAF.

A significant portion of the EAF system is ruptured in the last few years, as demonstrated by the recent activity starting with the January 24, 2020, Mw 6.8 Elazığ earthquake, near Hazir Lake, continuing with the February 06, 2023, Mw 7.8 Kahramanmaraş earthquake that ruptured the 310 km long Erkenek, Pazarcik, and Amanos contiguous fault segments. On the same day 9 hours later, the Mw 7.6 earthquake ruptured the 150 km long E-W trending left lateral splay of the EAF. Two weeks later on February 20, another aftershock with Mw 6.4 occurred in Antakya at the southern termination of the EAF. In this study, we constrained the coseismic slip distribution of the 2023 Mw 7.8 Kahramanmaraş, the Mw 7.6 Elbistan, and Mw 6.4 Antakya aftershocks. The finite fault rupture inversions that I accomplished in this Ph.D study are part of an international effort to collect multi-parametric spaceborne satellite observations to constrain the spatial distribution of the coseismic slip for the entire 2023 earthquake sequence.

Based on the estimated coseismic slip distribution, the 2023 mainshock rup-

ture propagated bilaterally from the central Pazarcik segment. To the north, the rupture terminated near the bifurcation with the Bitlis-Zagros fold-and-thrust-belt. As a result, a 40 km long segment separating the 2020 Elazığ and the 2023 Kahramanmaraş ruptures did not slip during an earthquake. The EAF features creeping segments to the north, near the Karliova triple junction, and around Hazir Lake in the Palu and Pütürge segments, but is locked during the interseismic cycle in the remaining segments. We speculate that this section of the EAF represents a potential seismic gap. Alarmingly, the Pütürge segment remains unbroken, bearing the potential for another Mw 6.8 earthquake. To test this hypothesis, we further investigate the fault behavior before the 2023 Kahramanmaraş sequence. We perform time series analysis using Sentinel-1 SAR interferometry to identify the extent of creep along the EAF, particularly along the 40 km long Pütürge segment. We process the ascending tracks AT116, and AT43, along with the descending tracks DT123 and DT21 using the small baseline (SBAS) inversion algorithm. We use 147 interferograms for track AT116, 85 for track AT43, 120 for track DT123, and 145 for track DT21. As a preliminary step, we stack the geocoded unwrapped interferograms and remove the unwrap errors for each interferogram. We then utilize the ECMWF ERA5 products to reduce the tropospheric phase delays. Finally, we correct the phase ramps, and topographic errors, and estimate the average velocity. Our results indicate the presence of up to 20 mm/yr shallow creep along the EAF after the coseismic deformation of the 2020 Elazığ earthquake, which propagates towards the southwestern end of the Pütürge segment. We also find a creep at many small segments of the EAF zone from Pütürge segment to the Karliova triple junction. This study clarifies the seismic potential of the Pütürge segment.

The first part of the work, concerning the slip distribution of the entire 2023 earthquake sequence on the EAF has been published in (Barbot et al., 2023), and here some text and figures from the publication are reproduced, whereas the work on the creep rates analysis is being prepared for publication.

5.1 Introduction

The Mediterranean Basin, tectonically one of the most active regions located within the western zone of the Alpine-Himalayan seismic belt, traces its origins to the Tethys Sea closure (Bozkurt, 2001; Jackson and McKenzie, 1984; Taymaz et al., 1991). The eastern Mediterranean region is considered as the Europe's most seismically active area due to the rapid interactions of microplates (Malinverno and Ryan, 1986; Nocquet, 2012; Le-Pichon and Kreemer, 2010). Interactions of tectonic processes, including the encroachment of the Arabian Plate towards the Anatolian plate, slab rollback at the Hellenic Trench, and expansion of

the Aegean Sea induce a large-scale rotation, facilitated by major transform faults (Barbot and Weiss, 2021; Barbot et al., 2023; L. Jolivet et al., 2013). The northward interaction of the Arabian Plate triggers a triple junction, where displacement is distributed among the NAF, EAF, and multiple faults in the Iranian-Turkish plateau (Hamiel and Fialko, 2007; Reilinger et al., 2006; Vernant et al., 2004) (Figure 5.1). The NAF, a mature, 1200 km long right lateral fault system, extends from the Karliova triple junction to the Marmara Sea (Ambraseys, 1970; Güvercin et al., 2022; Hubert-Ferrari et al., 2002; Le-Pichon et al., 2016). The conjugate EAF, a 300 km long sinistral fault system, extends southwards and branches out diffusely towards Antakya, the Cyprus Arc, and the Dead Sea Fault (DSF) (Garfunkel et al., 1981). The left lateral EAF system connects multiple fault segments with a relatively lower long-term slip rates (Aktug et al., 2016; Cavalié and Jónsson, 2014), exhibiting major releasing bends and step-overs (Duman and Emre, 2013; Güvercin et al., 2022), making it relatively immature in comparison to the NAF system (Figure 5.1). Farther south, the left lateral DSF system serves as the boundary fault and accommodates the Arabian Plate movement in the north (Garfunkel et al., 1981).

The dynamic interplay of these tectonic plates is regulated by the frictional resistance of faults within the brittle Earth's crust, leading to recurring seismic cycles. The NAF experienced a prolonged sequence of earthquakes throughout the 20th century, commencing with the Erzincan earthquake in 1939 with Mw 7.9 (Emre et al., 2021), the 1999 Mw 7.9 Izmit (Hamiel and Fialko, 2007), the 1999 Mw 7.4 Düzce earthquake (Ergintav et al., 2009; Hearn et al., 2002) near Istanbul. The northern EAF also experienced several earthquakes in the last century, mostly ruptured as left lateral slip with the Mw 6.8 in 2020, Mw 6.1 in 2010, Mw 6.7 in 1971, and Mw 6.8 in 1905. However, the southern section of the Elazığ segment has not been ruptured in the previous century (Barbot et al., 2023; Duman and Emre, 2013; Hubert-Ferrari et al., 2020). Southern EAF experienced several notable earthquakes with Mw 7.2 in 1893, Mw 7.0 in 1795, and Mw 6.9 in 1114 (Güvercin et al., 2022). Hence, most of the southern segments of the left lateral EAF system remain locked and accumulate stress before the 2020 Mw 6.8 earthquake at the northern section of the Elazığ, the 2023 Mw 7.8 Kahramanmaraş and the Mw 7.6 Elbistan earthquake sequence (Barbot et al., 2023; Pousse-Beltran et al., 2020).

On February 6, 2023, Turkey and Syria were shaken by powerful earthquakes that caused tremendous damage and loss of lives (Figure 5.1, and 5.2). Earthquakes in this region occur naturally due to the long-term motion of tectonic plates around the Mediterranean Basin. To better understand the circumstances of these tragic events, we analyze remote sensing data that measures the ground displacement caused by these earthquakes.

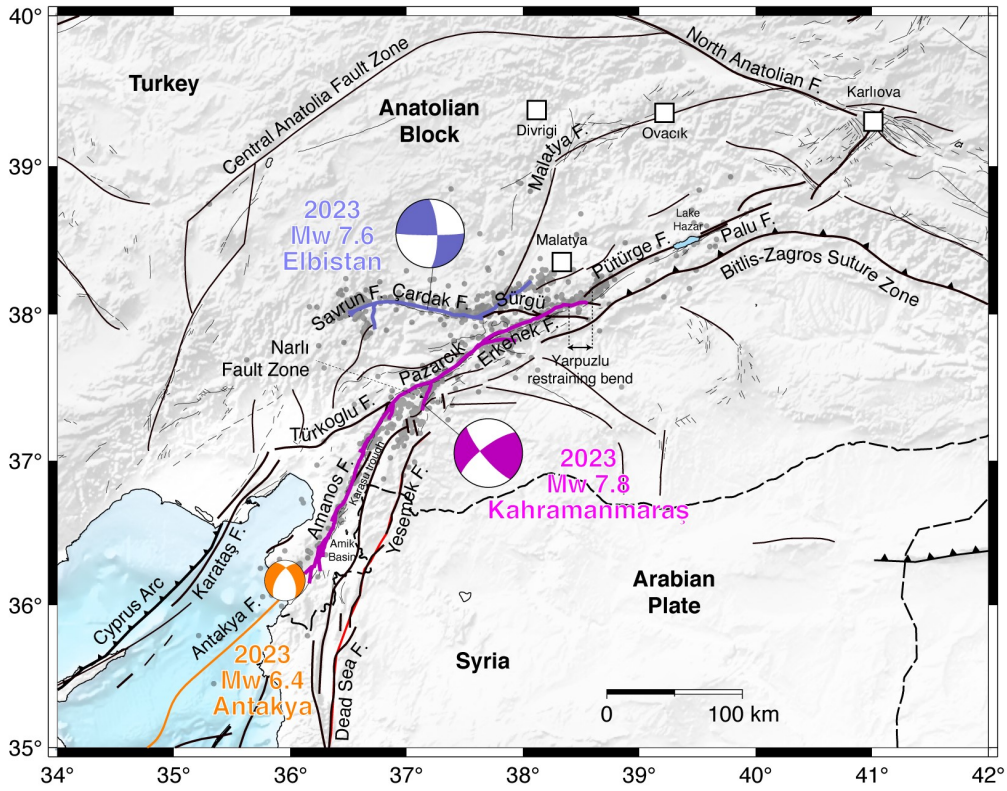

Figure 5.1: Simplified tectonic map of the East Anatolian Fault Zone after Duman and Emre, 2013 and Emre et al., 2018. The East Anatolian Fault consists of a succession of discontinuous segments. The 2023 Mw 7.8 mainshock ruptured the Amanos, Pazarcık, and Erkenek segments and stopped at the Yarpuzlu restraining bend. The Mw 7.6 aftershock ruptured the Savrun Fault, the Çardak Fault, and propagated toward Malataya along a structure between the Sürgü Fault and the Malatya Fault. Fault is abbreviated to "F." to save space. The February 20, 2023 Mw 6.4 aftershock took place near the Antakya Fault towards the Mediterranean Basin. The background seismicity also mentioned in (Figure 5.2b) represents the aftershocks within 2 days of the mainshock (Lomax, 2023).

5.2 Recent Seismicity on the EAF System

The complicated tectonic settings of the EAF system have produced numerous large earthquakes as explained in Section 5.1. However, in this study we will focus on some recent major earthquakes that struck north of the Pütürge segment in 2020 with Mw 6.8, and the 2023 earthquake sequence with Mw 7.8, Mw 7.6 and Mw 6.4 that ruptured the major parts of the EAF system from the Erkenek segment to Antakya (Barbot et al., 2023; Ragon et al., 2021) (Figure 5.2).

5.2.1 The 2023 Kahramanmaraş, and Elbistan Earthquake Sequences

On February 6, 2023, the Kahramanmaraş earthquake, the most significant seismic event to strike Turkey since 1939, ruptured the South-West trending segments of the EAF system continuously (Figure 5.2). This destructive mainshock initiated a long sequence of aftershocks. On the same day 9 hours later, another Mw 7.6 destructive earthquake ruptured the 150 km long east-west trending Çardak fault, a left lateral splay of the EAF system near Elbistan (Figure 5.2).

This complicated sequence of large earthquakes, occurring on nearby faults within hours, is considered an unprecedented phenomenon in a continental setting, particularly considering their similar source mechanisms (Figure 5.2). The mainshock and its major aftershocks produced widespread destruction and severe damage to an estimated 160,000 buildings and claimed over 50,000 lives. The long sequence of aftershocks along the EAF system disturbed an additional 200,000 people and affected around 14 million people across Turkey and Syria.

We find that the mainshock produced up to 8 m of slip on the EAF connecting segments that historically ruptured individually in different times. The Mw 7.6 aftershock produced more slip at depth, up to 12 m, on a separate fault. The coseismic slip for both earthquakes also correlates with the GPS measurements (Barbot et al., 2023). The coseismic slip of these earthquakes illuminates some important characteristics of the brittle crust in the EAF zone. Along the EAF, the slip distribution is characterized by a shallow slip deficit, a maximum coseismic slip of 8 m between 3 and 7 km depth, and a bottom depth of 18 km depth — presumably including much afterslip. Along the strike direction, coseismic slip is maximum at the central segments and tapers at the segment boundaries. The small-magnitude aftershocks cluster at the segment boundaries and the regions of high coseismic slip. Along the Çardak fault, the coseismic slip of the Mw 7.6 aftershock is relatively uniform with 11 m from the surface to 7 km depth, vanishing at 12 km depth (Barbot et al., 2023).

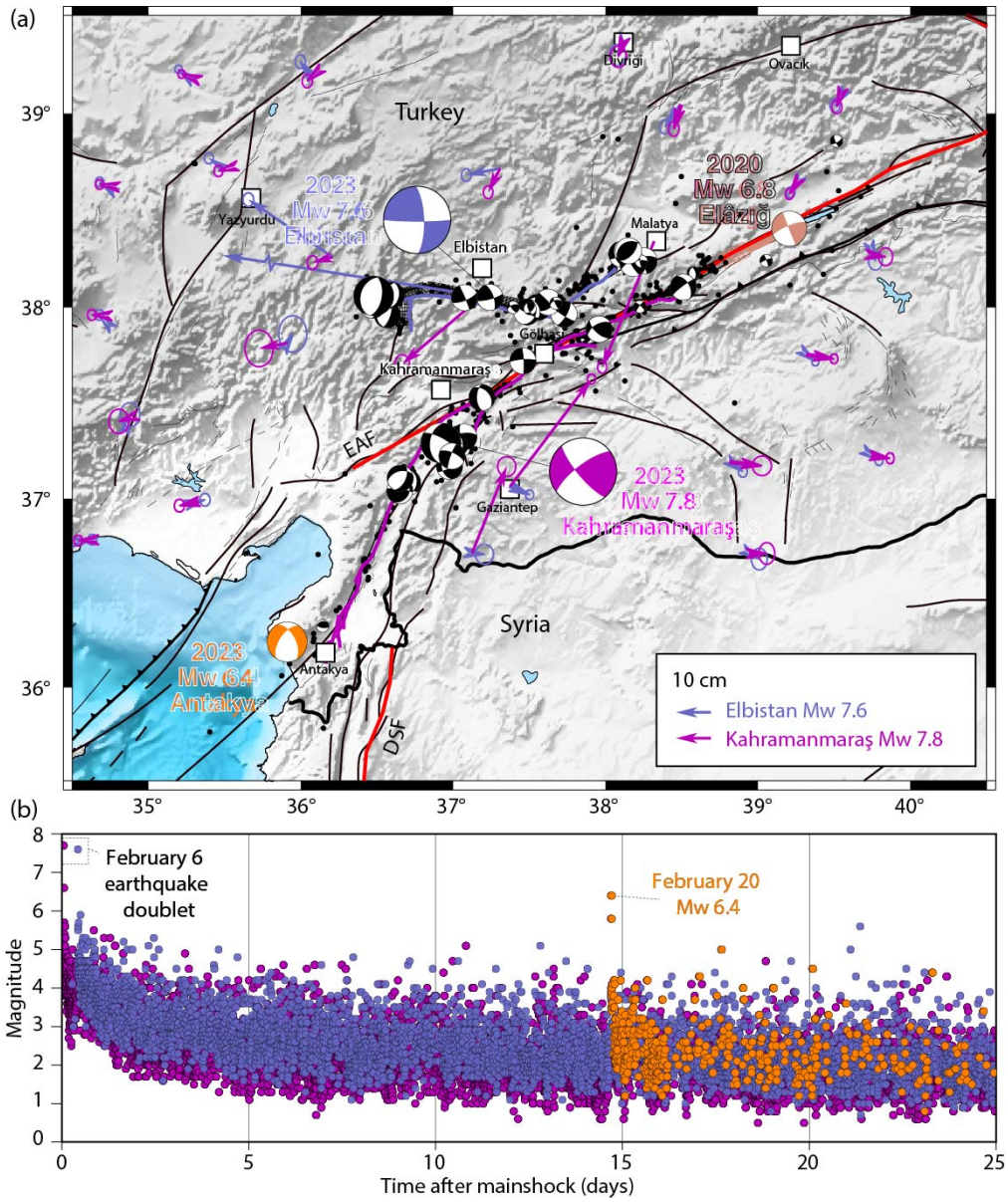

Figure 5.2: Tectonic setting and crustal deformation of the East Anatolian Fault (EAF) on February 6, 2023. a) The aftershocks (black dots) (Lomax, 2023) and the focal mechanisms of earthquakes of moment magnitude greater than 4 (beach balls) illuminate the ruptures of the Kahramanmaraş Mw 7.8 (purple) and the Elbistan Mw 7.6 (blue) earthquakes. The fault offsets indicate the extent of the ruptures. The EAF and Dead Sea (DSF), plate-boundary faults, are shown in red. Major and minor faults are shown in thick and thin black lines, respectively (Emre et al., 2018). The focal mechanisms are from the Disaster and Emergency Management Authority (AFAD) for February 6, 2023 (`https://deprem.afad.gov.tr/event-catalog`). The topography is from the Global Multi-Resolution Topography Synthesis (GMRT) (Ryan et al., 2009). b) Time series of aftershocks magnitude in the days following the mainshock (purple for aftershocks within 20 km of the EAF, blueish for aftershocks within 20 km of the Mw 7.6 rupture, and orange for earthquakes within 20 km of the Mw 6.4 Antakya aftershock). The February 20, 2023 Mw 6.4 aftershock occurs at the southern termination of the EAF.

5.2.2 The 2023 Antakya Aftershock

Just two weeks after the powerful 06 February 2023 earthquake sequence, a Mw 6.4 aftershock struck southeast Turkey on 20 February 2023 near Antakya (Figure 5.2). The earthquake occurred on a left lateral strike-slip fault where the EAF bifurcates offshore towards the Cyprus arc. The 20 February 2023 earthquake is considered a standout event of the aftershock sequence of the Mw 7.8 Kahramanmaraş rupture. The magnitude of Antakya aftershock (Mw 6.4) is significantly smaller than the mainshock with Mw 7.8, but it is still powerful enough to cause widespread damage in Antakya and surrounding areas. The aftershock indicates complex tectonic settings and stress transfer from continental settings to offshore. The Antakya fault ruptured previously in 1872 with Mw 7.2 claiming thousands of lives and widespread damage (Mai et al., 2023).

The Antakya aftershock was followed by numerous notable aftershocks in the Mediterranean Sea, showing the fault remained stressed and can still produce numerous aftershocks. The epicenter of the 20 February 2023 Mw 6.4 aftershock was closer to a densely populated city with a rich cultural heritage, causing extensive damage to infrastructure and buildings. The aftershock also triggered landslides and rockfalls, further disrupting the already damaged area caused by the Kahramanmaraş earthquake. Here, the Antakya aftershock provides us an opportunity to understand the rupture propagation and tapering off the ongoing seismicity on the EAF system. Understanding the geological setting, rupture termination of major earthquakes, and fault behavior in the region is crucial for earthquake preparedness and risk mitigation.

5.2.3 The 2020 Elazığ Earthquake

On January 24, 2020, the Mw 6.8 Elazığ earthquake occurred on the EAF system (Figure 5.2). It was one of the largest earthquakes of the last century on the EAF system prior to February 6, 2023, Mw 7.8, and Mw 7.6 devastating doublet earthquakes separated by 9 hours. The 2020 Elazığ earthquake originated near Lake Hazir and propagated southward until the Pütürge segment of the EAF system. The Pütürge segment remains locked during the coseismic rupture of the 2020 Elazığ earthquake (Konca et al., 2021; Pousse-Beltran et al., 2020; Ragon et al., 2021). It is to be noted that the 2023 Mw 7.8 Kahramanmaraş mainshock occurred on the EAF, propagated south- and north-ward bilaterally, and tapered off at the southern boundary of Pütürge segment.

5.3 Methodology used for studying the Antakya Aftershock

In this section, we will discuss the methodology applied in obtaining the coseismic deformation of the Antakya aftershock and the slip distribution for the 2023 Kahramanmaraş, Elbistan, and Antakya earthquake sequence.

5.3.1 Analysis of Antakya Aftershock

For the 2023 Mw 7.8 Kahramanmaraş, and Mw 7.6 Elbistan earthquakes different spaceborne geodetic observations were used to constrain the slip distribution to address first-order questions regarding the mechanisms of rupture propagation and arrest in the EAF system. In this section, we focus on the February 20, Mw 6.4 Antakya earthquake and the transition between the EAF and Antakya Fault that propagates into the Mediterranean Basin (Figure 5.1). For the Mw 6.4 Antakya aftershock, we make use of the great sensitivity of the Sentinel-1 SAR phase and constrain the slip distribution with the inversion of the Sentinel-1 interferograms. Below, we describe the data processing to constrain crustal deformation.

5.3.1.1 InSAR Data Processing

For the February 20, 2023 Mw 6.4 aftershock near Antakya, we use the interferogram based on SAR images acquired on February 9, 2023, and February 21, 2023, along the ascending track 14 (AT14) and the interferogram based on SAR images acquired on February 10, 2023, and February 22, 2023, on descending track 21 (DT21). With these acquisition dates, the observed deformation includes also the local Mw 5.5 aftershock. The features of the Sentinel-1 used in this study are given in Table 5.1. We mostly followed the procedure explained in Chapter 3 and Chapter 4 to process the SAR data for both ascending and descending track interferograms, with some differences. We produce the interferograms through the LicSBAS platform (Lazeckỳ et al., 2020; Morishita et al., 2020) and correct for atmospheric perturbations using the GPS-based iterative tropospheric decomposition GACOS model (Yu et al., 2018b). We apply the topographic phase correction included in LiCSBAS, which uses the digital elevation model from the SRTM (Farr et al., 2007).

Sometimes the deformation associated with large-magnitude earthquakes has a large deformation gradient that produces dense fringes in the InSAR interferogram which are difficult to unwrap reliably. Therefore, pixel-offset tracking methods are useful, in which cross-correlation of the Sentinel-1 SAR reflectivity amplitude, is used to estimate the coseismic surface deformation (Barbot et al.,

2023; T. Wang et al., 2014; 2018). Unlike the 2023 Mw 7.8 Kahramanmaraş, and Mw 7.6 Elbistan earthquakes, for the Antakya earthquake we were able to use phase information of the backscattered signal of the Sentinel-1 SAR data. Therefore, we unwrap the phase interferograms with the Statistical-cost, Network-flow Algorithms (C. Chen and Zebker, 2002). The unwrapped interferograms of both ascending and descending tracks are shown in Figure 5.3a, b, revealing crustal deformation to the southwest of the Mw 7.8 mainshock rupture, indicating the propagation of seismic unrest toward the Cyprus Arc, compatible with the distribution of aftershocks (Figures 5.2).

Table 5.1: Features of Sentinel-1A data used for estimating the deformation produced by Antakya aftershock

Duration (yy/mm/dd)	Track no.	Perp. baseline (m)	Inc. angle (°)	Head. platform (°)
2023/02/09–2023/02/21	*DES.T*021	15	38 – 41	168 – 170
2023/02/10–2023/02/22	*ASC.T*14	20	38 – 41	−9.7 – −11.2

5.3.1.2 Geodetic Bayesian Inversion of Antakya Aftershock

Before running the Bayesian inversion, we estimate the variance and covariance of the datasets to determine the errors, produced by phase decorrelation due to uneven distribution of water vapor content in the troposphere and turbulence of ions in the ionosphere (Hanssen et al., 1999). In addition, it can also be due to steep topographic variations in which case it correlates with the topography, named as stratified atmospheric noise (Knospe and S. Jonsson, 2009). Presumably, ionosphere structures are considered coherent over a scale of hundreds of kilometers, especially for C-band SAR satellites. However, water vapor content varies unevenly with topography which can introduce delays in LOS direction (Emardson et al., 2003; P. Jonsson and Eklundh, 2002). Therefore, we estimate the spatial variability of both ascending and descending interferograms using a semi-variogram (Wackernagel, 2003) by measuring the dissimilarity among the processed interferogram. We perform the semi-variogram analysis over a region, ten times larger than the area that is subjected to surface deformation and calculate the range, sill, and nugget values for the ascending and descending interferograms separately (Table 5.2).

We estimate the Antakya aftershock ruptured fault geometry, in terms of fault dip, strike, length, width, slip, and depth by inverting ascending and descending LOS surface displacements (Figure 5.3a, b) through the Bayesian

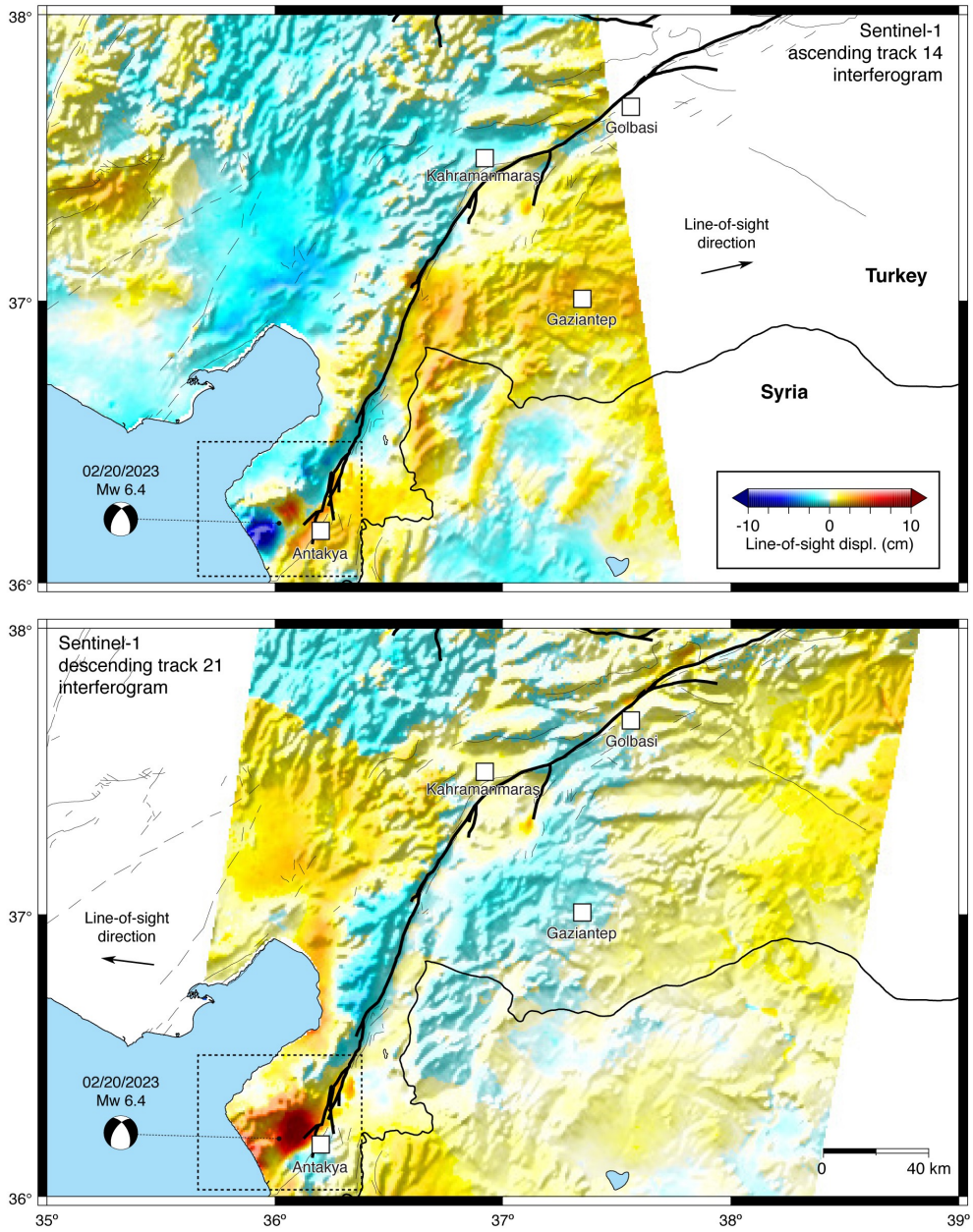

Figure 5.3: Sentinel-1 unwrapped interferograms of the February 20, 2023 Mw 6.4 aftershock near Antakya, Turkey. a) Interferogram of ascending track AT14, based on SAR images acquired on February 9, 2023 and February 21 2023. b) Interferogram of descending track DT21 based on SAR images acquired on February 10, 2023 and February 22, 2023. The dashed rectangle indicates the region most affected by crustal deformation.

Table 5.2: Detail of ascending descending interferograms dataset errors calculated in terms of LOS displacement of Antakya aftershock using semi-variogram

Track	Sill $(mm)^2$	Nugget $(mm)^2$	Range (km)	Threshold $(mm)^2$	Subsample (points)
$DES-T021$	0.16	2.44×10^{-18}	9.80	1×10^{-4}	388
$ASC-T14$	0.19	1.08×10^{-06}	13.2	1.4×10^{-2}	126

inversion (GBIS) approach (Bagnardi and Hooper, 2018; Javed et al., 2022). After estimating the semi-variogram parameters, we subsample the datasets to reduce the computational cost and obtain enough samples that accurately depict the true surface displacement. We subsample the full-resolution ascending track interferogram (number of subsamples in the AT14: 126) and descending track interferogram (number of subsamples in the DT021: 388) (Figure 5.4a, b) using a quadtree gradient-based approach (Simons et al., 2002). It recursively divides the surface deformation into further four polygons unless we achieve the threshold variance for ascending ($1.4 \times 10^{-2} mm^2$) and descending ($1 \times 10^{-4} mm^2$) interferograms as given in Table 5.2.

We examine the southern termination of the Mw 7.8 Kahramanmaraş earthquake sequence at Antakya with Mw 6.4. We generate a synthetic model in a homogeneous elastic half-space based on a uniform rectangular dislocation model (Okada, 1992). The Okada model has been proven effective in simulating coseismic deformation caused by earthquakes (Barbot et al., 2023; Barkat et al., 2022; Garthwaite et al., 2013; Javed et al., 2022; H. Wang et al., 2017; W. Xu et al., 2018). The ascending and descending interferograms show surface deformation of approximately -10 cm and 10 cm along their respective LOS direction (Figure 5.3). We efficiently categorize the posterior probability density (PDF) of the ruptured fault geometry of the Antakya aftershock with automatic step size using the Metropolis-Hastings algorithm and the Monte Carlo Markov chain method (Hastings, 1970; Metropolis et al., 1953; Tarantola, 2005). We use 10^6 iterations to define posterior PDF, discarding the first 20,000 samples (Figure 5.5).

We find the strike of rupture 237° ± 5 from the north with a dip angle of 55° ± 5. The fault orientation falls within the large cloud of aftershock hypocenters and aligns well with the Antakya Fault that runs toward the Cyprus Arc. The posterior probability distribution of each source fault model is shown in Figure 5.5. Histograms of ruptured fault model parameters are generated during the Bayesian inversion with 10^6 iterations. The y-axis shows the probability density based on 10^6 iterations with 95% confidence interval. To evaluate the quality of inversions, we find each rupture parameter converges very well around the average and optimal value of the model. (Figure 5.6).

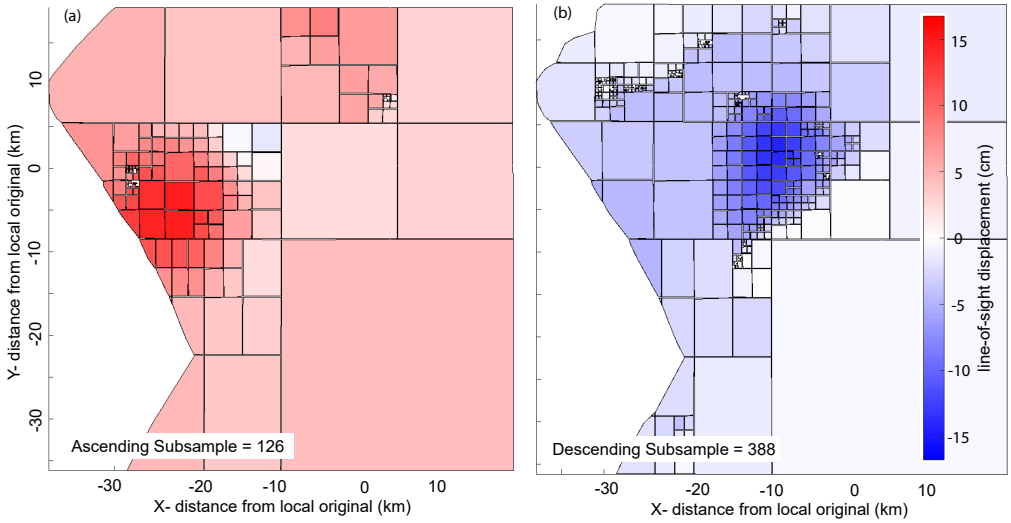

Figure 5.4: Subsampling of ascending (AT014) and descending (DT021) tracks interferograms before inverting LOS displacement.

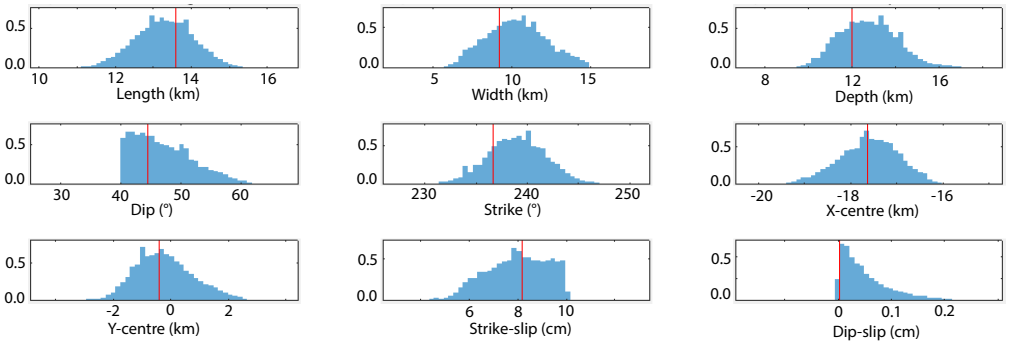

Figure 5.5: Histograms of ruptured fault model parameters through Bayesian inversion approach with 10^6 samples. The y-axis represents the probability density, and the red line indicates the optimal model values with 95% confidence interval

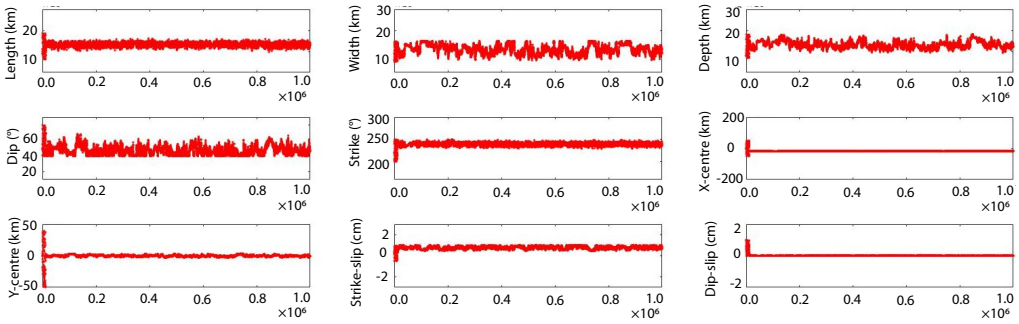

Figure 5.6: Convergence of ruptured fault model parameters through Bayesian inversion approach with 10^6 samples. The y-axis represents the range of fault parameters, while the x-axis shows the number of samples used in the inversions.

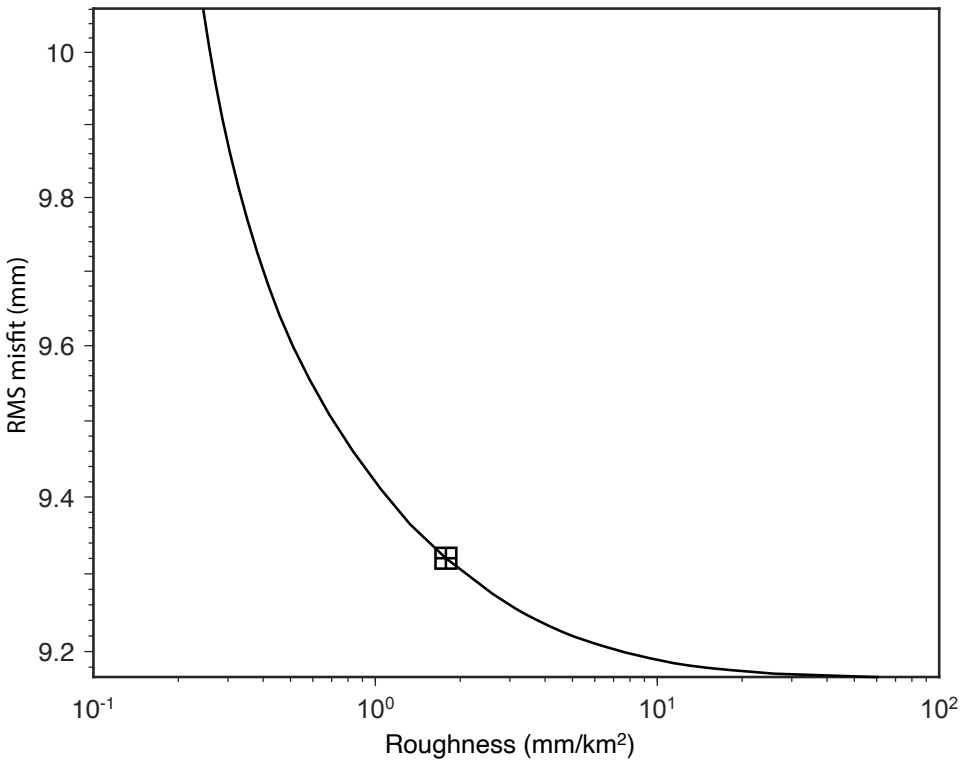

Figure 5.7: Trade-off between roughness and residuals for the Mw 6.4 Antakya aftershock.

5.3.1.3 Slip Distribution of the 2023 Earthquake Sequences

For the slip distribution of the 20 February 2023 Antakya aftershock, we use the inferred geometry, and invert for a finite slip distribution applying a non-negative least square inversion (Jónsson et al., 2002), with a discretization of the fault into $1 \times 1\,km^2$ patches. The comparison between the Sentinel-1 observations for tracks AT14 and DT21 and the forward model for the Mw 6.4 Antakya aftershock is shown in Figure 5.8. We use Green's function relating the fault strike-slip and dip-slip components to surface displacement for an elastic half-space (Okada, 1992). To reduce the number of data points used in finite-source modeling, we downsample the observations using a quadtree (Fialko, 2004b; Jónsson et al., 2002). We invert for the slip distribution using regularized least-squares by imposing a smooth distribution of slip enforced by a Laplacian operator (Huiskamp, 1991). We use the L-curve (Aster et al., 2012) to resolve the trade-off between misfit and roughness and estimate the optimal smoothing constraints (Aster et al., 2012) (Figure 5.7). Slip is allowed to have along-strike and down-dip components. The data used for the inversion are defined by the dashed frame in Figure 5.3. We use the ascending and descending interferograms jointly to constrain the slip distribution.

The slip distributions Mw 6.4 Antakya aftershock along with the Mw 7.8 Kahramanmaraş, and the Mw 7.6 Elbistan, and are shown in Figure 5.9. The coseismic slip for Kahramanmaraş mainshock is maximum between 3 and 7 km depth, tapering off between 8 and 14 km depth. Fault slip is mostly left-lateral with small changes of dip near the surface (Figure 5.9). For the Mw 6.4 Antakya aftershock, the rupture extends along strike over a length of 25 km, and a downdip distance of 25 km. The maximum slip of 0.93 m occurs at a depth of 8.3 km, with a rake of -12°, corresponding to dominantly left-lateral slip, with the area affected by greater slip extending down-dip towards the northeast (Figure 5.9)

On February 6, 2023, the Mw 7.8 mainshock initiated on the Narlı Fault zone that bounds the Narlı basin, north of the Karasu trough (Figure 5.9). The rupture continued along the EAF, propagating bilaterally into the Amanos segment to the south and into the Pazarcık and Erkenek segments to the north (Melgar et al., 2023). The surface rupture stopped just northeast of the Yarpuzlu restraining bend (Figure 5.9). There is no visible surface break along the Pütürge segment even though aftershocks extend to the southern limit of the January 24, 2020, Mw 6.8 Elazığ rupture.

The 06 February 2023 Mw 7.6 aftershock nucleated in the middle of the Çardak Fault and propagated westward to the Savrun Fault and eastward across the so-called Nurhak complexity (Duman and Emre, 2013) along an immature fault between the Malatya and the Sürgu faults (Melgar et al., 2023) (Figure 5.9).

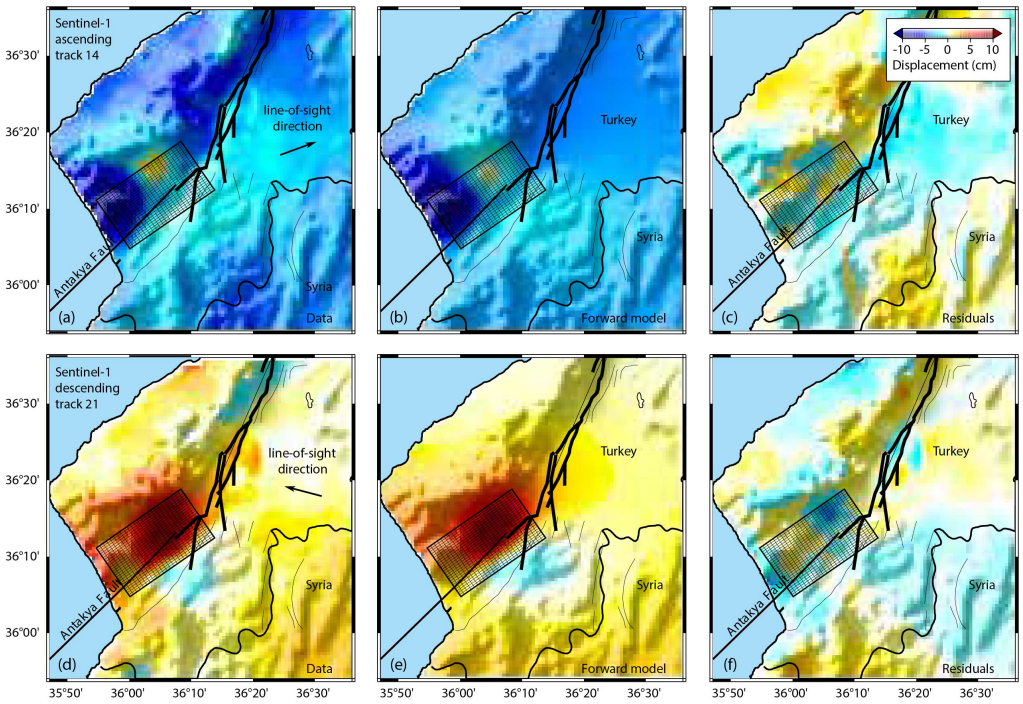

Figure 5.8: Comparison between Sentinel-1 interferogram and the deformation predicted by the slip distribution of the Mw 6.4 Antakya aftershock. a, b, c) Data, forward model, and residuals for the ascending track 14 interferogram. d, e, f) Same for the descending track 21 interferogram. The line-of-sight direction is indicated by the black arrow. The fault geometry (black patches) is broadly aligned with the Antakya Fault.

The Mw 7.6 aftershock triggered a sequence of additional aftershocks including normal faulting earthquakes near the Savrun Fault (Figure 5.2). The aftershocks cluster north of the Çardak Fault, indicating a north dipping fault. There is no indication of slip on the Sürgu fault connecting the Çardak fault to the EAF. The Mw 7.8 mainshock and the Mw 7.6 aftershock occurred on disconnected faults. The long streak of seismicity east of the Karasu trough and south of the Narlı Basin is not associated with detectable surface displacements.

The rupture of the Mw 7.6 aftershock is more compact, mostly confined to the Çardak fault with a maximum slip of 11 m from the surface to 7 km depth. The slip tapers off from 8 to 12 km, shallower than along the EAF (Figure 5.9). Slip along the northeast-striking Gök Hill and Söğüt segments between the Malatya and Sürgü faults is limited to at most 5 m. Slip on the south-striking Yeşilköy normal fault reaches 2 m (Figure 5.9).

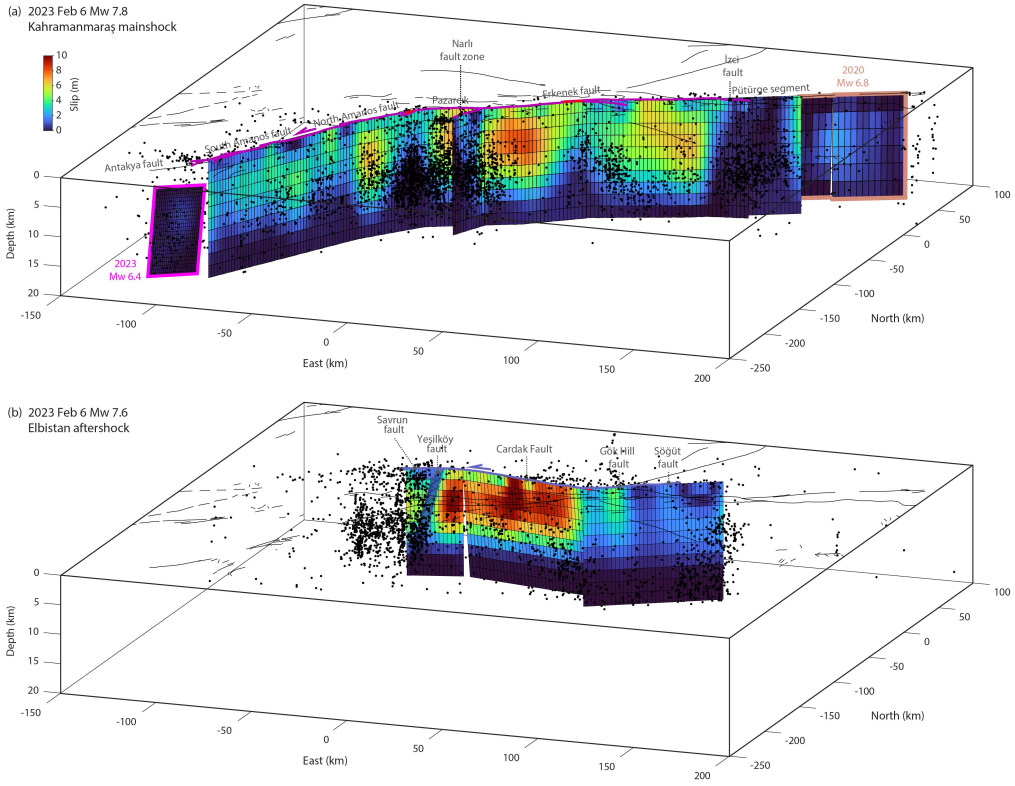

Figure 5.9: Coseismic slip distribution of a) the 2023 February 06, Mw 7.8 Kahramanmaraş mainshock, the February 20, Mw 6.4 aftershocks (purple), and the 2020 Mw 6.8 Elazığ earthquake (Pousse-Beltran et al., 2020) (light brown) and b) the 2023 February 6, Mw 7.6 Elbistan aftershock. The maximum slip of 8 m on the EAF concentrates between 3 and 7 km depth, highlighting a shallow slip deficit. The maximum slip on the Çardak fault during the Mw 7.6 aftershock is 11 m from the surface to 7 km depth. The small-magnitude aftershocks (Lomax, 2023) concentrate at segment boundaries and around the regions of high coseismic slip.

5.4 Fault Creep at Pütürge Segment Prior to the 2023 Earthquake Sequences

On January 24, 2020, the Mw 6.8 Elazığ earthquake occurred on the EAF system at the indentation zone of the Arabian plate towards the Anatolian plate. It was one of the largest earthquakes of the last century on the EAF system before the February 6, 2023, Mw 7.8, and Mw 7.6 devastating earthquakes doublet. The 2023 Mw 7.8 Kahramanmaraş mainshock occurred on the EAF and propagated south- and north-ward tapered off at the southern boundary of Pütürge segment. While the 2020 Mw 6.8 Elazığ earthquake originated near Lake Hazir and propagated southward until the Pütürge segment along the EAF. The Pütürge segment remains locked during both the 2020 and the 2023 mainshocks (Figures 5.10b). In this study, we use spaceborne Sentinel-1 observations to perform time series analysis to address the concern of a potential seismic gap at the Pütürge segment of the EAF zone between the Mw 6.8 2020 Elazığ earthquake and the Mw 7.8 2023 Kahramanmaraş earthquake (Figures 5.10b).

5.4.1 Coseismic Rupture of the 2020 Mw 6.8 Elazığ Earthquake

The geological studies on the EAF system at the convergence zone of the Anatolian-Arabian plates suggest approximately 25 km offset along the fault (Duman and Emre, 2013). Unlike the NAF, which experienced a significantly larger number of moderate to major earthquakes in the last century, the EAF had remained largely silent since the 19^{th} century (Duman and Emre, 2013). In 2020 the Elazığ earthquake ruptured nearly half of the Pütürge segment along the EAF, causing widespread damage, especially in the city of Elazığ, and took 41 lives and injured hundreds of people due to the collapse of poorly constructed buildings (Cakir et al., 2023; Pousse-Beltran et al., 2020; Tatar et al., 2020).

The 2020 Mw 6.8 Elazığ earthquake originated near an abrupt, approximately 10° bend along the surface trace of the Pürtürge segment of the EAF system. It was preceded by two moderate foreshocks occurring within a short distance of around 5 km on April 4 and December 27, 2019. The Elazığ rupture propagated in East-North direction and may have extended into the rupture zone of the 1874 Mw 7.1 Gölcük Gölu earthquake before halting at the Lake Hazar basin, a region previously identified as a significant EAF segment boundary (Pousse-Beltran et al., 2020).

SAR interferometry has shown a broader deformation across the fault than field observations and a lack of substantial coseismic surface rupture (Cakir et al., 2023; Konca et al., 2021; Pousse-Beltran et al., 2020; Ragon et al., 2021).

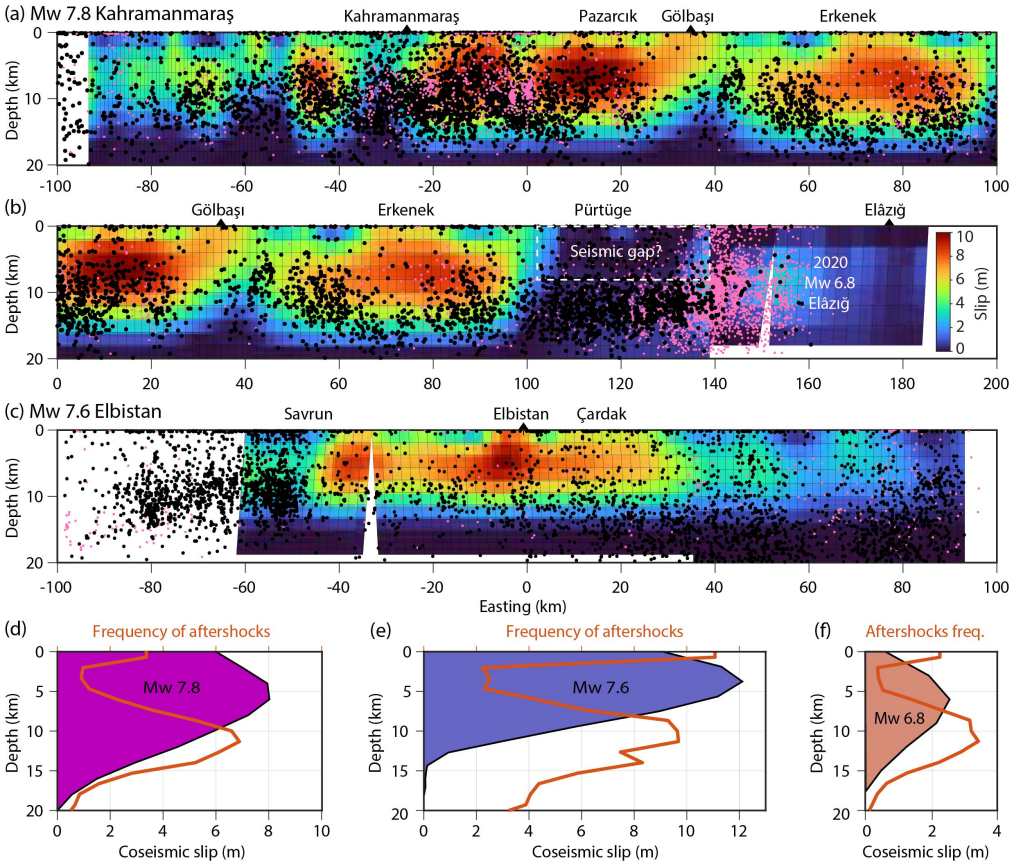

Figure 5.10: Shallow slip deficit and potential seismic gap along the Pütürge segment. a) Coseismic slip distribution of the 2023 February 6, Mw 7.8 Kahramanmaraş mainshock with peak slip between 6 and 8 km depth. b) Coseismic slip distribution of the Mw 7.8 mainshock in relation to the 2020 Mw 6.8 Elazığ earthquake (Pousse-Beltran et al., 2020), highlighting a potential 40 km-long seismic gap in the Pütürge segment. c) Coseismic slip distribution of the 2023 February 6 Mw 7.6 Elbistan aftershock. The aftershocks distribution and the background microseismicity before the respective earthquakes are shown with black and purple dots, respectively. d) Depth distribution of coseismic slip and aftershocks for the Mw 7.8 mainshock, highlighting a shallow slip deficit. The aftershocks concentrate in regions of high gradient of slip. e) Same for the Mw 7.6 aftershock. f) Same for the 2020 Mw 6.8 Elazığ earthquake and its aftershocks.

InSAR and seismological data analysis indicate a roughly 40 km long subsurface rupture between Elazığ and Pütürge segments along the EAF system. The earthquake nucleated at 12 km depth and propagated upwards mostly southwestward. The rupture was not exposed on the surface and terminated a few kilometers below the surface (Pousse-Beltran et al., 2020; Taymaz et al., 2021). Field observations and geodesy indicate discontinuities in deforming surface were majorly observed within a 300 m wide and 30 km long fault due to Elazığ earthquake. However, interferometry data indicates a broader deformation zone width of approximately 1 km (Tatar et al., 2020).

There are several geological and geophysical explanations for the lack of surface surface rupture. Some authors suggest the rupture arrested at the shallow depth due to a slip deficit (Cakir et al., 2023). Some authors proposed several explanations for the observed slip deficit, including the relatively immature EAF system (Pousse-Beltran et al., 2020; Taymaz et al., 2021), and absence of substantial stress transfer (Cakir et al., 2023; Konca et al., 2021; Pousse-Beltran et al., 2020; Ragon et al., 2021). Despite the absence of significant strike-slip coseismic displacement along surface ruptures, surprisingly vertical offsets of up to 40 cm were noted particularly in the southwestern part of the ruptured fault in the Pütürge segment (Tatar et al., 2020).

5.4.2 Slip Distribution of the Mw 6.8 Elazığ Earthquake

InSAR and seismological data analysis indicate a roughly 40 km long rupture, nucleated at 12 km depth which propagated upwards predominantly southwestward (Cakir et al., 2023; Pousse-Beltran et al., 2020; Taymaz et al., 2021). The rupture did not emerge to the surface but was obstructed abruptly at shallow depth. We compared the slip distribution of the Mw 6.8 Elazığ earthquake with the 2023 Kahramanmaraş earthquake sequence as shown in Figures 5.9a, and 5.10b.

The rupture propagation exhibited an elongated elliptical pattern with three distinct high-slip lobes, or asperities, situated beneath the fault in a shallow creeping sections (Cakir et al., 2023; Pousse-Beltran et al., 2020; Ragon et al., 2021; Taymaz et al., 2021). Coseismic slip reached a maximum of 3 m at depths of approximately 4 km above the hypocenter, while surface slip near the epicenter was limited to the order of cm (Cakir et al., 2023; Pousse-Beltran et al., 2020). The nucleation point of the earthquake, where the rupture initiated on the subsurface fault, was located at the edge of one of the high-slip lobes. While the maximum slip occurred at shallow depths of 4 - 8 km, coseismic slip diminished rapidly towards the surface, dropping from meters to near zero at depths of $1 - 1.5$ kilometers, leaving the shallowest segment of the fault with apparently negligible slip (Cakir et al., 2023; Pousse-Beltran et al., 2020).

5.4.3 Data and Methodology for SBAS Time Series

In this study, we perform time series analysis using Sentinel-1 SAR interferometry to understand the postseismic movement of the 2020 Mw 6.8 Elazığ earthquake, and analyze the seismic potential of the 40 km long Pütürge segment of the EAF zone. We use two Sentinel-1 ascending tracks AT116, and AT43, and two Sentinel-1 descending tracks DT123, and DT21 to fully cover the central and northern zones of the EAF system. We utilize the Sentinel-1 geocoded unwrapped interferograms from the Advanced Rapid Imaging and Analysis (ARIA) products for tracks AT116, AT43, and DT21 (Buzzanga et al., 2020). In addition, we use unwrapped interferograms of the Looking Inside Continents Space with Synthetic Aperture Radar (LiCSAR) products for the track DT123 (Lazeckỳ et al., 2020). We take advantage of these open source products to assess the kinematic behavior of the EAF system from the Pütürge and Palu segments to the Karliova triple junction point from January 29, 2020, to January 29, 2023, the time interval between the 2020 Elazığ and 2023 Kahramanmaraş earthquake sequence. We perform a time series analysis to calculate the average surface displacement using the SBAS algorithm (Morishita et al., 2020; Yunjun et al., 2019).

For tracks AT116, AT43, and DT21, we use the ARIA platform (Buzzanga et al., 2020), an initiative of the Jet Propulsion Lab (JPL) NASA to monitor floods, earthquakes, and other tectonic deformation processes. The project aims to cover the whole globe, currently concentrated in regions of the United States of America, China, and Turkey. The platform provides products of open-source Sentinel-1 geocoded unwrapped interferograms. The products consist of unwrapped phase, coherence, amplitude, and connected components information of the study area. Furthermore, it allows performing the time series analysis and computing the average velocity through MintPy software (Ghayournajarkar and Fukushima, 2020). We select 147 interferograms for the track AT116 (Figure 5.11), 86 for the track AT43 (Figure 5.12), and 145 for the track DT21 (Figure 5.13) to analyze the fault creep at the Pütürge, and Palu segments of the EAF up to the Karliova triple junction. As a preliminary step, we stack the geocoded unwrapped interferograms and remove the unwrap errors for each interferogram. We then utilize the ECMWF ERA5 products to reduce the tropospheric phase delays. Finally, we correct the phase ramps, and topographic errors, and estimate the average velocity. We follow the workflow in Mintpy software given in Figure 5.15. For further details please see the article Yunjun et al. (2019).

For the track DT123, not available in the required time interval at the ARIA platform, we use the LiCSAR platform (Lazeckỳ et al., 2020), managed by the Centre for the Observation and Modelling of Earthquakes, Volcanoes and Tec-

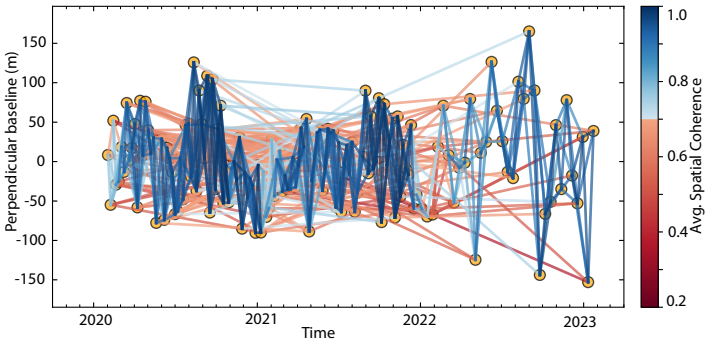

Figure 5.11: Network of ascending track (AT116) interferograms used for the SBAS time series analysis with the Mintpy software.

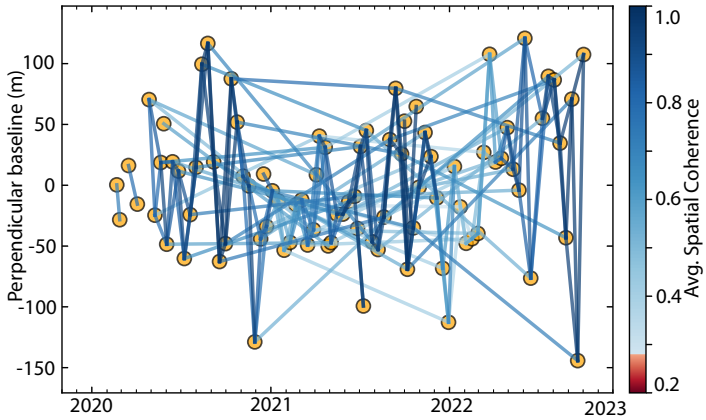

Figure 5.12: Network of ascending track (AT43) interferograms used for the SBAS time series analysis with the Mintpy software.

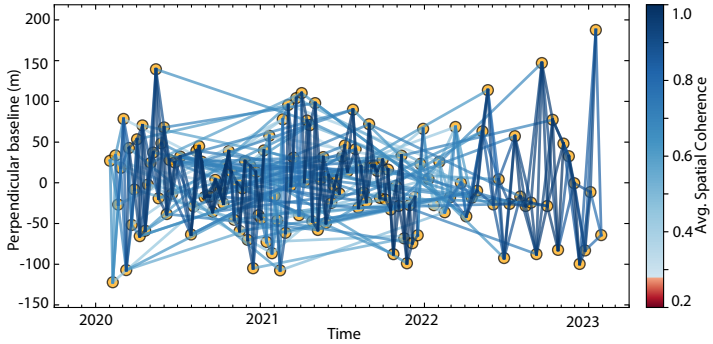

Figure 5.13: Network of descending track (DT21) interferograms used for the SBAS time series analysis with the Mintpy software.

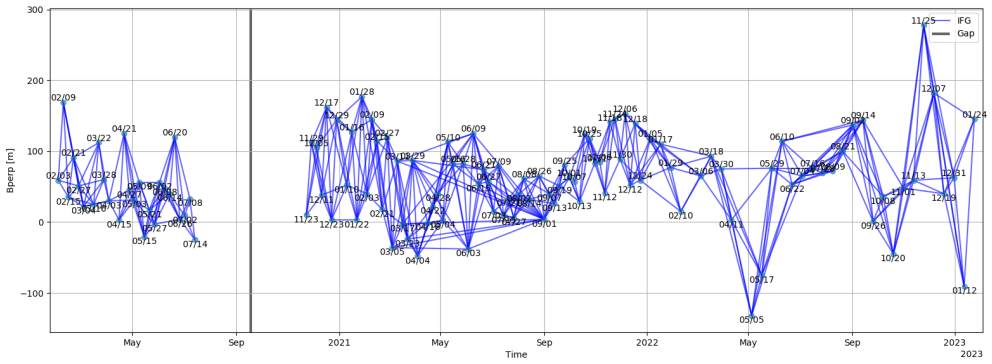

Figure 5.14: Network of descending track (DT123) interferograms used for the SBAS time series analysis with the LiCSBAS software.

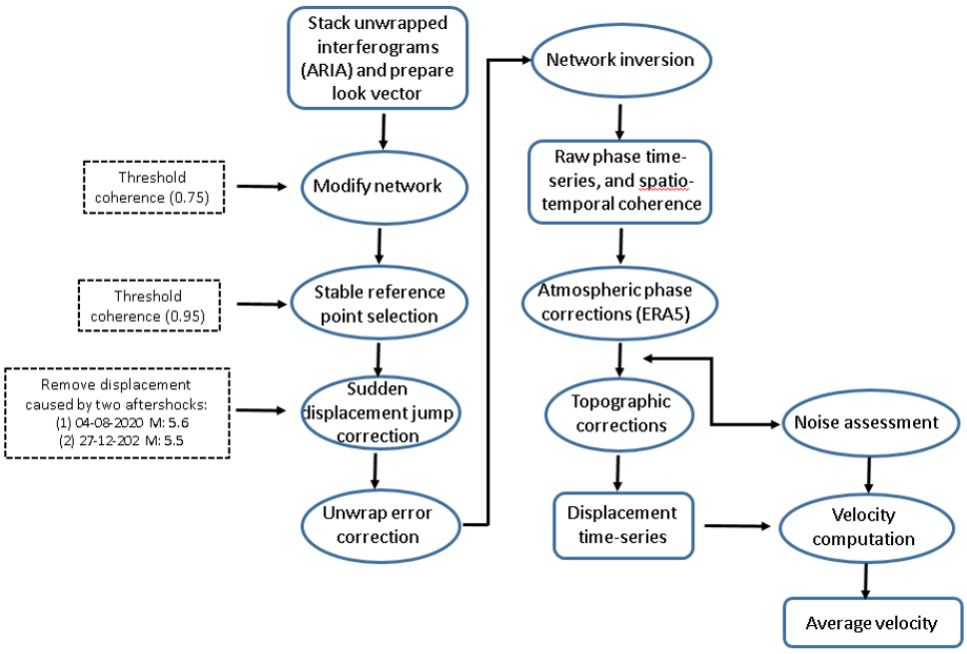

Figure 5.15: The detailed workflow we follow with the Mintpy software to process the time series of the Sentinel-1 geocoded unwrapped interferograms of tracks AT116, AT43, and DT21. The workflow is modified from Yunjun et al. (2019)

tonics (COMET). The major aim of the project is to comprehensively monitor the volcanoes, landslides, earthquake deformation, and tectonic movements utilizing Sentinel-1 SAR interferometry. It provides high-resolution tectonic strain maps, aiding in the development of advanced models for seismic and volcanic hazards. The LiCSAR platform generates interferograms on a predefined frame covering an area of 250 ×250 km^2, and consists of three subswaths. The LiCSAR platform provides multi-look interferograms of the order of 4 and 20 in azimuth and range directions, respectively. The Goldstein adaptive spectrum filter is applied to reduce and attenuate the noise level in each interferogram (Goldstein and Werner, 1998). Phase unwrapping is implemented using SNAPHU software (C. Chen and Zebker, 2001; 2002). Finally, the wrapped and unwrapped phase interferograms, along with coherence images are geocoded and saved to GeoTIFF format for further analysis by researchers.

We select 120 geocoded interferograms to estimate slip rates using LiCSBAS software (Morishita et al., 2020) for the track DT123 between January 29, 2020 – after the Mw 6.8 Elazığ earthquake and January 29, 2023 – prior the Mw 7.8 Kahramanmaraş seismic sequence covering the EAF system (Figure 5.14). We select the interferograms that have a perpendicular baseline smaller than 150 m and are least affected by seasonal atmospheric variation to retain a high correlation. Each interferogram is corrected by the path delays produced by atmospheric turbulence using the globally available GACOS products (Yu et al., 2018a). The time series network of the descending track (DT123) is shown in Figure 5.14. Moreover, we can also implement a spatio-temporal filter to enhance the signal to noise ratio and further eliminate the remaining inaccuracies incurred by the atmosphere. However, applying a large spatio-temporal filter– for instance, 50 days temporal, and 40 km spatial filter may oversmooth the true deformation produced by tectonic processes. In this study, we did not apply the spatio-temporal filter, and estimate the true deformation for each pixel. However, we remove the long wavelength linear trend by applying the de-ramping function. For further details please see the article Morishita et al. (2020)

5.4.4 Analysis of Fault Creep at Pütürge Segment

For the track AT116, we estimate the velocity in the LOS direction through the SBAS time series algorithm implemented in Mintpy software (Yunjun et al., 2019) between January 29, 2020, and January 29, 2023. The velocity is estimated with a reference image of February 14, 2020, on a pixel shown by a light blue colored rectangle in (Figure 5.16a). The reference pixel, identified based on a coherence threshold of 0.90, lies within a light blue rectangle depicted in Figure 5.16a. Positive velocity values indicate movement towards the satellite,

while negative values indicate movement away from it, aligning with the left lateral motion of the EAF system. We observe significant fault creep extending from the epicenter of the 2020 Mw 6.8 Elazığ earthquake towards the Pütürge segment, as shown in Figure 5.16a. The maximum creep rate of approximately 20 mm/yr is observed at the southern portion of the Pütürge segment, coinciding with the region where negligible coseismic slip was detected (Figure 5.16a and 5.10a, b).

Notably, we also find near-zero slip rates on the fault segments associated with the 06 February 2023 Mw 7.8 Kahramanmaraş and Mw 7.6 Elbistan earthquakes (Figure 5.16a). This suggests that the southern segments of the EAF system, where these earthquakes occurred, remained locked, accumulating stress until a continuous rupture in 2023 triggered the two powerful earthquakes. In order to understand velocity variations, we plot two profiles, BB' and CC', across the EAF system. Both profiles reveal a velocity jump of up to 20 mm/year (Figure 5.16b, c). Maximum velocity is observed near the fault trace, gradually diminishing away from it. We also analyze the time series movement on pixels P1 and P2, marked by red and yellow hexagons respectively, across the fault trace (Figure 5.16a, d, and e). Pixel P1 (red hexagon) exhibits a motion of approximately 28 mm towards the satellite in the LOS direction (Figure 5.16d). Additionally, pixel P2 (yellow hexagon) moves away from the satellite by around 53 mm (Figure 5.16e).

Similarly, we estimate the velocity along the LOS direction for the track DT21 using the SBAS time series algorithm implemented in Mintpy software (Yunjun et al., 2019) between January 29, 2020, and January 29, 2023. The velocity is calculated using a reference image taken on February 15, 2020, focusing on a stable reference pixel (Figure 5.17a). The date and location of this reference point have only a small difference from the one used for the ascending track AT116 mentioned before. Positive and negative velocities across the fault justify the left-lateral movement of the EAF system. We observe a substantial fault creep extending from the epicenter of the 2020 Mw 6.8 Elazığ earthquake towards the Pütürge segment (Figure 5.17a). The maximum creep rate of approximately 15 mm/yr is recorded at the southern portion of the Pütürge segment SW of the 2020 Mw 6.8 Elazığ earthquake epicentre (Figure 5.17a), where negligible coseismic slip was observed (Figure 5.17a and 5.10a, b).

In order to assess the velocity variations, we plot two profiles BB' and DD' across the EAF system. We detect a velocity jump of approximately 15 mm/year for BB' (Figure 5.17b). However, we find low slip rates of around 4 mm/year as we move SW of the Pütürge segment. As expected, the maximum velocity is observed near the fault trace, diminishing further away from the EAF system fault trace for profile BB'. The velocity rates on profile DD' clarifies the nearly zero creep rates on the fault segments associated with the 2023 February 6, Mw 7.8 Kahramanmaraş, and Mw 7.6 Elbistan earthquakes (Figure 5.17a), and

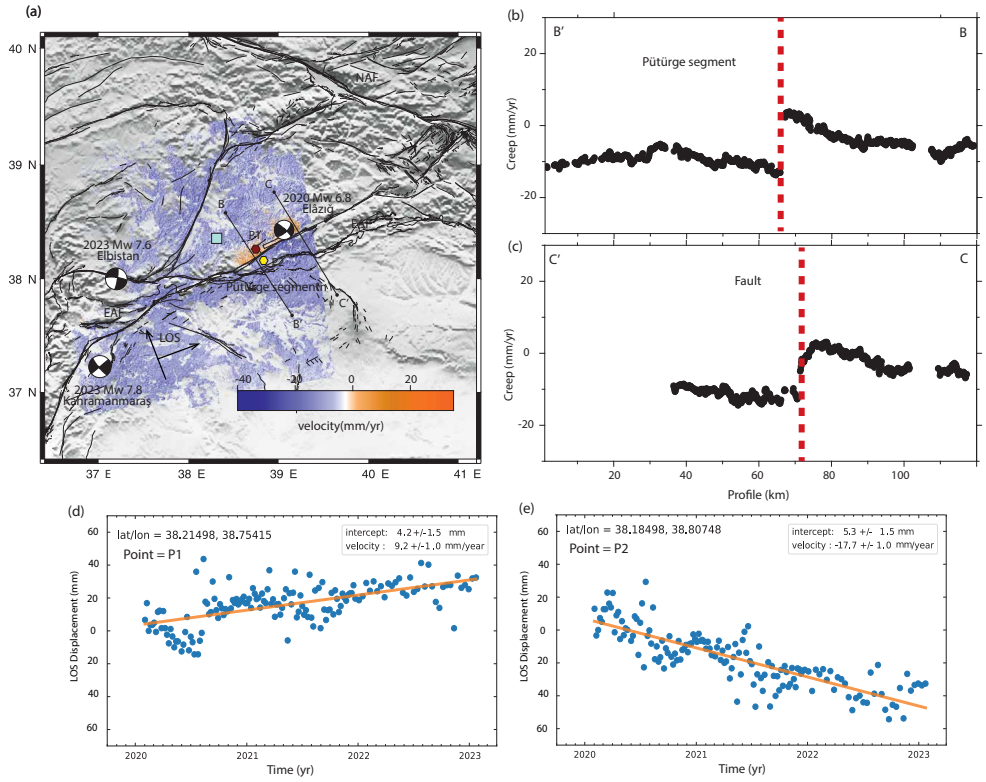

Figure 5.16: Velocity of the track AT116 from 29 January 2020 to 29 January 2023. (a) The velocity or creep rates estimated through SBAS time series analysis on the East Anatolian Fault (EAF) system. The velocity is estimated with reference to a stable pixel that exhibits a minimum 90% coherence shown by a light blue rectangle. The velocity shows a left lateral movement of the fault, the positive velocity shows the movement towards the satellite while negative velocity shows the movement away from the satellite. The focal mechanism solutions of the 2020 Mw 6.8 Elazığ, the 2023 Mw 7.8 Kahramanmaraş, and the 2023 Mw 7.6 Elbistan earthquakes are plotted. (b), and (c) The velocities on profiles BB' and CC' across the EAF system. The velocity jump can be seen across the EAF segments. (d) and (e) Time series movement in the line-of-sight direction on pixels P1 (red hexagon) and P2 (yellow hexagon) respectively.

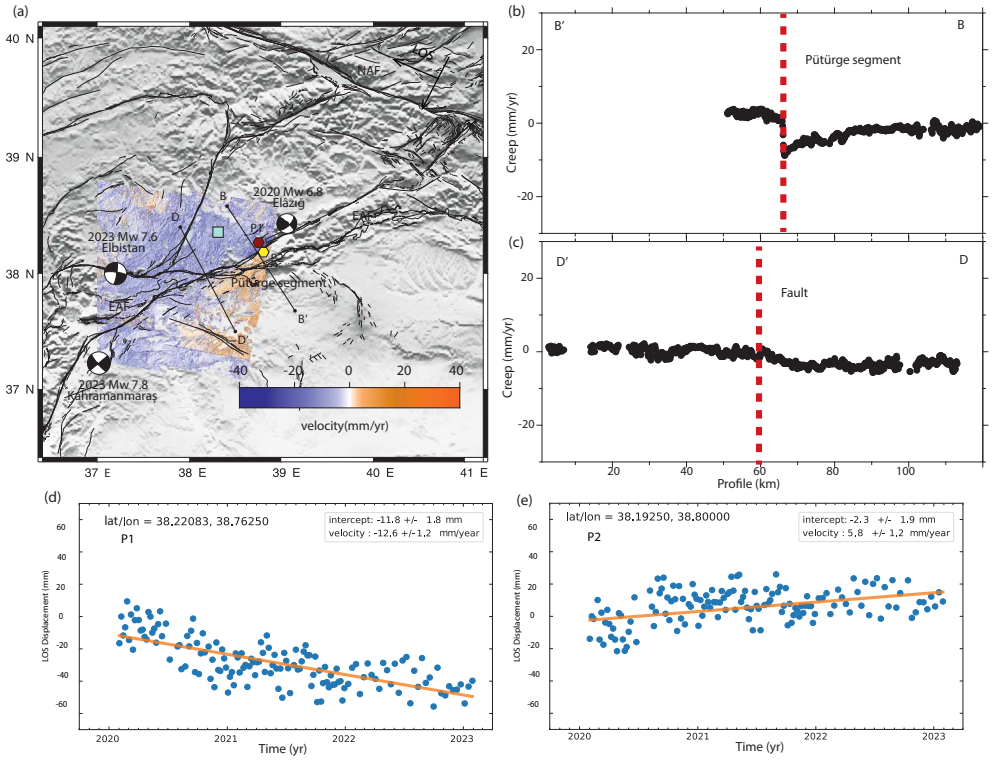

Figure 5.17: Velocity of the track DT21 from 29 January 2020 to 29 January 2023. (a) The velocity or creep rates estimated through SBAS time series analysis on the East Anatolian Fault (EAF) system. The velocity is estimated with reference to a stable pixel that exhibits a minimum 90% coherence shown by a light blue rectangle. The velocity shows a left lateral movement of the fault, the positive velocity shows the movement towards the satellite while negative velocity shows the movement away from the satellite. The focal mechanism solutions of the 2020 Mw 6.8 Elazığ, the 2023 Mw 7.8 Kahramanmaraş, and the 2023 Mw 7.6 Elbistan earthquakes are plotted. (b), and (c) The velocities on profiles BB' and DD' across the EAF system. The velocity jump can be seen across the EAF segments. (d) and (e) Time series movement in the line-of-sight direction on pixels P1 (red hexagon) and P2 (yellow hexagon) respectively.

rather shows the relative movement of the two plates starting from several decades of km from the fault. The velocity is close to zero on the profile crossing the same plate as the reference point, and slowly increases on the opposite side of the fault when reaching the stable plate movement rate at the distance of 70 km. This implies that the southern segments of the EAF system, encompassing the Kahramanmaraş and Elbistan earthquakes, remained locked and kept accumulating stress until unzipped in 2023 and generating two devastating earthquakes on the EAF system. We examine the time series movement of pixels P1 and P2 marked by red and yellow hexagons across the fault trace, respectively (Figure 5.17a, d, and e). Pixel P1 (red hexagon) moves approximately 39 mm away from the satellite in the line-of-sight direction (Figure 5.17d). Additionally, the pixel P2 (yellow hexagon) moves approximately 18 mm toward the satellite (Figure 5.17e).

We observe similar trends in tracks AT43 and DT123 across the Pütürge and northeastern sections of the 2020 Mw 6.8 Elazığ earthquake zone (Figures 5.18 and 5.19). These tracks have limited data, and are lacking the coverage south of the fault. Furthermore, the track DT123 exhibits a higher noise level compared to tracks AT116, AT43, and DT21. This track was processed using the LiCSBAS platform (Morishita et al., 2020) due to the absence of available geocoded unwrapped interferograms at the ARIA tools platform (Buzzanga et al., 2020) between 2020 and 2023. Nonetheless, the results still confirm the prevailing left-lateral movement trend across the EAF system, consistent with findings from other tracks. The positive and negative velocities observed in track DT123 support the left lateral movement of the EAF system. Moreover, we identify a significant creep rate of approximately 20 mm/year extending from the epicenter of the 2020 Mw 6.8 Elazığ earthquake towards the Pütürge segment (Figure 5.19a). To investigate velocity variations in the track DT123, we plot profiles BB' and CC' and time series of pixels P1 and P2 across the EAF system (Figures 5.19b - e). Both profiles exhibit a velocity jump of around 20 mm/year (Figures 5.19b, c). In contrast, slip rates along the track AT43 show a noticeable decrease in the northeast of the 2020 Mw 6.8 Elazığ earthquake zone (Figures 5.19a - e) and 5.18a - d). The BB' profile and time series on pixels P1 and P2 across the EAF system in track AT43 reveal a velocity jump of approximately 5 mm/year (Figures 5.18b - e).

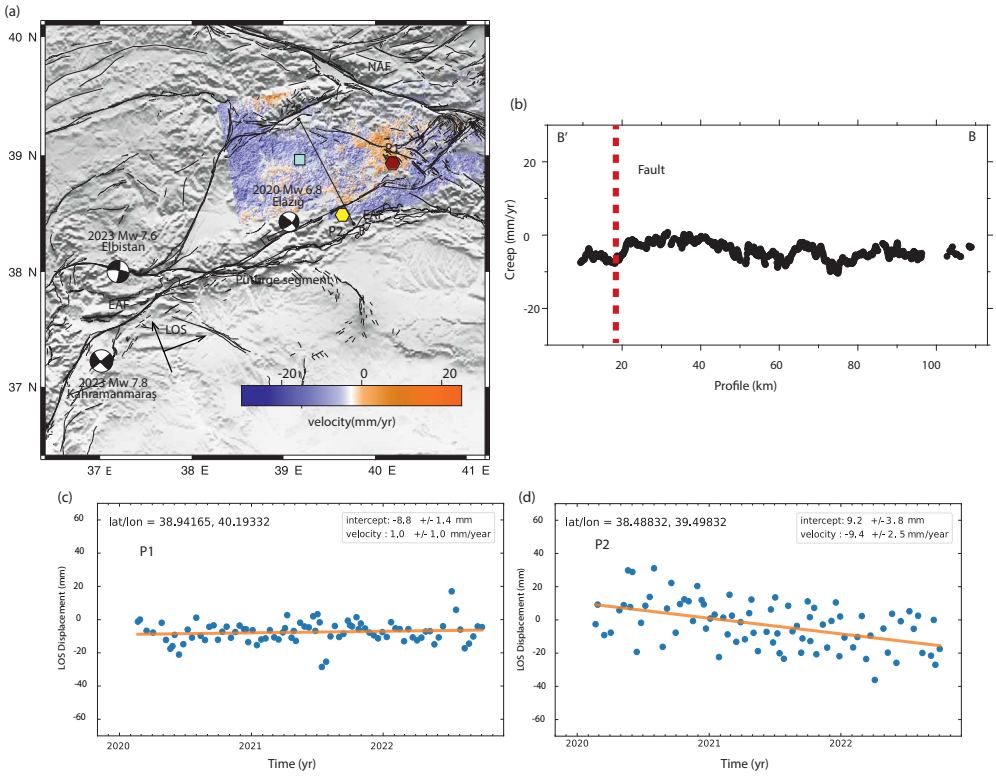

Figure 5.18: Velocity of the track AT43 from 29 January 2020 to 29 January 2023. (a) The velocity or creep rates estimated through SBAS time series analysis on the East Anatolian Fault (EAF) system. The velocity is estimated with reference to a stable pixel that exhibits a minimum 90% coherence shown by a light blue rectangle. The velocity shows a left lateral movement of the fault, the positive velocity shows the movement towards the satellite while negative velocity shows the movement away from the satellite. The focal mechanism solutions of the 2020 Mw 6.8 Elazığ, the 2023 Mw 7.8 Kahramanmaraş, and the 2023 Mw 7.6 Elbistan earthquakes are plotted. (b) The velocities on profiles BB' across the EAF system. The velocity jump can be seen across the EAF segments. (c) and (d) Time series movement in the line-of-sight direction on pixels P1 (red hexagon) and P2 (yellow hexagon) respectively.

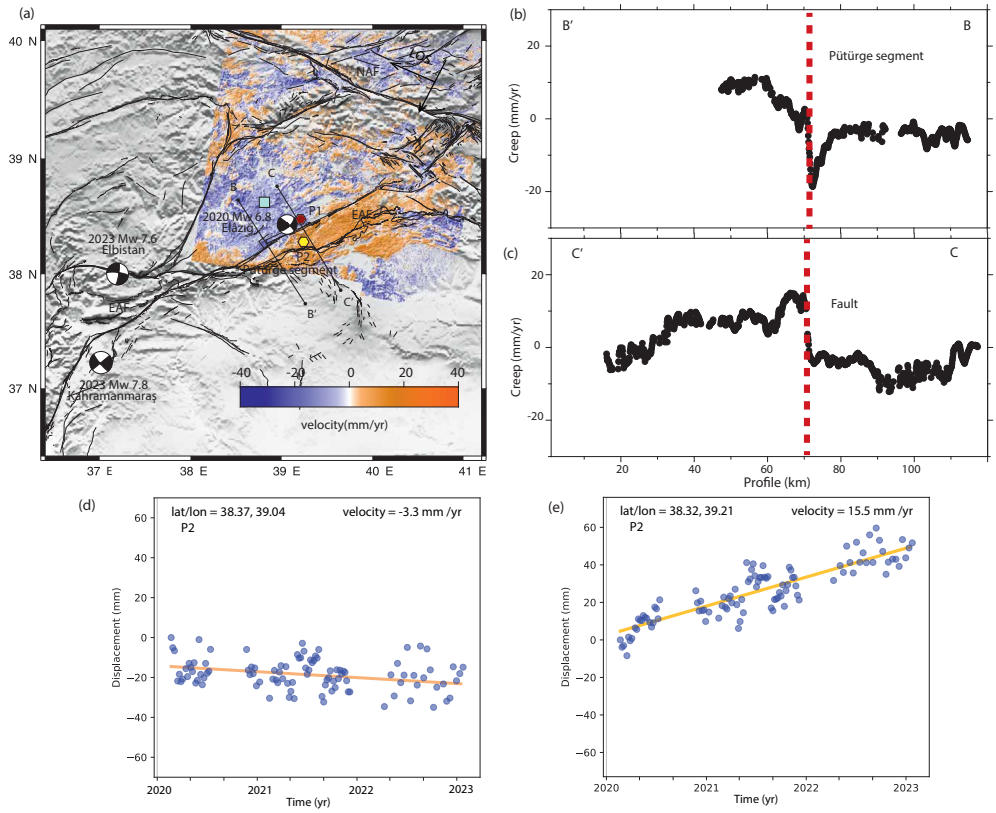

Figure 5.19: Velocity of the track DT123 from 29 January 2020 to 29 January 2023. (a) The velocity or creep rates estimated through SBAS time series analysis on the East Anatolian Fault (EAF) system. The velocity is estimated with reference to a stable pixel that exhibits a minimum 90% coherence shown by a light blue rectangle. The velocity shows a left lateral movement of the fault, the positive velocity shows the movement towards the satellite while negative velocity shows the movement away from the satellite. The focal mechanism solutions of the 2020 Mw 6.8 Elazığ, the 2023 Mw 7.8 Kahramanmaraş, and the 2023 Mw 7.6 Elbistan earthquakes are plotted. (b), and (c) The velocities on profiles BB' and CC' across the EAF system. The velocity jump can be seen across the EAF segments. (d) and (e) Time series movement in the line-of-sight direction on pixels P1 (red hexagon) and P2 (yellow hexagon) respectively.

5.5 Discussion

The distribution of coseismic slip includes revealing asperities of large slip centered along the South Amanos, North Amanos, Pazarcık, and Erkenek segments separated by major releasing bends and step-overs (Duman and Emre, 2013) 5.9). These segments ruptured several times in the last millennia. The Amanos segment hosted an Mw=7.5 earthquake in 521. The Pazarcık segment ruptured previously in 1513 with a Mw 7.4 earthquake. The Erkenek segment ruptured with a Mw 7.1 earthquake in 1893. Although all these segments ruptured in a single event during the Mw 7.8 mainshock of 2023, the waxing and waning of coseismic slip along the strike direction follows the same segmentation, with tapering of fault slip near segment boundaries. This behavior is compatible with the start-stop control of fault bends and morphological gradients on seismicity (Qiu et al., 2016; Sathiakumar and Barbot, 2021).

A somewhat surprising behavior of the Kahramanmaraş earthquake sequence is the rupture of faults with the same sense of motion — left-lateral strike-slip — despite the high angle between the Çardak Fault and the Pazarcık-Erkenek segment that hosted much coseismic slip. Recent strike-slip earthquakes on oblique faults, such as the 2012 Mw 8.6 Indian Ocean (Masuti et al., 2016; Wei et al., 2013) or the 2019 Mw 7.2 Ridgecrest (K. Chen et al., 2020; Qiu et al., 2020) earthquakes occurred on conjugate faults, i.e., one being dextral while the other is sinistral. The activation of faults with the same sense of motion is not uncommon within the context of escape tectonics that operates in Anatolia. For example, the oblique Altyn Tagh Fault and the Kunlun Fault in Tibet accommodate the extrusion of southern Tibet.

Regarding the recent 2023 earthquake sequence on the EAf system, a remaining question is how the Kahramanmaraş earthquake will affect future seismic unrest in the region. Of particular concern is the potential triggering of large earthquakes along the DSF system. However, the distribution of aftershocks and the fault orientation of the Mw 6.4 aftershock indicate propagation of seismic unrest toward the Cyprus Arc (Figures 5.2, and 5.9). Nevertheless, intense seismicity concentrates along the eastern side of the Karasu trough, running parallel to the Amanos segment in the direction of the DSF. Hence, the potential of a southward propagation of seismicity is not entirely excluded.

There are also some unprecedented observations regarding the lack of surface rupture during the coseismic slip of the 2020 Mw 6.8 Elazığ earthquake. There are several geological and geophysical explanations for the lack of surface rupture. Some authors suggest the rupture arrested at the shallow depth due to a slip deficit of around 1 m on the shallow fault (Cakir et al., 2023). Some authors proposed the presence of outcropping metamorphic rocks and multiple bends obstruct the rupture to emerge over the surface (Tatar et al., 2020). The

lack of a continuous surface rupture is also observed from field observations and satellite geodesy. Tatar et al. (2020) give various reasons for the lack of surface rupture: (1) the ruptured fault is not emergent to the surface; (2) the fault underwent left-lateral torque movement around a vertical axis (3) the Pütürge segment exhibits a restraining bend structure or the presence of metamorphic rocks along the fault strike that can obstruct the rupture to propagate to the surface. It is also found that most of the observed surface deformation features along the Pütürge segment in colluvial, or alluvial fan sediments (Tatar et al., 2020). The unconsolidated or poorly consolidated nature of these sediments may contribute to the absence of horizontal displacements on the surface.

The 2020 Mw 6.8 Elazığ earthquake has increased stress levels along the southwestern end of the Pütürge segment (Tatar et al., 2020). The sudden arrest near the surface needs a significantly higher a-b (rate and state frictional parameters) values of the rate and state friction law in this shallow velocity-strengthening creeping section. This phenomenon is somewhat analogous to observations from the southern half of the Mw 6.0, 2004 Parkfield earthquake (Johanson and Bürgmann, 2010; Mei et al., 2021; L. Wang, 2018) and the 1987 Mw 6.6 Superstition Hill earthquake (Marone et al., 1991), where a shallow creep dominated.

A major concern raised by the earthquake research community was that the slip distribution indicated a large remaining seismic gap in the Pütürge segment that separated the 2023 Mw 7.8 mainshock rupture and the fault area involved in the 2020 Mw 6.8 Elazığ earthquake (Figure 5.10b). The aftershock distribution connected the two ruptures between 10 and 20 km depth, leaving a 40 km long seismic gap between the surface and 10 km depth. Apparently, the locked area is similar to the spatial extent of the 2020 Elazığ earthquake rupture. Hence, there was a concern for the possibility of another Mw 6.8 earthquake to occur in the Pütürge segment of the EAF. Analysis of geodetic data across the Pütürge and Palu segment of the EAF indicated high interseismic coupling south of the 2020 Elazığ rupture (Bletery et al., 2020).

Overall, our SBAS time series analysis using all available ascending and descending tracks consistently shows creep on the Pütürge segment during the time interval extending after the 2020 Mw 6.8 Elazığ earthquake and prior to the February 6, 2023 Kahramanmaraş earthquakes sequence. Comprehensive results between 2020 and 2023 SAR observations provide insights into the intricate mechanisms underlying the rupture of a shallow creeping fault between two recent major seismic events that struck the central and southern parts of the EAF system. Afterslip reached its peak values in regions where the coseismic rupture of the 2020 Mw 6.8 Elazığ and 2023 Kahramanmaraş earthquakes sequence was negligible (Figure 5.16a, 5.17a, 5.9a and 5.10a, b).

The shallow coseismic slip of the 2020 Mw 6.8 Elazığ earthquake was ab-

sent within 1 - 2 kilometers of the surface. The coseismic rupture of the 2023 Kahramanmaraş earthquakes sequence stopped abruptly prior to propagating the Pütürge segment, where ongoing afterslip is anticipated since the 2020 Mw 6.8 Elazığ earthquake (Figure 5.16a, 5.17a, 5.9a and 5.10a, b). The surface slip commenced following the mainshock and continued as an afterslip on the Pütürge segment. Large aftershocks occurred in deeper zones characterized by low coseismic slip and reduced afterslip rates (Figure 5.10a). These results provide a handful of geodetic analyses to answer the concerns of the interseismic or postseismic coupling between the 2020 Elazığ and the 2023 Kahramanmaraş earthquakes at the Pütürge segment of EAF zone.

5.6 Conclusions

Remote sensing data provide great insights into the 2023 Kahramanmaraş earthquake sequence, including the extent of the surface rupture and the distribution of coseismic slip along various segments of the EAF and Çardak fault during the Mw 7.8 mainshock and the Mw 7.6 aftershock. The mainshock ruptured the Amanos, Pazarcık, and Erkenek segments propagating across fault bends and releasing step-overs. The southward rupture termination was caused by the diffuse termination of the EAF as it bifurcates into the Antakya Fault and the DSF. The second largest aftershock, the Antakya Mw 6.4 earthquake extends the rupture along the Antakya fault toward the Mediterranean Basin, alleviating the risk of triggering large earthquakes on the DSF. To the north, the rupture propagation was arrested by the Yarpuzlu releasing bend at the southern boundary of the Pütürge segment of the EAF, leaving a 40 km-long seismic gap to the rupture area of the 2020 Mw 6.8 Elazığ earthquake. The Pütürge segment must be instrumented to assess its seismic potential.

The Mw 7.6 Elbistan aftershock ruptured the nearby Çardak and Savrun faults and a previously unidentified fault situated across the Nurhak complexity between the Sürgü fault and the Malatya fault. The Mw 7.8 mainshock and the Mw 7.6 aftershock share the same sense of motion — left-lateral strike-slip faulting — despite markedly different fault orientations. The distribution of coseismic slip for both events highlights a pronounced shallow slip deficit and a complementarity with the aftershock distribution. These observations provide constraints on the depth of the seismogenic zone, defined as the area where large earthquakes nucleate and propagate. The depth distributions of aftershocks and of coseismic slip indicate an unstable-weakening region between 4 and 10 km depth. The Kahramanmaraş earthquake sequence reminds us of the devastating potential of immature strike-slip faults.

InSAR analysis with SBAS time series using both ascending and descending

tracks consistently shows a creep on the Pütürge segment during the time interval extending after the 2020 Mw 6.8 Elazığ earthquake to prior the February 6, 2023 Kahramanmaraş earthquakes sequence. We find a velocity jump in the line-of-sight direction up to 20 mm/yr for all the available tracks. The creep concentrates at the boundary and shallow depth of the seismic gap, possibly representing the afterslip of the 2020 Elazığ earthquake. Maximum velocity is observed near the fault trace, gradually diminishing away from it. The spatial distribution of creep is compatible with a remaining seismic gap along the Pütürge segment. The section is kinematically locked. Notably, we also find near-zero slip rates on the fault segments associated with the 06 February 2023 Mw 7.8 Kahramanmaraş and Mw7.6 Elbistan earthquakes. This suggests that the southern segments of the EAF system, where these earthquakes occurred, remained locked, accumulating stress until a continuous rupture in 2023 triggered the two powerful earthquakes, Mw 7.8 and Mw 7.6, separated by approximately 9 hours. This study clarifies the seismic potential of the Pütürge segment. We are aiming to work further on the remaining questions: (1) Three-dimensional slip distribution to understand the creep rates in depth, (2) Lithological control of fault creep surrounding the seismic gap, (3) Mechanisms of triggering of remaining locked section.

6 Conclusions

In the thesis, we investigate the two key convergence zones: (1) the SFT belt at the western boundary of the Indian-Eurasian plates, and (2) the EAF zone at the indentation of the Arabian into the Anatolian plates. Both zones are separated by the Persia-Tibet-Burma Orogenic belts along the Bitlis-Zagros fold and thrust belt (Barnhart et al., 2018; Sepehr and Cosgrove, 2004; Yassaghi and Marone, 2019). Both zones are highly active in terms of seismic deformation, but they exhibit distinct deformation patterns. In the SFT belt, earthquakes such as the 2015 Mw 5.7 Dajal and the 2021 Mw 6.0 Harnai are thrust-dominated while the 2020 Mw 6.8 Elazığ earthquake, the 2023 Mw 7.8 Kahramanmaraş, the Mw 7.6 Elbistan, and the Mw 6.4 Antakya earthquakes are left-lateral strike slips earthquake. These types of complex faults are predominantly characterized by fault bends and step-over structures (Barka and Kadinsky, 1988; Cakir et al., 2023; Konca et al., 2021; Tatar et al., 2012; Yule and Sieh, 2003). In recent decades, the advancement of space geodesy enables us to monitor and provide insights into complex deformation processes and characterize their temporal and spatial variations (Barbot and Weiss, 2021; Barbot et al., 2023; Gordon and S. Stein, 1992; S. Stein, 1993).

The SAR interferometry allows us to investigate the processes involved in the multiple phases of the earthquake cycle including the preseismic, coseismic, and postseismic movement. We study the details of the coseismic folding due to the 2015 Dajal earthquake in the front of the SFT belt (discussed in Chapter 3). We also investigate the coseismic, postseismic, and preseismic phases of the 2021 Harnai earthquake in the western SFT belt through SBAS time series analysis (discussed in Chapter 4). We use Sentinel-1 SAR observations to investigate the complex deformation processes occurring across the wide fault zone of the SFT belt which was formed during the India-Eurasia collision in the late Cenozoic. Further, we study the different seismic phases of the earthquakes in the EAF zone for the years 2020 to 2023 (discussed in Chapter 5). The earthquakes that occurred in this period on the EAF are January 24 2020 Mw 6.8 Elazığ earthquake, February 06 2023 Mw 7.8 Kahramanmaraş, and Mw 7.6 Elbistan earthquakes, February 20 2023 Mw 6.4 Antakya aftershock.

The coseismic deformation associated with the 2015 Mw 5.7 Dajal blind earthquake at the eastern boundary of the SFT shows the earthquake ruptured the base of the Boundary Thrust buried under the sediment from the Indus River

floodplain, representing fault-bend or fault-propagation folding some 30 km off its nearest surface exposure. We conclude the rupture and associated folding in the hanging wall document the eastward growth of the SFT. The earthquake represents the seismic rupture of a frontal blind ramp of the SFT, presumably as the seismic expression of a Fault-Bend Fold (FBF) or Fault-Propagation Fold (FPF). The earthquake was accompanied by coseismic folding accommodated by flexural slip along an active axial surface. The deformation is captured at the temporal resolution afforded by the radar acquisitions, which includes between 10 and 18 days of potential postseismic deformation. Despite this short period of observation, flexural slip is tantamount to 70% of the expected value for coseismic folding, indicating strong mechanical coupling and synchronicity between faulting and folding at the time scales of the seismic cycle. While the Dajal earthquake demonstrates the seismic potential of the deformation front of fold-and-thrust belts, the folded sediments above the blind ramp exert a strong control on the rupture propagation. Further seismic exploration of fold-and-thrust belts will be crucial to anticipate the location and size of future seismicity in this widespread tectonic setting.

The western zone of the SFT belt exhibits high seismic hazard. Here, we take advantage of the Sentinel-1, and ALOS-2 ScanSAR satellite observations to estimate the coseismic deformation caused by the 2021 Mw 6.0 Harnai earthquake. We conclude that the coseismic surface deformation along the line-of-sight (LOS) is estimated as 70 mm and 80 mm for ascending and descending interferograms, respectively. Modeling of InSAR data reveals primarily thrust-dominated slip in up-dip direction with a strike-slip component that is in good agreement with the tectonic context of the transpressional Karahi and Harnai faults. Source fault geometry along with the corresponding uncertainty of the 2021 Mw 6.0 Harnai earthquake and preseismic InSAR-derived movement shows the fault was locked until 2021, prior to the rupture. The finite slip models show that 95% of slip is concentrated between 3 and 10 km depth. The NW-SE oriented rupture rather than the NE-SW oriented model is justified by the tectonic setting and fault structure of the Harnai fault. The major part of the deformation is observed in the hanging wall placed to the south of the Harnai fault. The 2021 Mw 6.0 Harnai earthquake occurred approximately 60 km NW of the 27 February 1997 Mw 6.9 doublet earthquake on the same fault. The 2021 Harnai earthquake NW-SE trending fault model is compatible with the focal mechanism of the 1997 doublet. The 2021 earthquake shares the same fault segment as the 1997 doublet aftershocks with Mw 5.6 (March 20, 1997), Mw 5.5 (August 24, 1997), and Mw 5.0 (June 17, 1997). Moreover, the northwestern extension of the Harnai fault merges with the active right lateral Urghargai strike-slip fault, the latter had been ruptured with an Mw 7.0 earthquake in 1931, next to relatively smaller recent strike-slip events. The left lateral active strike-slip Karahi fault departs

from the above junction and extends eastward subparallel to the Harnai fault. Therefore, the Harnai thrust-dominated fault is sandwiched between two active strike-slip faults.

Integrating different methods of satellite geodesy provides great insights into the 2023 Kahramanmaraş earthquake sequence, including the extent of the surface rupture and the distribution of coseismic slip along various segments of the EAF and Çardak fault during the Mw 7.8 mainshock and the Mw 7.6 aftershock. The mainshock ruptured the Amanos, Pazarcık, and Erkenek segments propagating across fault bends and releasing step-overs. The southward rupture termination was caused by the diffuse termination of the EAF as it bifurcates into the Antakya Fault and the DSF. The second largest aftershock, the Antakya Mw 6.4 earthquake extends the rupture along the Antakya Fault toward the Mediterranean Basin, alleviating the risk of triggering large earthquakes on the DSF. To the north, the rupture propagation was arrested by the Yarpuzlu releasing bend at the southern boundary of the Pütürge segment of the EAF, leaving a 40 km-long seismic gap to the rupture area of the 2020 Mw 6.8 Elazığ earthquake. The Pütürge segment must be instrumented to assess its seismic potential.

The coseismic slip of the 06 February 2023 Turkey earthquakes collectively ruptured approximately 580 km long rupture consisting of 14 fault segments with varying strikes and dips along the EAF system, resulting in a maximum slip of 12 m (Barbot et al., 2023; Melgar et al., 2023). For the postseismic phase of the 2020 Mw 6.8 Elazığ earthquake, we study approximately 250 km long fault segments from the Pütürge segment to the Karliova triple junction point. Overall, we investigate the approximately 850 km long EAF fault zone for the coseismic and postseismic phases, consisting of the creeping, and locked sections. Investigating such a large fault system is a difficult task, but SAR Interferometry provides valuable tools for accurately investigating the sources of the complex tectonic processes and the response of the deforming elastic and viscoelastic crust at regional and tectonic plate scales (Barbot et al., 2023; Cakir et al., 2023; Feng et al., 2015; Javed et al., 2022; R. Jolivet et al., 2012; Rollins et al., 2018).

The EAF features creeping segments to the north, near the Karliova triple junction and around Hazir Lake in the Palu and Pütürge segments, but is locked during the interseismic cycle in the remaining segments. We test this hypothesis and perform SBAS time series analysis using Sentinel-1 SAR interferometry to identify the extent of creep along the EAF, particularly along the 40 km long Pütürge segment. We conclude our InSAR analysis with SBAS time series using both ascending and descending tracks consistently shows a creep on Pütürge segment during the time interval– after 2020 Mw 6.8 Elazığ earthquake and prior to the February 6, 2023 Kahramanmaraş earthquakes sequence. We

find a velocity jump in the line-of-sight direction up to 20 mm/yr for all the available tracks. The creep concentrates at the boundary and shallow depth of the seismic gap, possibly representing the afterslip of the 2020 Elazığ earthquake. Maximum velocity is observed near the fault trace, gradually diminishing away from it. The spatial distribution of creep is compatible with a remaining seismic gap along the Pütürge segment. The section is kinematically locked. Notably, we also find near-zero slip rates on the fault segments associated with the 06 February 2023 Mw 7.8 Kahramanmaraş and the Mw 7.6 Elbistan earthquakes. This suggests that the southern segments of the EAF system, where these earthquakes occurred, remained locked, accumulating stress until a continuous rupture in 2023 triggered the two powerful earthquakes, Mw 7.8 and Mw 7.6, separated by approximately 9 hours. This study clarifies the seismic potential of the Pütürge segment. We are aiming to work further on the remaining questions: (1) Three-dimensional slip distribution to understand the creep rates in depth, (2) Lithological control of fault creep surrounding the seismic gap, (3) Mechanisms of triggering of remaining locked section.

Bibliography

Agata, R., Barbot, S. D., Fujita, K., Hyodo, M., Iinuma, T., Nakata, R., Ichimura, T., and Hori, T. (2019). "Rapid mantle flow with power-law creep explains deformation after the 2011 Tohoku mega-quake". *Nature Communications* 10.1, p. 1385. DOI: 10.1038/s41467-019-08984-7.

Akaike, H. (1985). "Prediction and entropy". In: *Selected Papers of Hirotugu Akaike*. Springer, pp. 387–410.

Aktug, B., Ozener, H., Dogru, A., Sabuncu, A., Turgut, B., Halicioglu, K., Yilmaz, O., and Havazli, E. (2016). "Slip rates and seismic potential on the East Anatolian Fault System using an improved GPS velocity field". *Journal of Geodynamics* 94, pp. 1–12. DOI: 10.1016/j.jog.2016.01.001.

Albano, M., Barba, S., Bignami, C., Carminati, E., Doglioni, C., Moro, M., Saroli, M., Samsonov, S., and Stramondo, S. (2021). "Numerical analysis of interseismic, coseismic and post-seismic phases for normal and reverse faulting earthquakes in Italy". *Geophysical Journal International* 225.1, pp. 627–645.

Ambraseys, N. (1970). "Some Characteristic Features of the North Anatolian Fault Zone". 9, pp. 143–165.

Ambraseys, N. and Bilham, R. (2003). "Earthquakes and associated deformation in northern Baluchistan 1892-2001". *Bulletin of the Seismological Society of America* 93.4, pp. 1573–1605.

Ambraseys, N. and Bilham, R. (2012). "The Sarez-Pamir earthquake and landslide of 18 February 1911". 83.2, pp. 294–314.

Ando, R. and Kaneko, Y. (2018). "Dynamic rupture simulation reproduces spontaneous multifault rupture and arrest during the 2016 Mw 7.9 Kaikoura earthquake". 45.23, pp. 12–875. DOI: 10.1029/2018GL080550.

Aster, R. C., Borchers, B., and Thurber, C. H. (2012). *Parameter estimation and inverse problems*. 2nd. Academic Press, p. 376. ISBN: 9780123850485.

Bagnardi, M. and Hooper, A. (2018). "Inversion of surface deformation data for rapid estimates of source parameters and uncertainties: A Bayesian approach". 19.7, pp. 2194–2211.

Bamler, R. and Hartl, P. (1998). "Synthetic aperture radar interferometry". *Inverse problems* 14.4, R1.

Banks, C. and Warburton, J. (1986). "'Passive-roof' duplex geometry in the frontal structures of the Kirthar and Sulaiman mountain belts, Pakistan".

Journal of structural Geology 8.3-4, pp. 229–237. DOI: 10.1016/0191-8141(86)90045-3.

Baran, I., Stewart, M. P., Kampes, B. M., Perski, Z., and Lilly, P. (2003). "A modification to the Goldstein radar interferogram filter". *IEEE Transactions on Geoscience and Remote Sensing* 41.9, pp. 2114–2118.

Barbot, S. and Weiss, J. (2021). "Connecting subduction, extension and shear localization across the Aegean Sea and Anatolia". 226.1, pp. 422–445. DOI: 10.1093/gji/ggab078.

Barbot, S., Agram, P., and De Michele, M. (2013). "Change of Apparent Segmentation of the San Andreas Fault Around Parkfield from Space Geodetic Observations Across Multiple Periods". 118.12, pp. 6311–6327. DOI: 10.1002/2013JB010442.

Barbot, S., Fialko, Y., and Sandwell, D. (June 2008). "Effect of a Compliant Fault Zone on the Inferred Earthquake Slip Distribution". 113.B6. DOI: 10.1029/2007JB005256.

Barbot, S., Luo, H., Wang, T., Hamiel, Y., Piatibratova, O., Javed, M. T., Braitenberg, C., Gurbuz, G., et al. (2023). "Slip distribution of the February 6, 2023 Mw 7.8 and Mw 7.6, Kahramanmaraş, Turkey earthquake sequence in the East Anatolian Fault Zone". *Seismica* 3.2.

Barka, A. and Kadinsky, C. K. (1988). "Strike-slip fault geometry in Turkey and its influence on earthquake activity". *Tectonics* 7.3, pp. 663–684. DOI: 10.1029/TC007i003p00663.

Barka, A. (1996). "Slip distribution along the North Anatolian fault associated with the large earthquakes of the period 1939 to 1967". *Bulletin of the Seismological Society of America* 86.5, pp. 1238–1254.

Barkat, A., Javed, F., Joe Tan, Y., Ali, A., Javed, M. T., Ahmad, N., Awais, M., Ali Shah, M., and Iqbal, T. (2022). "2019 M w 5.9 Mirpur, Pakistan Earthquake: Insights from Integrating Geodetic, Seismic, and Field Observations". *Seismological Society of America* 93.4, pp. 2015–2026.

Barnhart, W. D., Brengman, C. M., Li, S., and Peterson, K. E. (2018). "Ramp-flat basement structures of the Zagros Mountains inferred from co-seismic slip and afterslip of the 2017 Mw7.3 Darbandikhan, Iran/Iraq earthquake". 496, pp. 96–107. DOI: 10.1016/j.epsl.2018.05.036.

Berardino, P., Fornaro, G., Lanari, R., and Sansosti, E. (2002). "A new algorithm for surface deformation monitoring based on small baseline differential SAR interferograms". 40.11, pp. 2375–2383.

Bernard, M., Shen-Tu, B., Holt, W., and Davis, D. (2000). "Kinematics of active deformation in the Sulaiman Lobe and Range, Pakistan". *Journal of Geophysical Research: Solid Earth* 105.B6, pp. 13253–13279.

Besoya, M., Govil, H., and Bhaumik, P. (2021). “A review on surface deformation evaluation using multitemporal SAR interferometry techniques”. *Spatial Information Research* 29, pp. 267–280.

Billi, A., Gambini, R., Nicolai, C., and Storti, F. (2007). “Neogene-Quaternary intraforeland transpression along a Mesozoic platform-basin margin: The Gargano fault system, Adria, Italy”. *Geosphere* 3.1, pp. 1–15.

Bletery, Q., Cavalié, O., Nocquet, J.-M., and Ragon, T. (2020). “Distribution of interseismic coupling along the North and East Anatolian Faults inferred from InSAR and GPS data”. 47.16, e2020GL087775. DOI: 10.1029/2020GL087775.

Blewitt, G. (2007). “GPS and space based geodetic methods”. *Treatise on Geophysics* 3, pp. 351–390.

Bozkurt, E. (2001). “Neotectonics of Turkey–a synthesis”. *Geodinamica acta* 14.1-3, pp. 3–30. DOI: 10.1080/09853111.2001.11432432.

Brown, W. M. and Porcello, L. J. (1969). “An introduction to synthetic-aperture radar”. *IEEE spectrum* 6.9, pp. 52–62.

Buzzanga, B., Bekaert, D. P., Hamlington, B. D., and Sangha, S. S. (2020). “Toward sustained monitoring of subsidence at the coast using InSAR and GPS: An application in Hampton Roads, Virginia”. *Geophysical Research Letters* 47.18, e2020GL090013.

Cakir, Z., Doğan, U., Akoğlu, A. M., Ergintav, S., Özarpacı, S., Özdemir, A., Nozadkhalil, T., Çakir, N., Zabcı, C., Erkoç, M. H., et al. (2023). “Arrest of the Mw 6.8 January 24, 2020 Elaziğ (Turkey) earthquake by shallow fault creep”. *Earth and Planetary Science Letters* 608, p. 118085.

Cavalié, O. and Jónsson, S. (2014). “Block-like plate movements in eastern Anatolia observed by InSAR”. 41.1, pp. 26–31. DOI: 10.1002/2013GL058170.

Chang, S.-H., Avouac, J.-P., Barbot, S., and Lee, J.-C. (2013). “Evidence for near-surface enhanced rate-strengthening derived from dynamic modeling of aseismic slip due to the 2004 Parkfield earthquake”. 118.7, pp. 3431–3447.

Chapple, W. M. (1978). “Mechanics of thin-skinned fold-and-thrust belts”. *Geological Society of America Bulletin* 89.8, pp. 1189–1198.

Chen, C. and Zebker, H. A. (2001). “Two-dimensional phase unwrapping with use of statistical models for cost functions in nonlinear optimization”. *JOSA A* 18.2, pp. 338–351.

Chen, C. and Zebker, H. A. (2002). “Phase unwrapping for large SAR interferograms: statistical segmentation and generalized network models”. *IEEE Trans. Geosci. Rem. Sens.* 40.8, pp. 1709–1719.

Chen, K., Avouac, J.-P., Aati, S., Milliner, C., Zheng, F., and Shi, C. (2020). “Cascading and pulse-like ruptures during the 2019 Ridgecrest earthquakes in the Eastern California Shear Zone”. *Nature communications* 11.1, pp. 1–8. DOI: 10.1038/s41467-019-13750-w.

Chiarabba, C., Jovane, L., and DiStefano, R. (2005). "A new view of Italian seismicity using 20 years of instrumental recordings". *Tectonophysics* 395.3-4, pp. 251–268.

Couples, G. D., Lewis, H., and Tanner, P. G. (1998). "Strain partitioning during flexural-slip folding". *Geological Society, London, Special Publications* 127.1, pp. 149–165. DOI: 10.1144/GSL.SP.1998.127.01.12.

Daout, S., Barbot, S., Peltzer, G., Doin, M.-P., Liu, Z., and Jolivet, R. (2016a). "Constraining the kinematics of metropolitan Los Angeles faults with a slip-partitioning model". 43.21. DOI: 10.1002/2016GL071061.

Daout, S., Jolivet, R., Lasserre, C., Doin, M.-P., Barbot, S., Tapponnier, P., Peltzer, G., Socquet, A., and Sun, J. (2016b). "Along-strike variations of the partitioning of convergence across the Haiyuan fault system detected by InSAR". 205.1, pp. 536–547. DOI: 10.1093/gji/ggw028.

Davis, D., Suppe, J., and Dahlen, F. (1983). "Mechanics of fold-and-thrust belts and accretionary wedges". *Journal of Geophysical Research: Solid Earth* 88.B2, pp. 1153–1172.

Davis, T. L., Namson, J., and Yerkes, R. F. (1989). "A cross section of the Los Angeles area: Seismically active fold and thrust belt, the 1987 Whittier Narrows earthquake, and earthquake hazard". *Journal of Geophysical Research: Solid Earth* 94.B7, pp. 9644–9664. DOI: 10.1029/JB094iB07p09644.

De Zan, F. and Monti Guarnieri, A. (2006). "TOPSAR: Terrain Observation by Progressive Scans". *IEEE Transactions on Geoscience and Remote Sensing* 44.9, pp. 2352–2360. DOI: 10.1109/TGRS.2006.873853.

Duman, T. Y. and Emre, Ö. (2013). "The East Anatolian Fault: geometry, segmentation and jog characteristics". *Geological Society, London, Special Publications* 372.1, pp. 495–529. DOI: 10.1144/SP372.1.

Eakin, D. H., McIntosh, K. D., Van Avendonk, H., Lavier, L., Lester, R., Liu, C.-S., and Lee, C.-S. (2014). "Crustal-scale seismic profiles across the Manila subduction zone: The transition from intraoceanic subduction to incipient collision". 119.1, pp. 1–17. DOI: 10.1002/2013JB010395.

Elliott, J., Walters, R., and Wright, T. (2016). "The role of space-based observation in understanding and responding to active tectonics and earthquakes". *Nature communications* 7.1, pp. 1–16. DOI: 10.1038/ncomms13844.

Emardson, T., Simons, M., and Webb, F. (2003). "Neutral atmospheric delay in interferometric synthetic aperture radar applications: Statistical description and mitigation". *Journal of Geophysical Research: Solid Earth* 108.B5.

Emre, Ö., Duman, T., Özalp, S., Şaroğlu, F., Olgun, Ş., Elmaci, H., and Can, T. (July 2018). "Active fault database of Turkey". *Bulletin of Earthquake Engineering* 16, pp. 3229–3275. DOI: 10.1007/s10518-016-0041-2.

Emre, Ö., Kondo, H., Özalp, S., and Elmacı, H. (2021). "Fault geometry, segmentation and slip distribution associated with the 1939 Erzincan earthquake rupture along the North Anatolian fault, Turkey".

England, P. C. and Houseman, G. A. (1986). "Finite Strain calculations of continental deformation II. Comparison with the India-Asia collision zone". 91, pp. 3664–3676.

Ergintav, S., McClusky, S., Hearn, E., Reilinger, R., Cakmak, R., Herring, T., Ozener, H., Lenk, O., and Tari, E. (2009). "Seven years of postseismic deformation following the 1999, M=7.4 and M=7.2, Izmit-Düzce, Turkey earthquake sequence". 114.B07403.

Farr, T. G., Rosen, P. A., Caro, E., Crippen, R., Duren, R., Hensley, S., Kobrick, M., Paller, M., Rodriguez, E., Roth, L., et al. (2007). "The shuttle radar topography mission". *Reviews of geophysics* 45.2.

Fattahi, H. and Amelung, F. (2016). "InSAR observations of strain accumulation and fault creep along the Chaman Fault system, Pakistan and Afghanistan". *Geophysical Research Letters* 43.16, pp. 8399–8406.

Feng, L., Hill, E. M., Banerjee, P., Hermawan, I., Tsang, L. L., Natawidjaja, D. H., Suwargadi, B. W., and Sieh, K. (2015). "A unified GPS-based earthquake catalog for the Sumatran plate boundary between 2002 and 2013". *Journal of Geophysical Research: Solid Earth* 120.5, pp. 3566–3598.

Ferretti, A., MONTI-GUARNIERI, A. V., Prati, C., Rocca, F., and Massonnet, D. (2007). *INSAR Principles A*. ESA publications.

Fialko, Y. (2004a). "Evidence of fluid-filled upper crust from observations of post-seismic deformation due to the 1992 M_w7.3 Landers earthquake". 109, B08401, 10.1029/2004JB002985.

Fialko, Y. (2004b). "Probing the mechanical properties of seismically active crust with space geodesy: Study of the co-seismic deformation due to the 1992 M_w7.3 Landers (Southern California) earthquake". 109.B03307.

Fialko, Y. (2004c). "Temperature fields generated by the elastodynamic propagation of shear cracks in the Earth". 109, B01303, 10.1029/2003JB002497.

Fialko, Y., Sandwell, D., Simons, M., and Rosen, P. (May 2005). "Three-dimensional deformation caused by the Bam, Iran, earthquake and the origin of shallow slip deficit". *Nature* 435, pp. 295–299.

Fielding, E. J., Lundgren, P. R., Bürgmann, R., and Funning, G. J. (2009). "Shallow fault-zone dilatancy recovery after the 2003 Bam earthquake in Iran". *Nature* 458, pp. 64–68.

Freed, A. M. and Bürgmann, R. (2004). "Evidence of power-law flow in the Mojave desert mantle". *Nature* 430, pp. 548–551. DOI: 10.1038/nature02784.

Fukuda, J. and Johnson, K. M. (2008). "A fully Bayesian inversion for spatial distribution of fault slip with objective smoothing". *Bulletin of the Seismological Society of America* 98.3, pp. 1128–1146.

Funning, G. J., Fukahata, Y., Yagi, Y., and Parsons, B. (2014). "A method for the joint inversion of geodetic and seismic waveform data using ABIC: application to the 1997 Manyi, Tibet, earthquake". 196.3, pp. 1564–1579.

Garfunkel, Z., Zak, I., and Freund, R. (1981). "Active faulting in the Dead Sea rift". 80.1-4, pp. 1–26. DOI: 10.1016/0040-1951(81)90139-6.

Garthwaite, M. C., Wang, H., and Wright, T. J. (2013). "Broadscale interseismic deformation and fault slip rates in the central Tibetan Plateau observed using InSAR". *Journal of Geophysical Research: Solid Earth* 118.9, pp. 5071–5083.

Ghayournajarkar, N. and Fukushima, Y. (2020). "Determination of the dipping direction of a blind reverse fault from InSAR: case study on the 2017 Sefid Sang earthquake, northeastern Iran". *earth, planets and space* 72.1, pp. 1–15.

Goldstein, R. M. and Werner, C. L. (1998). "Radar interferogram filtering for geophysical applications". *Geophysical research letters* 25.21, pp. 4035–4038.

Goldstein, R. M., Zebker, H. A., and Werner, C. L. (1988). "Satellite radar interferometry: Two-dimensional phase unwrapping". *Radio science* 23.4, pp. 713–720.

Gomba, G., Parizzi, A., De Zan, F., Eineder, M., and Bamler, R. (2015). "Toward operational compensation of ionospheric effects in SAR interferograms: The split-spectrum method". *IEEE Transactions on Geoscience and Remote Sensing* 54.3, pp. 1446–1461.

Gordon, R. G. and Stein, S. (1992). "Global tectonics and space geodesy". *Science* 256.5055, pp. 333–342.

Grandin, R., Klein, E., Métois, M., and Vigny, C. (2016). "Three-dimensional displacement field of the 2015 Mw8. 3 Illapel earthquake (Chile) from across- and along-track Sentinel-1 TOPS interferometry". *Geophysical Research Letters* 43.6, pp. 2552–2561.

Güvercin, S. E., Karabulut, H., Konca, A. Ö., Doğan, U., and Ergintav, S. (2022). "Active seismotectonics of the East Anatolian Fault". 230.1, pp. 50–69. DOI: 10.1093/gji/ggac045.

Ul-Hadi, S., Khan, S. D., Owen, L. A., and Khan, A. S. (2013). "Geomorphic response to an active transpressive regime: A case study along the Chaman strike-slip fault, western Pakistan". *Earth surface processes and landforms* 38.3, pp. 250–264.

Hamiel, Y. and Fialko, Y. (2007). "Structure and mechanical properties of faults in the North Anatolian Fault system from InSAR observations of coseismic deformation due to the 1999 Izmit (Turkey) earthquake". *Journal of Geophysical Research: Solid Earth* 112.B7.

Hanssen, R. F., Weckwerth, T. M., Zebker, H. A., and Klees, R. (1999). "High-resolution water vapor mapping from interferometric radar measurements". *Science* 283.5406, pp. 1297–1299.

Haq, S. S. and Davis, D. M. (1997). “Oblique convergence and the lobate mountain belts of western Pakistan”. *Geology* 25.1, pp. 23–26.

Hastings, W. K. (Apr. 1970). “Monte Carlo sampling methods using Markov chains and their applications”. *Biometrika* 57.1, pp. 97–109. ISSN: 0006-3444. DOI: 10.1093/biomet/57.1.97. eprint: https://academic.oup.com/biomet/article-pdf/57/1/97/23940249/57-1-97.pdf. URL: https://doi.org/10.1093/biomet/57.1.97.

Hearn, E. H., Bürgmann, R., and Reilinger, R. E. (Feb. 2002). “Dynamics of Izmit Earthquake Postseismic Deformation and Loading of the Düzce Earthquake Hypocenter”. 92.1, pp. 172–193.

Hooper, A. (2008). “A multi-temporal InSAR method incorporating both persistent scatterer and small baseline approaches”. *Geophysical Research Letters* 35.16.

Hubbard, J., Almeida, R., Foster, A., Sapkota, S. N., Bürgi, P., and Tapponnier, P. (2016). “Structural segmentation controlled the 2015 Mw 7.8 Gorkha earthquake rupture in Nepal”. *Geology* 44.8, pp. 639–642. DOI: 10.1130/G38077.1.

Hubbard, J., Barbot, S., Hill, E. M., and Tapponnier, P. (2015). “Coseismic slip on shallow décollement megathrusts: implications for seismic and tsunami hazard”. *Earth-Science Reviews* 141, pp. 45–55. DOI: 10.1016/j.earscirev.2014.11.003.

Hubert-Ferrari, A., Armijo, R., King, G., Meyer, B., and Barka, A. (2002). “Morphology, displacement, and slip rates along the North Anatolian Fault, Turkey”. 107.B10, ETG–9. DOI: 10.1029/2001JB000393.

Hubert-Ferrari, A., Lamair, L., Hage, S., Schmidt, S., Çağatay, M. N., and Avşar, U. (2020). “A 3800 yr paleoseismic record (Lake Hazar sediments, eastern Turkey): Implications for the East Anatolian Fault seismic cycle”. 538, p. 116152. DOI: 10.1016/j.epsl.2020.116152.

Hudnut, K. W., Shen, Z., Murray, M., McClusky, S., King, R., Herring, T., Hager, B., Feng, Y., Fang, P., Donnellan, A., and Bock, Y. (1996). “Co-seismic displacements of the 1994 Northridge, California, Earthquake”. 86.1b, S19–S36.

Huiskamp, G. (1991). “Difference formulas for the surface Laplacian on a triangulated surface”. *J. Comp. Physics* 95.2, pp. 477–496.

Humayon, M., Lillie, R. J., and Lawrence, R. D. (1991). “Structural interpretation of the eastern Sulaiman foldbelt and foredeep, Pakistan”. *Tectonics* 10.2, pp. 299–324.

Jackson, J. and McKenzie, D. (1984). “Active tectonics of the Alpine–Himalayan belt between western Turkey and Pakistan”. 77.1, pp. 185–264. DOI: 10.1111/j.1365-246X.1984.tb01931.x.

Jadoon, I. (1995). “Three Dimensional Geometry of Passive-roof Duplex, Quaternary Transpression, and Hydrocarbon Traps in the Sulaiman Foreland, Pakistan”. *Pakistan Journal of Hydrocarbon Research* 7, pp. 9–29.

Jadoon, I., Lawrence, R., and Lillie, R. (1993). "Evolution of foreland structures: An example from the Sulaiman thrust lobe of Pakistan, southwest of the Himalayas". *Geological Society, London, Special Publications* 74.1, pp. 589–602.

Javed, M. T., Barbot, S., Javed, F., Ali, A., and Braitenberg, C. (2022). "Coseismic Folding During Ramp Failure at the Front of the Sulaiman Fold-and-Thrust Belt". *Geophysical Research Letters* 49.23, e2022GL099953.

Johanson, I. A. and Bürgmann, R. (2010). "Coseismic and postseismic slip from the 2003 San Simeon earthquake and their effects on backthrust slip and the 2004 Parkfield earthquake". 115.B07411, p. 18.

Johnson, K. M. (2018). "Growth of fault-cored anticlines by flexural slip folding: Analysis by boundary element modeling". 123.3, pp. 2426–2447. DOI: 10.1002/2017JB014867.

Johnson, K. M. and Johnson, A. M. (2002). "Mechanical models of trishear-like folds". *Journal of Structural Geology* 24.2, pp. 277–287. DOI: 10.1016/S0191-8141(01)00062-1.

Jolivet, L., Faccenna, C., Huet, B., Labrousse, L., Le Pourhiet, L., Lacombe, O., Lecomte, E., Burov, E., Denèle, Y., Brun, J.-P., et al. (2013). "Aegean tectonics: Strain localisation, slab tearing and trench retreat". 597, pp. 1–33. DOI: 10.1016/j.tecto.2012.06.011.

Jolivet, R., Lasserre, C., Doin, M.-P., Guillaso, S., Peltzer, G., Dailu, R., Sun, J., Shen, Z.-K., and Xu, X. (2012). "Shallow creep on the Haiyuan Fault (Gansu, China) revealed by SAR Interferometry". 117.B06401, p. 18. DOI: 10.1029/2011JB008732.

Jonsson, P. and Eklundh, L. (2002). "Seasonality extraction by function fitting to time-series of satellite sensor data". *IEEE transactions on Geoscience and Remote Sensing* 40.8, pp. 1824–1832.

Jonsson, S., Segall, P., Pedersen, R., and Bjornsson, G. (2003). "Post-earthquake ground movements correlated to pore-pressure transients". *Nature* 424, pp. 179–183.

Jónsson, S., Zebker, H., Segall, P., and Amelung, F. (2002). "Fault slip distribution of the 1999 M w 7.1 Hector Mine, California, earthquake, estimated from satellite radar and GPS measurements". 92.4, pp. 1377–1389. DOI: 10.1785/0120000922.

Kaneko, Y., Hamling, I., Van Dissen, R., Motagh, M., and Samsonov, S. (2015). "InSAR imaging of displacement on flexural-slip faults triggered by the 2013 Mw 6.6 Lake Grassmere earthquake, central New Zealand". 42.3, pp. 781–788. DOI: 10.1002/2014GL062767.

Karaca, S. O., Abir, I. A., Khan, S. D., Ozsayın, E., and Qureshi, K. A. (2021). "Neotectonics of the Western Suleiman Fold Belt, Pakistan: evidence for bookshelf faulting". *Remote Sensing* 13.18, p. 3593.

Kastelic, V. and Carafa, M. M. (2012). "Fault slip rates for the active External Dinarides thrust-and-fold belt". *Tectonics* 31.3. DOI: 10.1029/2011TC003022.

Khan, N. and Scarselli, N. (2021). "Seismostratigraphic architecture of the sulaiman fold-thrust belt front (Pakistan): Constraints for resource potential of the cretaceous-paleogene strata in the east gondwana fragment". *Journal of Asian Earth Sciences* 205, p. 104598.

King, G. and Nábělek, J. (1985). "Role of fault bends in the initiation and termination of earthquake rupture". *Science* 228.4702, pp. 984–987.

Knospe, S. and Jonsson, S. (2009). "Covariance estimation for dInSAR surface deformation measurements in the presence of anisotropic atmospheric noise". *IEEE Transactions on Geoscience and Remote Sensing* 48.4, pp. 2057–2065.

Konca, A. Ö., Karabulut, H., Güvercin, S. E., Eskiköy, F., Özarpacı, S., Özdemir, A., Floyd, M., Ergintav, S., and Doğan, U. (2021). "From interseismic deformation with near-repeating earthquakes to co-seismic rupture: A unified view of the 2020 Mw 6. 8 Sivrice (Elazığ) Eastern Turkey earthquake". 126.10, e2021JB021830. DOI: 10.1029/2021JB021830.

Kopp, H. and Kukowski, N. (2003). "Backstop geometry and accretionary mechanics of the Sunda margin". *Tectonics* 22.6.

Kuo, Y.-T., Ayoub, F., Leprince, S., Chen, Y.-G., Avouac, J.-P., Shyu, J. B. H., Lai, K.-Y., and Kuo, Y.-J. (2014). "Coseismic thrusting and folding in the 1999 Mw 7.6 Chi-Chi earthquake: A high-resolution approach by aerial photos taken from Tsaotun, central Taiwan". 119.1, pp. 645–660. DOI: 10.1002/2013JB010308.

Lai, K.-Y., Chen, Y.-G., Hung, J.-H., Suppe, J., Yue, L.-F., and Chen, Y.-W. (2006). "Surface deformation related to kink-folding above an active fault: Evidence from geomorphic features and co-seismic slips". *Quaternary International* 147.1, pp. 44–54.

Lapusta, N. and Rice, J. R. (2003). "Nucleation and early seismic propagation of small and large events in a crustal earthquake model". 108.B4, 2205. DOI: 10.1029/2001JB000793.

Lavé, J. and Avouac, J.-P. (2000). "Active folding of fluvial terraces across the Siwaliks Hills, Himalayas of central Nepal". 105.B3, pp. 5735–5770.

Lawrence, R. D. and Yeats, R. S. (1979). "Geological reconnaissance of the Chaman Fault in Pakistan". *Geodynamics of Pakistan*, pp. 351–357.

Lazeckỳ, M., Spaans, K., González, P. J., Maghsoudi, Y., Morishita, Y., Albino, F., Elliott, J., Greenall, N., Hatton, E., Hooper, A., et al. (2020). "LiCSAR: An automatic InSAR tool for measuring and monitoring tectonic and volcanic activity". *Remote Sensing* 12.15, p. 2430.

Lentas, K., Di Giacomo, D., Harris, J., and Storchak, D. A. (2019). "The ISC Bulletin as a comprehensive source of earthquake source mechanisms". *Earth System Science Data* 11.2, pp. 565–578.

Li, Z., Elliott, J. R., Feng, W., Jackson, J. A., Parsons, B. E., and Walters, R. J. (2011). "The 2010 MW 6.8 Yushu (Qinghai, China) earthquake: Constraints provided by InSAR and body wave seismology". 116.B10302, p. 16.

Li, Z., Fielding, E. J., Cross, P., and Muller, J.-P. (2006). "Interferometric synthetic aperture radar atmospheric correction: GPS topography-dependent turbulence model". *Journal of Geophysical Research: Solid Earth* 111.B2.

Li, Z., Xu, W., Feng, G., Hu, J., Wang, C., Ding, X., and Zhu, J. (2012). "Correcting atmospheric effects on InSAR with MERIS water vapour data and elevation-dependent interpolation model". *Geophysical journal international* 189.2, pp. 898–910.

Lin, A., Ouchi, T., Chen, A., and Maruyama, T. (2001). "Co-seismic displacements, folding and shortening structures along the Chelungpu surface rupture zone occurred during the 1999 Chi-Chi (Taiwan) earthquake". *Tectonophysics* 330.3-4, pp. 225–244. DOI: 10.1016/S0040-1951(00)00230-4.

Lin, J. and Stein, R. (1989). "Coseismic folding, earthquake recurrence, and the 1987 source mechanism at Whittier Narrows, Los Angeles Basin, California". 94.B7, pp. 9614–9632. DOI: 10.1029/JB094iB07p09614.

Lomax, A. (Mar. 2023). *Precise, NLL-SSST-coherence hypocenter catalog for the 2023 Mw 7.8 and Mw 7.6 SE Turkey earthquake sequence*. DOI: 10.5281/zenodo.7699882. URL: https://zenodo.org/record/7699882#.ZAjBfuzMI-Q.

Mahanjane, E. S. and Franke, D. (2014). "The Rovuma Delta deep-water fold-and-thrust belt, offshore Mozambique". *Tectonophysics* 614, pp. 91–99. DOI: 10.1016/j.tecto.2013.12.017.

Mai, P. M., Aspiotis, T., Aquib, T. A., Cano, E. V., Castro-Cruz, D., Espindola-Carmona, A., Li, B., Li, X., Liu, J., Matrau, R., et al. (2023). "The Destructive Earthquake Doublet of 6 February 2023 in South-Central Türkiye and Northwestern Syria: Initial Observations and Analyses". *The Seismic Record* 3.2, pp. 105–115.

Malinverno, A. and Ryan, W. B. (1986). "Extension in the Tyrrhenian Sea and shortening in the Apennines as result of arc migration driven by sinking of the lithosphere". *Tectonics* 5.2, pp. 227–245. DOI: 10.1029/TC005i002p00227.

Marone, C., Scholz, C. H., and Bilham, R. (1991). "On the mechanics of earthquake afterslip". 96, pp. 8441–8452. DOI: 10.1029/91JB00275.

Mason, D. P. and Little, T. A. (2006). "Refined slip distribution and moment magnitude of the 1848 Marlborough earthquake, Awatere Fault, New Zealand". *New Zealand Journal of Geology and Geophysics* 49.3, pp. 375–382.

Massonnet, D. and Feigl, K. L. (1998). "Radar interferometry and its application to changes in the Earth's surface". *Reviews of geophysics* 36.4, pp. 441–500.

Massonnet, D., Holzer, T., and Vadon, H. (1997). "Land subsidence caused by the East Mesa geothermal field, California, observed using SAR interferometry". *Geophysical research letters* 24.8, pp. 901–904.

Masuti, S., Barbot, S., Karato, S., Feng, L., and Banerjee, P. (2016). "Upper mantle water stratification inferred from the 2012 Mw 8.6 Indian Ocean earthquake". *Nature* 538, pp. 373–377. DOI: 10.1038/nature19783.

Meade, B. J., Klinger, Y., and Hetland, E. A. (2013). "Inference of multiple earthquake-cycle relaxation timescales from irregular geodetic sampling of interseismic deformation". *Bulletin of the Seismological Society of America* 103.5, pp. 2824–2835.

Mei, C., Barbot, S., and Wu, W. (2021). "Period-multiplying cycles at the transition between stick-slip and stable sliding and implications for the Parkfield period-doubling tremors". 48.7, e2020GL091807. DOI: 10.1029/2020gl091807.

Melgar, D., Taymaz, T., Ganas, A., Crowell, B., Öcalan, T., Kahraman, M., Tsironi, V., Yolsal-Çevikbil, S., Valkaniotis, S., Irmak, T. S., Eken, T., Erman, C., Özkan, B., Dogan, A. H., and Altuntaş, C. (Mar. 2023). "Sub- and super-shear ruptures during the 2023 Mw 7.8 and Mw 7.6 earthquake doublet in SE Türkiye". *Seismica* 2.3. DOI: 10.26443/seismica.v2i3.387. URL: https://seismica.library.mcgill.ca/article/view/387.

Mellors, R. J., Magistrale, H., Earle, P., and Cogbill, A. (2004). "Comparison of four moderate-size earthquakes in southern California using seismology and InSAR". *Bulletin of the Seismological Society of America* 94.6, pp. 2004–2014.

Metropolis, N., Rosenbluth, A. W., Rosenbluth, M. N., Teller, A. H., and Teller, E. (1953). "Equation of state calculations by fast computing machines". *The journal of chemical physics* 21.6, pp. 1087–1092.

Miranda, N., Meadows, P., Type, D., and Note, T. (2015). "Radiometric calibration of S-1 Level-1 products generated by the S-1 IPF". *Viewed at https://sentinel.esa. int/documents/247904/685163/S1-Radiometric-Calibration-V1. 0. pdf.*

Moore, M., Anderson, H., and Pearson, C. (2000). "Seismic and geodetic constraints on plate boundary deformation across the northern Macquarie Ridge and southern South Island of New Zealand". *Geophysical Journal International* 143.3, pp. 847–880.

Morishita, Y., Lazecky, M., Wright, T. J., Weiss, J. R., Elliott, J. R., and Hooper, A. (2020). "LiCSBAS: An open-source InSAR time series analysis package integrated with the LiCSAR automated Sentinel-1 InSAR processor". *Remote Sensing* 12.3, p. 424.

Mosegaard, K. and Tarantola, A. (1995). "Monte Carlo sampling of solutions to inverse problems". *Journal of Geophysical Research: Solid Earth* 100.B7, pp. 12431–12447.

Muñoz, N. and Charrier, R. (1996). "Uplift of the western border of the Altiplano on a west-vergent thrust system, northern Chile". *Journal of South American Earth Sciences* 9.3-4, pp. 171–181. DOI: 10.1016/0895-9811(96)00004-1.

Namson, J. and Davis, T. L. (1988). "Seismically active fold and thrust belt in the San Joaquin Valley, central California". *Geological Society of America Bulletin*

100.2, pp. 257–273. DOI: 10.1130/0016-7606(1988)100<0257:SAFATB>2.3.CO;2.

Nanjundiah, P., Barbot, S., and Wei, S. (2020). "Static source properties of slow and fast earthquakes". 125.12, e2019JB019028. DOI: 10.1029/2019JB019028.

Nissen, E., Elliott, J., Sloan, R., Craig, T., Funning, G., Hutko, A., Parsons, B., and Wright, T. (2016). "Limitations of rupture forecasting exposed by instantaneously triggered earthquake doublet". *Nature Geoscience* 9.4, pp. 330–336.

Nocquet, J.-M. (2012). "Present-day kinematics of the Mediterranean: A comprehensive overview of GPS results". 579, pp. 220–242. DOI: 10.1016/j.tecto.2012.03.037.

Okada, Y. (Aug. 1985). "Surface deformation due to shear and tensile faults in a half-space". 75.4, pp. 1135–1154.

Okada, Y. (Apr. 1992). "Internal Deformation Due to Shear and Tensile Faults in a Half-Space". 82, pp. 1018–1040.

Parker, R. L. (1994). *Geophysical inverse theory*. Princeton, N.J.: Princeton University Press.

Peltzer, G., Rosen, P., Rogez, F., and Hudnut, K. (Dec. 1998). "Poro-elastic rebound along the Landers 1992 earthquake surface rupture". 103.B12, pp. 30131–30145.

Pezzo, G., Merryman Boncori, J. P., Atzori, S., Antonioli, A., and Salvi, S. (2014). "Deformation of the western Indian Plate boundary: insights from differential and multi-aperture InSAR data inversion for the 2008 Baluchistan (Western Pakistan) seismic sequence". *Geophysical Journal International* 198.1, pp. 25–39.

Le-Pichon, X. and Kreemer, C. (2010). "The Miocene-to-Present Kinematic Evolution of the Eastern Mediterranean and Middle East and Its Implications for Dynamics". *Annual Review of Earth and Planetary Sciences* 38.1, pp. 323–351. DOI: 10.1146/annurev-earth-040809-152419.

Le-Pichon, X., Şengör, A. C., Kende, J., İmren, C., Henry, P., Grall, C., and Karabulut, H. (2016). "Propagation of a strike-slip plate boundary within an extensional environment: the westward propagation of the North Anatolian Fault". *Canadian Journal of Earth Sciences* 53.11, pp. 1416–1439. DOI: 10.1139/cjes-2015-0129.

Poblet, J. and Lisle, R. J. (2011). "Kinematic evolution and structural styles of fold-and-thrust belts". *Geological Society, London, Special Publications* 349.1, pp. 1–24. DOI: 10.1144/SP349.1.

Pollitz, F. F., Wicks, C., and Thatcher, W. (2001). "Mantle Flow Beneath a Continental Strike-Slip Fault: Postseismic Deformation After the 1999 Hector Mine Earthquake". *Science* 293, pp. 1814–1818.

Pousse-Beltran, L., Nissen, E., Bergman, E. A., Cambaz, M. D., Gaudreau, É., Karasözen, E., and Tan, F. (2020). "The 2020 M w 6.8 Elazığ (Turkey) earthquake reveals rupture behavior of the East Anatolian Fault". 47.13, e2020GL088136. DOI: 10.1029/2020GL088136.

Powali, D., Sharma, S., Mandal, R., and Mitra, S. (2020). "A reappraisal of the 2005 Kashmir (Mw 7.6) earthquake and its aftershocks: Seismotectonics of NW Himalaya". *Tectonophysics* 789, p. 228501.

Prats-Iraola, P., Scheiber, R., Marotti, L., Wollstadt, S., and Reigber, A. (2012). "TOPS interferometry with TerraSAR-X". *IEEE Transactions on geoscience and remote sensing* 50.8, pp. 3179–3188.

Prevot, R., Hatzfeld, D., Roecker, S., and Molnar, P. (1980). "Shallow earthquakes and active tectonics in eastern Afghanistan". *Journal of Geophysical Research: Solid Earth* 85.B3, pp. 1347–1357.

Price, R. (1981). "The Cordilleran foreland thrust and fold belt in the southern Canadian Rocky Mountains". *Geological Society, London, Special Publications* 9.1, pp. 427–448. DOI: 10.1144/GSL.SP.1981.009.01.39.

Qiu, Q., Hill, E. M., Barbot, S., Hubbard, J., Feng, W., Lindsey, E. O., Feng, L., Dai, K., Samsonov, S. V., and Tapponnier, P. (2016). "The mechanism of partial rupture of a locked megathrust: The role of fault morphology". *Geology* 44.10, pp. 875–878. DOI: 10.1130/G38178.1.

Qiu, Q., Barbot, S., Wang, T., and Wei, S. (2020). "Slip complementarity and triggering between the foreshock, mainshock, and afterslip of the 2019 Ridgecrest rupture sequence". DOI: 10.1785/0120200037.

Qiu, Q. and Barbot, S. (2022). "Tsunami excitation in the outer wedge of global subduction zones". *Earth-Science Reviews*, p. 104054. DOI: 10.1016/j.earscirev.2022.104054.

Ragon, T., Simons, M., Bletery, Q., Cavalié, O., and Fielding, E. (2021). "A stochastic view of the 2020 Elazığ Mw 6.8 earthquake (Turkey)". 48.3, e2020GL090704. DOI: 10.1029/2020GL090704.

Reilinger, R., McClusky, S., Vernant, P., Lawrence, S., Ergintav, S., Cakmak, R., Ozener, H., Kadirov, F., Guliev, I., Stepanyan, R., Nadariya, M., Hahubia, G., Mahmoud, S., Sakr, K., ArRajehi, A., Paradissis, D., Al-Aydrus, A., Prilepin, M., Guseva, T., Evren, E., Dmitrotsa, A., Filikov, S. V., Gomez, F., Al-Ghazzi, R., and Karam, G. (2006). "GPS constraints on continental deformation in the Africa-Arabia-Eurasia continental collision zone and implications for the dynamics of plate interactions". 111.B5. DOI: 10.1029/2005JB004051.

Reynolds, K., Copley, A., and Hussain, E. (2015). "Evolution and dynamics of a fold-thrust belt: the Sulaiman Range of Pakistan". *Geophysical Journal International* 201.2, pp. 683–710.

Rollins, C., Avouac, J.-P., Landry, W., Argus, D. F., and Barbot, S. (2018). "Interseismic strain accumulation on faults beneath Los Angeles, California". 123.8, pp. 7126–7150. DOI: 10.1029/2017JB015387.

Ryan, W. B., Carbotte, S. M., Coplan, J. O., O'Hara, S., Melkonian, A., Arko, R., Weissel, R. A., Ferrini, V., Goodwillie, A., Nitsche, F., et al. (2009). "Global multi-resolution topography synthesis". 10.3. DOI: 10.1029/2008GC002332.

Saffer, D. M. and Bekins, B. A. (2002). "Hydrologic controls on the morphology and mechanics of accretionary wedges". *Geology* 30.3, pp. 271–274.

Saif-Ur-Rehman, K. J., Ding, L., Jadoon, I., Baral, U., Qasim, M., and Idrees, M. (2019). "Interpretation of the Eastern Sulaiman fold-and-thrust belt, Pakistan: A passive roof duplex". *Journal of Structural Geology* 126, pp. 231–244. DOI: 10.1016/j.jsg.2019.06.010.

Saif-Ur-Rehman, K. J., Ding, L., Jadoon, I., Idrees, M., and Zaib, M. O. (2020). "Geometry and development of Zindapir Anticlinorium, Sulaiman Range, Pakistan". *Journal of Structural Geology* 131, p. 103932. DOI: 10.1016/j.jsg.2019.103932.

Sambridge, M. and Mosegaard, K. (2002). "Monte Carlo methods in geophysical inverse problems". *Reviews of Geophysics* 40.3, pp. 3–1.

Samsonov, S. and Tiampo, K. (2006). "Analytical optimization of a DInSAR and GPS dataset for derivation of three-dimensional surface motion". *IEEE Geoscience and Remote Sensing Letters* 3.1, pp. 107–111.

Sandwell, D., Mellors, R., Tong, X., Wei, M., and Wessel, P. (2011). "Gmtsar: An insar processing system based on generic mapping tools". *UC San Diego: Library – Scripps Digital Collection*.

Sansosti, E., Berardino, P., Manunta, M., Serafino, F., and Fornaro, G. (2006). "Geometrical SAR image registration". *IEEE Transactions on Geoscience and Remote Sensing* 44.10, pp. 2861–2870.

Sathiakumar, S. and Barbot, S. (2021). "The stop-start control of seismicity by fault bends along the Main Himalayan Thrust". *Communications Earth & Environment* 2.1, pp. 1–11. DOI: 10.1038/s43247-021-00153-3.

Sathiakumar, S., Barbot, S., and J. Hubbard (2020). "Seismic cycles in fault-bend folds". 125.8, e2019JB018557. DOI: 10.1029/2019JB018557.

Savage, J. and Svarc, J. (1997). "Postseismic deformation associated with the 1992 M_w=7.3 Landers earthquake, southern California". 102, pp. 7565–7577.

Savage, J. and Burford, R. (1973). "Geodetic determination of relative plate motion in central California". 78, pp. 832–845.

Segall, P. and Davis, J. L. (1997). "GPS applications for geodynamics and earthquake studies". *Annual Review of Earth and Planetary Sciences* 25.1, pp. 301–336.

Şengör, A., Tüysüz, O., Imren, C., Sakınç, M., Eyidoğan, H., Görür, N., Le-Pichon, X., and Rangin, C. (2005). "The North Anatolian fault: A new look". *Annu.*

Rev. Earth Planet. Sci. 33, pp. 37–112. DOI: 10.1146/annurev.earth.32.101802.120415.

Sepehr, M. and Cosgrove, J. (2004). "Structural framework of the Zagros fold–thrust belt, Iran". *Marine and Petroleum geology* 21.7, pp. 829–843. DOI: 10.1016/j.marpetgeo.2003.07.006.

Shaukat, A. Z., Tahir, M., Iqbal, T., Iqbal, T., and Shah, M. A. (2023). "Seismotectonic Analysis of the 7 October 2021 M w 5.9 Harnai Earthquake, Pakistan". *Bulletin of the Seismological Society of America* 113.2, pp. 636–647.

Shaw, J. H., Connors, C. D., Suppe, J., et al. (2005). *Seismic interpretation of contractional fault-related folds: An AAPG seismic atlas*. Vol. 53. American Association of Petroleum Geologists. ISBN: 9781629810447. DOI: 10.1306/St531003.

Shaw, J. H., Novoa, E., and Connors, C. D. (2004). "Structural controls on growth stratigraphy in contractional fault-related folds". *American Association of Petroleum Geologists*.

Shaw, J. H. and Shearer, P. M. (1999). "An elusive blind-thrust fault beneath metropolitan Los Angeles". *Science* 283.5407, pp. 1516–1518. DOI: 10.1126/science.283.5407.1516.

Shaw, J. H. and Suppe, J. (1994). "Active faulting and growth folding in the eastern Santa Barbara Channel, California". *Geological Society of America Bulletin* 106.5, pp. 607–626. DOI: 10.1130/0016-7606(1994)106<0607:AFAGFI>2.3.CO;2.

Shaw, J. H. and Suppe, J. (1996). "Earthquake hazards of active blind-thrust faults under the central Los Angeles basin, California". 101.B4, pp. 8623–8642. DOI: 10.1029/95JB03453.

Shim, J., Scherliess, L., Schunk, R., and Thompson, D. (2008). "Spatial correlations of day-to-day ionospheric total electron content variability obtained from ground-based GPS". *Journal of Geophysical Research: Space Physics* 113.A9.

Simons, M., Fialko, Y., and Rivera, L. (2002). "Coseismic deformation from the 1999 M_w7.1 Hector Mine, California, earthquake, as inferred from InSAR and GPS observations". 92, pp. 1390–1402.

Stein, S. (1993). "Space geodesy and plate motions". *Contributions of Space Geodesy to Geodynamics: Crustal Dynamics* 23, pp. 5–20.

Suppe, J. (1983). "Geometry and kinematics of fault-bend folding". *Am. J. science* 283.7, pp. 684–721.

Suppe, J. and Medwedeff, D. A. (1990). "Geometry and kinematics of fault-propagation folding". *Eclogae Geologicae Helvetiae* 83.3, pp. 409–454.

Szeliga, W., Bilham, R., Kakar, D. M., and Lodi, S. H. (2012). "Interseismic strain accumulation along the western boundary of the Indian subcontinent". *Journal of Geophysical Research: Solid Earth* 117.B8.

Tanner, P. G. (1989). "The flexural-slip mechanism". *Journal of Structural Geology* 11.6, pp. 635–655. DOI: 10.1016/0191-8141(89)90001-1.

Tapponnier, P., Lacassin, R., Leloup, P., Scharer, U., Dalai, Z., Haisei, W., Ziaohan, L., Shaocheng, J., Lianshang, Z., and Jiayou, Z. (1990). "The Ailao Shan/Red River metamorphic belt: tertiary left-lateral shear between Indochina and South China". *Nature* 343.6257, pp. 431–437.

Tarantola, A. (2005). *Inverse Problem Theory and Methods for Model Parameter Estimation*. Philadelphia, PA, USA: Soc. Ind. App. Math. ISBN: 0898715725.

Tatar, O., Poyraz, F., Gürsoy, H., Cakir, Z., Ergintav, S., Akpınar, Z., Koçbulut, F., Sezen, F., Türk, T., Hastaoğlu, K. Ö., et al. (2012). "Crustal deformation and kinematics of the Eastern Part of the North Anatolian Fault Zone (Turkey) from GPS measurements". 518, pp. 55–62. DOI: 10.1016/j.tecto.2011.11.010.

Tatar, O., Sözbilir, H., Koçbulut, F., Bozkurt, E., Aksoy, E., Eski, S., Özmen, B., Alan, H., and Metin, Y. (2020). "Surface deformations of 24 January 2020 Sivrice (Elazığ)–Doğanyol (Malatya) earthquake (Mw= 6.8) along the Pütürge segment of the East Anatolian Fault Zone and its comparison with Turkey's 100-year-surface ruptures". *Mediterranean Geoscience Reviews* 2, pp. 385–410.

Taymaz, T., Ganas, A., Yolsal-Çevikbilen, S., Vera, F., Eken, T., Erman, C., Keleş, D., Kapetanidis, V., Valkaniotis, S., Karasante, I., et al. (2021). "Source mechanism and rupture process of the 24 January 2020 Mw 6.7 Doğanyol–sivrice earthquake obtained from seismological waveform analysis and space geodetic observations on the East Anatolian Fault Zone (Turkey)". *Tectonophysics* 804, p. 228745.

Taymaz, T., Jackson, J., and McKenzie, D. (1991). "Active tectonics of the north and central Aegean Sea". 106.2, pp. 433–490. DOI: 10.1111/j.1365-246X.1991.tb03906.x.

Thatcher, W. (2007). "Microplate model for the present-day deformation of Tibet". *Journal of Geophysical Research: Solid Earth* 112.B1.

Thatcher, W. (2009). "How the continents deform: The evidence from tectonic geodesy". *Annual Review of Earth and Planetary Sciences* 37, pp. 237–262.

Tsang, L. L., Hill, E. M., Barbot, S., Qiu, Q., Feng, L., Hermawan, I., Banerjee, P., and Natawidjaja, D. H. (2016). "Afterslip following the 2007 Mw 8.4 Bengkulu earthquake in Sumatra loaded the 2010 Mw 7.8 Mentawai tsunami earthquake rupture zone". *Journal of Geophysical Research: Solid Earth* 121.12, pp. 9034–9049.

Tsuji, T., Ashi, J., and Ikeda, Y. (2014). "Strike-slip motion of a mega-splay fault system in the Nankai oblique subduction zone". 66.1, p. 120.

USGS (2020). "United States Geological Survey, Earthquake Lists, Maps, and Statistics, accessed March 18, 2020". *USGS*. URL: https://doi.org/10.1093/biomet/57.1.97.

Usman, M. and Furuya, M. (2015). "Complex faulting in the Quetta Syntaxis: fault source modeling of the October 28, 2008 earthquake sequence in Baluchistan, Pakistan, based on ALOS/PALSAR InSAR data". *Earth, Planets and Space* 67.1, pp. 1–11.

Vernant, P., Nilforoushan, F., Hatzfeld, D., Abbassi, M., Vigny, C., Masson, F., Nankali, H., Martinod, J., Ashtiani, A., Bayer, R., et al. (2004). "Present-day crustal deformation and plate kinematics in the Middle East constrained by GPS measurements in Iran and northern Oman". 157.1, pp. 381–398. DOI: 10.1111/j.1365-246X.2004.02222.x.

Von Huene, R., Kulm, L., and Miller, J. (1985). "Structure of the frontal part of the Andean convergent margin". 90.B7, pp. 5429–5442. DOI: 10.1029/JB090iB07p05429.

Wackernagel, H. (2003). "Variogram and covariance function". In: *Multivariate Geostatistics*. Springer, pp. 50–56.

Walters, R. J., Holley, R. J., Parsons, B., and Wright, T. J. (2011). "Interseismic strain accumulation across the North Anatolian Fault from Envisat InSAR measurements". 38.L05303, p. 5. DOI: 10.1029/2010GL046443.

Wang, B., Zhao, C., Zhang, Q., Yang, C., Li, W., Li, G., Kang, Y., and Zheng, S. (2023). "SAR Interferometry Infrastructure Deformation Monitoring by the Number of Redundant Observations Optimizes Phase Unwrapping Networks". *IEEE Journal of Selected Topics in Applied Earth Observations and Remote Sensing*.

Wang, H., Liu-Zeng, J., Ng, A.-M., Ge, L., Javed, F., Long, F., Aoudia, A., Feng, J., and Shao, Z. (2017). "Sentinel-1 observations of the 2016 Menyuan earthquake: A buried reverse event linked to the left-lateral Haiyuan fault". *International Journal of Applied Earth Observation and Geoinformation* 61, pp. 14–21.

Wang, L. (2018). "The Next M~6 Event in Parkfield Implied by a Physical Model Linking Interseismic, Coseismic, and Postseismic Phase". 123.10, pp. 8858–8873. DOI: 10.1029/2018JB015493.

Wang, T., Jónsson, S., and Hanssen, R. F. (2014). "Improved SAR image coregistration using pixel-offset series". *IEEE geoscience and remote sensing letters* 11.9, pp. 1465–1469. DOI: 10.1109/LGRS.2013.2295429.

Wang, T., Shi, Q., Nikkhoo, M., Wei, S., Barbot, S., Dreger, D., Bürgmann, R., Motagh, M., and Chen, Q.-F. (2018). "The rise, collapse, and compaction of Mt. Mantap from the 3 September 2017 North Korean nuclear test". *Science*, eaar7230. DOI: 10.1126/science.aar7230.

Wang, X., Wei, S., and Wu, W. (2017). "Double-ramp on the Main Himalayan Thrust revealed by broadband waveform modeling of the 2015 Gorkha earthquake sequence". 473, pp. 83–93.

Weertman, J. (1966). "Rate of growth of fatigue cracks calculated from the theory of infinitesimal dislocations distributed on a plane". *International Journal of Fracture Mechanics* 2.2, pp. 460–467.

Wei, S., Helmberger, D., and Avouac, J.-P. (2013). "Modeling the 2012 Wharton basin earthquakes off-Sumatra: Complete lithospheric failure". 118.7, pp. 3592–3609.

Weng, H. and Yang, H. (2017). "Seismogenic width controls aspect ratios of earthquake ruptures". 44.6, pp. 2725–2732. DOI: 10.1002/2016GL072168.

Wesnousky, S. G. (2006). "Predicting the endpoints of earthquake ruptures". *Nature* 444.7117, pp. 358–360. DOI: 10.1038/nature05275.

Wessel, P. and Luis, J. F. (2017). "The GMT/MATLAB Toolbox". *Geochemistry, Geophysics, Geosystems* 18.2, pp. 811–823. DOI: 10.1002/2016GC006723.

Wessel, P., Smith, W. H. F., Scharroo, R., Luis, J., and Wobbe, F. (2013). "Generic Mapping Tools: Improved Version Released". *Eos, Transactions American Geophysical Union* 94.45, pp. 409–410. DOI: 10.1002/2013EO450001.

Weston, J., Ferreira, A. M., and Funning, G. J. (2012). "Systematic comparisons of earthquake source models determined using InSAR and seismic data". *Tectonophysics* 532, pp. 61–81.

Wright, T., Parsons, B., and Fielding, E. (2001). "Measurement of interseismic strain accumulation across the North Anatolian Fault by satellite radar interferometry". 28.10, pp. 2117–2120. DOI: 10.1029/2000GL012850.

Xu, W., Feng, G., Meng, L., Zhang, A., Ampuero, J. P., Bürgmann, R., and Fang, L. (2018). "Transpressional rupture cascade of the 2016 Mw 7.8 Kaikoura earthquake, New Zealand". *Journal of Geophysical Research: Solid Earth* 123.3, pp. 2396–2409.

Xu, X., Wen, X., Han, Z., Chen, G., Li, C., Zheng, W., Zhnag, S., Ren, Z., Xu, C., Tan, X., et al. (2013). "Lushan Ms 7.0 earthquake: a blind reserve-fault event". *Chinese Science Bulletin* 58.28, pp. 3437–3443.

Yadav, R. K., Kundu, B., Gahalaut, K., Catherine, J., Gahalaut, V. K., Ambikapthy, A., and Naidu, M. (2013). "Coseismic offsets due to the 11 April 2012 Indian Ocean earthquakes (Mw 8.6 and 8.2) derived from GPS measurements". *Geophysical Research Letters* 40.13, pp. 3389–3393.

Yassaghi, A. and Marone, C. (2019). "The relationship between fault zone structure and frictional heterogeneity, insight from faults in the High Zagros". 762, pp. 109–120.

Yu, C., Li, Z., and Penna, N. T. (2018a). "Interferometric synthetic aperture radar atmospheric correction using a GPS-based iterative tropospheric decomposition model". *Remote Sensing of Environment* 204, pp. 109–121. DOI: 10.1016/j.rse.2017.10.038.

Yu, C., Li, Z., Penna, N. T., and Crippa, P. (2018b). "Generic atmospheric correction model for interferometric synthetic aperture radar observations". *Journal of Geophysical Research: Solid Earth* 123.10, pp. 9202–9222.

Yue, L., Suppe, J., and Hung, J.-H. (2005). "Structural geology of a classic thrust belt earthquake: the 1999 Chi-Chi earthquake Taiwan (M_w 7.6)". *J. Struct. Geol.* 27, pp. 2058–2083.

Yule, D. and Sieh, K. (2003). "Complexities of the San Andreas fault near San Gorgonio Pass: Implications for large earthquakes". *Journal of Geophysical Research: Solid Earth* 108.B11.

Yunjun, Z., Fattahi, H., and Amelung, F. (2019). "Small baseline InSAR time series analysis: Unwrapping error correction and noise reduction". *Computers & Geosciences* 133, p. 104331.

Zebker, H. A. and Goldstein, R. M. (1986). "Topographic mapping from interferometric synthetic aperture radar observations". *Journal of Geophysical Research: Solid Earth* 91.B5, pp. 4993–4999.

Zebker, H. A., Rosen, P. A., Goldstein, R. M., Gabriel, A., and Werner, C. L. (1994). "On the derivation of coseismic displacement fields using differential radar interferometry: The Landers earthquake". *Journal of Geophysical Research: Solid Earth* 99.B10, pp. 19617–19634.

Zebker, H. A., Rosen, P. A., and Hensley, S. (1997). "Atmospheric effects in interferometric synthetic aperture radar surface deformation and topographic maps". *Journal of geophysical research: solid earth* 102.B4, pp. 7547–7563.

Zebker, H. A. and Villasenor, J. (1992). "Decorrelation in interferometric radar echoes". 30.5, pp. 950–959.

Zhou, L., Yu, H., and Lan, Y. (2020). "Deep convolutional neural network-based robust phase gradient estimation for two-dimensional phase unwrapping using SAR interferograms". *IEEE Transactions on Geoscience and Remote Sensing* 58.7, pp. 4653–4665.

Zilio, D. L. and Ampuero, J. (2023). "Earthquake doublet in Turkey and Syria". *Comm. Earth Environ* 4.71. DOI: 10.1038/s43247-023-00747-z.

Zink, M. (2002). "Introduction to the ASAR calibration/validation project". *Envisat Calibration Review*.

List of Figures

2.1 The launched and proposed SAR satellite missions operating using different frequencies of microwaves. We specifically used the C-band (5.3 GHz) Sentinel-1A/1B and the L-band (1.2 GHz) ALOS-2 satellites (https://detektia.com/en/sar-synthetic-aperture-radar/). 7

2.2 Sentinel-1 satellite acquisition modes. The acquisition difference of Extra Wide swath (EW), Strip map (SM), Interferometric Wide (IW) and, Wave (WV) of the Seintinel-1 satellite. The image modified from (https://sentinels.copernicus.eu/web/sentinel/missions/sentinel-1/instrument-payload). . . . 8

2.3 Sentinel-1 TOPS mode acquisition in subwath 1, 2 and 3 with burst 1, 2, and 3 along with burst overlap (Grandin et al., 2016). 8

2.4 SAR image of Sentinel-1 satellite showing the backscattered signal on the Sulaiman Fold and thrust (SFT) belt at the Indian-Eurasian plates boundary zone. The bright pixels indicate the exposed rocks while the dark pixels indicate the vegetation, trees, and flat surfaces as lakes. 10

2.5 Effect of topography on SAR image acquisition. (a) Slant range resolution is affected by topographic gradient. (b) The positive topographic gradient incorporates the layover effect and the negative gradient produces a shadow zone (Ferretti et al., 2007). 12

2.6 Scketch of Synthetic Aperture Radar (SAR) antennas mounted on the Radar which record backscattered signals on multiple positions along the flight direction of the satellite. Here ρ is the distance between the illuminted targeted ground surface and the antenna, ε is half illuminated ground length, and ϑ is the pulse angle (Ferretti et al., 2007). 12

2.7 The geometry of InSAR satellites used to obtain an interferogram using two SAR satellites to monitor the surface deformation along the line-of-sight direction (Besoya et al., 2021; Ferretti et al., 2007). 14

2.8 The contribution of topographic noise in the velocity inferred from Sentinel-1A time series from 30 October 2020 to 30 November 2021 at the central SFT zone in the descending track T078. The GACOS corrections are already applied to remove the stratified atmospheric noise that correlates with topography. The black rectangle shows the deformation produced by the 2021 Mw 6.0 earthquake at the western SFT zone. 16
2.9 The contribution of atmospheric and significant ionospheric noise in an interferogram produced using L-band ALOS-2 ScanSAR data from 29 September 2021 to 10 October 2021 at the western SFT zone. The black rectangle shows the deformation produced by the 2021 Mw 6.0 earthquake at the western SFT zone. . . . 17
2.10 . The different stages of a fault behavior during an earthquake cycle. Space geodesy provides great insights to understand the distinct phenomena occurring during interseismic, coseismic, and postseismic phases. 20
2.11 Space geodetic revolution helps us to monitor the behavior of faults and measure time-dependent parameters of deformation to insight into the entire earthquake cycle. Coseismic deformation occurs over a fault in the seismogenic crust. Postseismic deformation in the form of shallow and deep after-slip started shortly after an earthquake. The shallow after-slip occurs in the brittle upper crust, and the deep after-slip occurs in the ductile lower crust and upper mantle. Interseismic strain accumulates across the fault zone for the rest of the period of the earthquake cycle. The figure is modified from (Elliott et al., 2016) 21
2.12 A sketch of an entire earthquake cycle including, coseismic ($T = 0$), postseismic ($T > 0$), and interseismic ($T >> 0$) phases in the thrust and extensional regimes. Star indicates the hypocentral location of a presumed earthquake, $T = 0$ represents the time earthquake nucleation. The figure is modified from (Albano et al., 2021) 22

3.1 Tectonic settings and historical earthquakes (yellow circles) with M>3.5 on SFT belt. a) Faults abbreviated with BT – boundary thrust, CF – Chaman Fault, GBF – Ghazaband Fault, KF – Kingri Fault, KT – Kamari Thrust, KHT – Karahi Thrust (Pezzo et al., 2014). Focal mechanism solutions in blue (Nissen et al., 2016), orange (Pezzo et al., 2014), GCMT catalog, dark gray (Reynolds et al., 2015), black (Bernard et al., 2000), and white circles (Ambraseys and Bilham, 2003). The dark red moment tensor is the 2015 Dajal earthquake epicenter, shown above the slip distribution. The inset shows the geographical location of the SFT belt and the relative motion (36 mm/yr) between the India and the Afghan block (Ul-Hadi et al., 2013). b) and c) Ascending and descending, wrapped LOS displacement of the 2015 Dajal earthquake. 25

3.2 LOS displacement for ascending (a-e), and descending (f) tracks, calculated using Sentinel-1A interferograms for time couples before, after, and across the 2015 Dajal earthquake of 23 October 2015. 28

3.3 The adaptive quadtree gradient-based subsampling and semi-variogram analysis. a, b) The subsampling and semi-variogram to estimate the covariance of the processed interferogram during ascending track respectively. The ascending interferogram is subdivided into 238 points with the threshold variance of 1.0×10^{-2} mm^2. c, d) The subsampling and semi-variogram to estimate the covariance of the processed interferogram during descending track respectively. The descending interferogram is subdivided into 178 points with the threshold variance of 4.5×10^{-2} mm^2. Blue (solid lines) is the exponential function of the semivariogram while Red (blocks) is the experimental semi-variogram. The local origin for both interferograms is 70.289°E and 29.662°N. 30

3.4 Histograms of source fault model parameters through Bayesian inversion approach with 10^6 samples, on wider area of 0.6° x 0.6°. The y-axis represents the probability density, and the red line indicates the optimal model values with 95% confidence interval for GACOS corrected data. (Rejected solution). 31

3.5 Histograms of source fault model parameters through Bayesian inversion approach with 10^6 samples, on area of 0.2° x 0.2°. The y-axis represents the probability density, and the red line indicates the optimal model values with 95% confidence interval. The optimal model has fault length around 15 km, width 2.9 km, depth 6.5 km, dip 40°, strike 194°, and average slip 0.28 m. (Best solution). 32
3.6 Single fault plane solution by using GBIS approach a, b) observation, c, d) synthetic interferogram and e, f) residual of the ascending track (T071) and descending track (T005) respectively. The deformation along the LOS displacement is approximately 50 mm and 45 mm along with less than 2.3 mm residual for descending and ascending track respectively. The focal mechanism solution (red colored) is produced by using inverted ruptured fault parameters and the focal mechanism solution (black colored) is taken from USGS. 33
3.7 End-member models of fault-related folds in a representative cross-section. a) Double FBF model with syncline and anticlinal fault bends and active axial surfaces. b) Long-term slip directions along the décollement, ramp, and axial surfaces. The three velocity vectors close the hodograph (inset). Flexural slip on axial surfaces accommodates the advection of thrusted sediments as they start or stop climbing the ramp. The unit vector **n** is normal to the axial surface. c) FPF with four active axial surfaces (long dashed lines). The domains surrounded by active axial surface move at the same long-term velocity. The passive axial surface (short dashed line) does not contribute to internal deformation. d) Relative motion along the top axial surfaces 3 and 4 of the fault-propagation fault model closing the hodographs (inset). The end-member models are extruded along a 194° strike to form a three-dimensional structure for the purpose of inversion. 35
3.8 Kinematic models of the Mw 5.7 Dajal earthquake for two-end member fault-related fold geometries and two vergence directions. a, c) Forward- and backward-vergent FBF coseismic slip distribution on the décollement-ramp-décollement system and flexural slip on two axial surfaces. b, d) Forward- and backward-vergent FPF coseismic slip distribution on the décollement-ramp system and flexural slip on four active axial surfaces. 38

3.9 The FBF, and FPF model solutions a, f) ascending and descending InSAR observations, b - i) Ascending and descending backward-vergent fault-bend fold and fault-propagation fold models and residuals, k - r) Ascending and descending forward-vergent fault-bend fold and fault-propagation fold models and residuals. The maximum coseismic slip along the LOS displacement is approximately 50 mm along with less than 2.8 mm residual for descending and ascending track respectively. Focal mechanism solution (red colored) is produced by using inverted ruptured fault parameters and focal mechanism solution (black colored) is taken from USGS. 39

3.10 Model comparison. a) Forward-vergent FPF models for ascending and descending InSAR tracks. b) Forward-vergent FBF models during ascending and descending InSAR tracks. Focal mechanisms based on InSAR (red) or from USGS (black). c) Tradeoff between data misfit and model roughness (L-curve) for forward- and backward-vergent FBF and FPF models. The black and red color circles show selected smoothing factors for the FBF and FPF models, 0.06, and 0.05, respectively. 41

3.11 Blind frontal ramp of the Eastern SFT. a) The dashed line with chevron is the proposed extension of the BT south of the Zindapir anticlinorium and the Sakhi Sarwar anticline without surface expression. The ramp is buried under recent sediments from the Indus River flood plain, 30 km east of the Eastern SFT. b, c) Cross-sections of FBF and FPF geometries across the Dajal earthquake epicentral area with a FPF extending from the southern extension of the BT buried under Miocene or younger sediments. The colors indicate the concentration of slip on the ramp and flexural slip along the active axial surface. Vertical exaggeration (x1). 45

4.1 Tectonic settings and historical earthquakes (yellow circles) with M>3.5 on SFT belt. a) Faults abbreviated with BT – boundary thrust, CF – Chaman Fault, GBF – Ghazaband Fault, KF – Karahi Fault, KT – Kamari Thrust, HF – Harnai Fault (Pezzo et al., 2014). Focal mechanism solutions in blue (Nissen et al., 2016), orange (Pezzo et al., 2014), GCMT catalog, dark gray (Reynolds et al., 2015), black (Bernard et al., 2000), and white circles (Ambraseys and Bilham, 2003). The black-colored beach solution in a blue rectangle is produced by using inverted fault model parameters of the 2021 Mw 6.0 Harnai earthquake. The inset shows the geographical location of the SFT belt and the relative motion (36 mm/yr) between India and the Afghan block (Ul-Hadi et al., 2013). 50
4.2 Network of ascending (AT144) and descending (DT78) track interferograms used for the SBAS time series analysis with the LiCSBAS software. 52
4.3 Comparison of using single pair of interferograms and multiple pairs of interferograms of ascending and descending tracks to estimate coseismic deformation of the 2021 Mw 6.0 Harni earthquake (a, b) Coseismic deformation obtained through GMTSAR software using a single pair of interferograms. (c, d) Coseismic deformation obtained through SBAS time series in LiCSBAS software using multiple pairs of interferograms. KF – right lateral Karahi Fault, HF – thrusting Harnai Fault 53
4.4 Subsampling of ascending (AT144) and descending (DT78) track interferograms using Bayesian inversion. 55
4.5 Uniform fault plane solution obtained NW-SE trending model by using GBIS approach a, b) observation, c, d) synthetic interferogram and e, f) residual of the ascending track (AT144) and descending track (DT78) respectively. The deformation along the LOS displacement is approximately 70 mm and 80 mm. The focal mechanism solution (black colored) is produced by using inverted ruptured NW-SE trending model. 58
4.6 Histograms of NW-SE trending ruptured fault model parameters through Bayesian inversion approach with 10^7 samples. The y-axis represents the probability density, and the red line indicates the optimal model values with 95% confidence interval 58
4.7 Convergence of NW-SE trending ruptured fault model parameters through Bayesian inversion approach with 10^7 samples. The y-axis represents the range of fault parameters, while the x-axis shows the number of samples used in the inversions. . . 59

4.8 Uniform fault plane solution obtained NE-SW trending model by using GBIS approach a, b) observation, c, d) synthetic interferogram and e, f) residual of the ascending track (AT144) and descending track (DT78) respectively. The deformation along the LOS displacement is approximately 70 mm and 80 mm. The focal mechanism solution (black colored) is produced by using an inverted ruptured NW-SE trending model. 60
4.9 Histograms of NE-SW trending ruptured fault model parameters through Bayesian inversion approach with 10^7 samples. The y-axis represents the probability density, and the red line indicates the optimal model values with 95% confidence interval 61
4.10 The kinematic finite slip surface deformation models obtained from the NW-SE trending rupture of the 2021 Mw 6.0 Harnai earthquake. (a, d) Ascending and descending InSAR observations. (b, e) Ascending and descending synthetic models. (c, f) Ascending and descending residuals, respectively. The maximum of co-seismic deformation along the LOS displacement is around 70 mm, and 80 mm along the line-of-sight direction with less than 6 mm residual for both ascending and descending interferograms respectively. Focal mechanism obtained from Bayesian inversions using NW-SE trending rupture fault model. 63
4.11 Kinematic rupture model of the Mw 6.0 Harnai earthquake (a) 3D coseismic slip distribution on the NW-SE trending rupture model estimated from Bayesian inversion. (b) 2D coseismic slip distribution along the dip and strike of the NW-SE trending fault. 64
4.12 The kinematic finite slip surface deformation models obtained from NE-SW trending rupture of 2021 Mw 6.0 Harnai earthquake. (a, d) Ascending and descending InSAR observations. (b, e) Ascending and descending synthetic models. (c, f) Ascending and descending residuals, respectively. The maximum LOS displacement is 70 mm, and 80 mm in the ascending and descending interferograms respectively. Focal mechanism obtained from Bayesian inversions using NE-SW trending rupture fault model. 65
4.13 Kinematic rupture model of the Mw 6.0 Harnai earthquake (a) 3D coseismic slip distribution on the NE-SW trending rupture model estimated from Bayesian inversion. (b) 2D coseismic slip distribution along the dip and strike of the NE-SW trending fault. 66

4.14 Slip rates of ascending track AT144 between December 2020 to December 2022. (a) Positive velocity is the movement towards the satellite, negative velocity is the movement away from the satellite. Beach ball solution of the 2021 Mw 6.0 earthquake. (b) The creep rate across the profile AA' and the black dashed line shows the Harnai fault. (c and d) Pre-seismic, post-seismic, and co-seismic displacement of the Mw 6.0 2021 Harnai earthquake on points P1, and P2. The red dots show the interferograms. The green colored line shows the co-seismic movement due to the Mw 6.0 earthquake. 70

4.15 Slip rates of descending track DT78 between December 2020 to December 2022. (a) Positive velocity is the movement toward the satellite, negative velocity is the movement away from the satellite. Beach ball solution of the 2021Mw 6.0 earthquake. (b) The creep rate across the profile AA' and the black dashed line shows the Harnai fault. (c and d) Pre-seismic, post-seismic, and co-seismic displacement of the Mw 6.0 2021 Harnai earthquake on points P1, and P2. The red dots show the interferograms. The green colored line shows the co-seismic movement due to the Mw 6.0 earthquake. 71

5.1 Simplified tectonic map of the East Anatolian Fault Zone after Duman and Emre, 2013 and Emre et al., 2018. The East Anatolian Fault consists of a succession of discontinuous segments. The 2023 Mw 7.8 mainshock ruptured the Amanos, Pazarcık, and Erkenek segments and stopped at the Yarpuzlu restraining bend. The Mw 7.6 aftershock ruptured the Savrun Fault, the Çardak Fault, and propagated toward Malataya along a structure between the Sürgü Fault and the Malatya Fault. Fault is abbreviated to "F." to save space. The February 20, 2023 Mw 6.4 aftershock took place near the Antakya Fault towards the Mediterranean Basin. The background seismicity also mentioned in (Figure 5.2b) represents the aftershocks within 2 days of the mainshock (Lomax, 2023). 76

5.2 Tectonic setting and crustal deformation of the East Anatolian Fault (EAF) on February 6, 2023. a) The aftershocks (black dots) (Lomax, 2023) and the focal mechanisms of earthquakes of moment magnitude greater than 4 (beach balls) illuminate the ruptures of the Kahramanmaraş Mw 7.8 (purple) and the Elbistan Mw 7.6 (blue) earthquakes. The fault offsets indicate the extent of the ruptures. The EAF and Dead Sea (DSF), plate-boundary faults, are shown in red. Major and minor faults are shown in thick and thin black lines, respectively (Emre et al., 2018). The focal mechanisms are from the Disaster and Emergency Management Authority (AFAD) for February 6, 2023 (`https://deprem.afad.gov.tr/event-catalog`). The topography is from the Global Multi-Resolution Topography Synthesis (GMRT) (Ryan et al., 2009). b) Time series of aftershocks magnitude in the days following the mainshock (purple for aftershocks within 20 km of the EAF, blueish for aftershocks within 20 km of the Mw 7.6 rupture, and orange for earthquakes within 20 km of the Mw 6.4 Antakya aftershock). The February 20, 2023 Mw 6.4 aftershock occurs at the southern termination of the EAF. 78

5.3 Sentinel-1 unwrapped interferograms of the February 20, 2023 Mw 6.4 aftershock near Antakya, Turkey. a) Interferogram of ascending track AT14, based on SAR images acquired on February 9, 2023 and February 21 2023. b) Interferogram of descending track DT21 based on SAR images acquired on February 10, 2023 and February 22, 2023. The dashed rectangle indicates the region most affected by crustal deformation. 82

5.4 Subsampling of ascending (AT014) and descending (DT021) tracks interferograms before inverting LOS displacement. . . 84

5.5 Histograms of ruptured fault model parameters through Bayesian inversion approach with 10^6 samples. The y-axis represents the probability density, and the red line indicates the optimal model values with 95% confidence interval 84

5.6 Convergence of ruptured fault model parameters through Bayesian inversion approach with 10^6 samples. The y-axis represents the range of fault parameters, while the x-axis shows the number of samples used in the inversions. 85

5.7 Trade-off between roughness and residuals for the Mw 6.4 Antakya aftershock. 85

5.8 Comparison between Sentinel-1 interferogram and the deformation predicted by the slip distribution of the Mw 6.4 Antakya aftershock. a, b, c) Data, forward model, and residuals for the ascending track 14 interferogram. d, e, f) Same for the descending track 21 interferogram. The line-of-sight direction is indicated by the black arrow. The fault geometry (black patches) is broadly aligned with the Antakya Fault. 87
5.9 Coseismic slip distribution of a) the 2023 February 06, Mw 7.8 Kahramanmaraş mainshock, the February 20, Mw 6.4 aftershocks (purple), and the 2020 Mw 6.8 Elazığ earthquake (Pousse-Beltran et al., 2020) (light brown) and b) the 2023 February 6, Mw 7.6 Elbistan aftershock. The maximum slip of 8 m on the EAF concentrates between 3 and 7 km depth, highlighting a shallow slip deficit. The maximum slip on the Çardak fault during the Mw 7.6 aftershock is 11 m from the surface to 7 km depth. The small-magnitude aftershocks (Lomax, 2023) concentrate at segment boundaries and around the regions of high coseismic slip. 89
5.10 Shallow slip deficit and potential seismic gap along the Pütürge segment. a) Coseismic slip distribution of the 2023 February 6, Mw 7.8 Kahramanmaraş mainshock with peak slip between 6 and 8 km depth. b) Coseismic slip distribution of the Mw 7.8 mainshock in relation to the 2020 Mw 6.8 Elazığ earthquake (Pousse-Beltran et al., 2020), highlighting a potential 40 km-long seismic gap in the Pütürge segment. c) Coseismic slip distribution of the 2023 February 6 Mw 7.6 Elbistan aftershock. The aftershocks distribution and the background microseismicity before the respective earthquakes are shown with black and purple dots, respectively. d) Depth distribution of coseismic slip and aftershocks for the Mw 7.8 mainshock, highlighting a shallow slip deficit. The aftershocks concentrate in regions of high gradient of slip. e) Same for the Mw 7.6 aftershock. f) Same for the 2020 Mw 6.8 Elazığ earthquake and its aftershocks. 91
5.11 Network of ascending track (AT116) interferograms used for the SBAS time series analysis with the Mintpy software. . . . 94
5.12 Network of ascending track (AT43) interferograms used for the SBAS time series analysis with the Mintpy software. 94
5.13 Network of descending track (DT21) interferograms used for the SBAS time series analysis with the Mintpy software. . . . 94

5.14 Network of descending track (DT123) interferograms used for the SBAS time series analysis with the LiCSBAS software. . . 95
5.15 The detailed workflow we follow with the Mintpy software to process the time series of the Sentinel-1 geocoded unwrapped interferograms of tracks AT116, AT43, and DT21. The workflow is modified from Yunjun et al. (2019) 95
5.16 Velocity of the track AT116 from 29 January 2020 to 29 January 2023. (a) The velocity or creep rates estimated through SBAS time series analysis on the East Anatolian Fault (EAF) system. The velocity is estimated with reference to a stable pixel that exhibits a minimum 90% coherence shown by a light blue rectangle. The velocity shows a left lateral movement of the fault, the positive velocity shows the movement towards the satellite while negative velocity shows the movement away from the satellite. The focal mechanism solutions of the 2020 Mw 6.8 Elazığ, the 2023 Mw 7.8 Kahramanmaraş, and the 2023 Mw 7.6 Elbistan earthquakes are plotted. (b), and (c) The velocities on profiles BB' and CC' across the EAF system. The velocity jump can be seen across the EAF segments. (d) and (e) Time series movement in the line-of-sight direction on pixels P1 (red hexagon) and P2 (yellow hexagon) respectively. 98
5.17 Velocity of the track DT21 from 29 January 2020 to 29 January 2023. (a) The velocity or creep rates estimated through SBAS time series analysis on the East Anatolian Fault (EAF) system. The velocity is estimated with reference to a stable pixel that exhibits a minimum 90% coherence shown by a light blue rectangle. The velocity shows a left lateral movement of the fault, the positive velocity shows the movement towards the satellite while negative velocity shows the movement away from the satellite. The focal mechanism solutions of the 2020 Mw 6.8 Elazığ, the 2023 Mw 7.8 Kahramanmaraş, and the 2023 Mw 7.6 Elbistan earthquakes are plotted. (b), and (c) The velocities on profiles BB' and DD' across the EAF system. The velocity jump can be seen across the EAF segments. (d) and (e) Time series movement in the line-of-sight direction on pixels P1 (red hexagon) and P2 (yellow hexagon) respectively. 99

5.18 Velocity of the track AT43 from 29 January 2020 to 29 January 2023. (a) The velocity or creep rates estimated through SBAS time series analysis on the East Anatolian Fault (EAF) system. The velocity is estimated with reference to a stable pixel that exhibits a minimum 90% coherence shown by a light blue rectangle. The velocity shows a left lateral movement of the fault, the positive velocity shows the movement towards the satellite while negative velocity shows the movement away from the satellite. The focal mechanism solutions of the 2020 Mw 6.8 Elazığ, the 2023 Mw 7.8 Kahramanmaraş, and the 2023 Mw 7.6 Elbistan earthquakes are plotted. (b) The velocities on profiles BB' across the EAF system. The velocity jump can be seen across the EAF segments. (c) and (d) Time series movement in the line-of-sight direction on pixels P1 (red hexagon) and P2 (yellow hexagon) respectively. 101

5.19 Velocity of the track DT123 from 29 January 2020 to 29 January 2023. (a) The velocity or creep rates estimated through SBAS time series analysis on the East Anatolian Fault (EAF) system. The velocity is estimated with reference to a stable pixel that exhibits a minimum 90% coherence shown by a light blue rectangle. The velocity shows a left lateral movement of the fault, the positive velocity shows the movement towards the satellite while negative velocity shows the movement away from the satellite. The focal mechanism solutions of the 2020 Mw 6.8 Elazığ, the 2023 Mw 7.8 Kahramanmaraş, and the 2023 Mw 7.6 Elbistan earthquakes are plotted. (b), and (c) The velocities on profiles BB' and CC' across the EAF system. The velocity jump can be seen across the EAF segments. (d) and (e) Time series movement in the line-of-sight direction on pixels P1 (red hexagon) and P2 (yellow hexagon) respectively. 102

List of Tables

3.1 Features of Sentinel-1A interferometric pairs 27
3.2 Detail of interferogram errors calculated using semi-variogram 29
3.3 The estimated source fault parameters, inverting both ascending and descending interferograms along with their uncertainties by assuming single fault plane and ignoring fault-bends 32
3.4 The FPF and FBF models with varying dips at 7.5 km depth and their corresponding residuals. The 40° dip results consistently with the lowest RMS residuals. 40
3.5 AIC, RMS and Reduced-Chi-square analysis for forward- and backward-vergent models, depth = 7.5 km, dip = 40°. The reduced-chi-square statistic is a measure of the squared difference between the observed and modeled values, considering the degrees of freedom, and the sample size 42
3.6 AIC, RMS for forward- vergent FPF model with dip = 40°with, and varying depth. 42

4.1 Features of Sentinel-1 data 52
4.2 Detail of interferogram errors calculated using semi-variogram 54
4.3 The inverted ruptured fault parameters using Sentinel-1 ascending and descending deformation data 61

5.1 Features of Sentinel-1A data used for estimating the deformation produced by Antakya aftershock 81
5.2 Detail of ascending descending interferograms dataset errors calculated in terms of LOS displacement of Antakya aftershock using semi-variogram 83